INSTITUTO SUPERIOR DE ENGENHARIA DE LISBOA
Área Departamental de Engenharia Electrónica e Telecomunicações e de Computadores

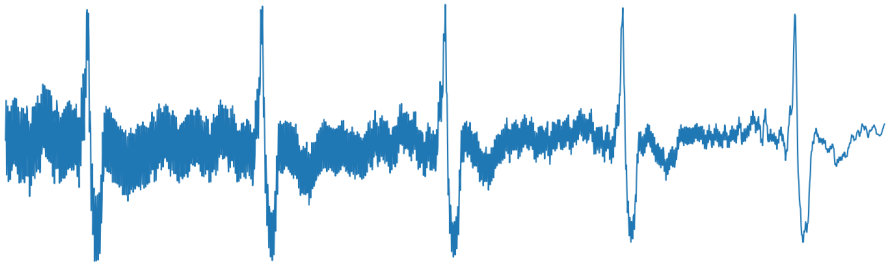

Adaptive ECG Acquisition System

DAVID VELEZ
(Licenciado)

Thesis submitted in the fulfilment of requirements for the Master's Degree in Electronics and Telecommunications Engineering (Electronics Engineering Expertise)

Supervisors:
PhD André Ribeiro Lourenço
PhD João Pedro Barrigana Ramos da Costa

Jury:
President: PhD Paula Maria Garcia Louro
Vowels: PhD Luís Miguel Tavares Fernandes

June of 2023

Acknowledgements

I would like to thank Professors André Lourenço and João Costa for their support and guidance throughout this project. Without their expertise and mentorship, this project would not have been possible.

A very special thanks goes to my family, my parents António Velez and Fátima Velez and my girlfriend Ana Rita Marçalo, for all the support and encouragement during my academic career.

I would also like to extend my sincere appreciation to the exceptional team at CardioID Technologies for their feedback, suggestions, and encouragement. In particularly to Lourenço Abrunhosa for all his help regarding acquisition set-ups and digital signal processing, as well as to José Santos for his valuable feedback in firmware development.

Finally, I would like to express my deepest gratitude to all the individuals who volunteered for electrocardiogram acquisition and provided invaluable data for this project. I am grateful for your participation.

Abstract

Noise is one of the major challenges in engineering, especially in bioengineering. The recording of the heart signal using an electrocardiogram (ECG) system is one of the most relevant tools for clinical evaluation as well as other non-medical applications. The use of ECG for biometrics and drowsiness detection is opening new possibilities for the use of these systems in daily-life applications, which are even more prone to noise.

This project aims to develop a novel ECG front-end design with the ability to adaptively change its characteristics as a function of each acquisition context. By understating the most common signal distortion sources and evaluating several ECG quality assessment techniques, an adaptive ECG circuit architecture is created and validated.

Several scenarios for testing the system are considered, starting from a theoretical perspective to several real-world acquisition scenarios, from resting conditions to acquisition while driving a vehicle. The designed system showed potential for usage as a tool for tackling unfavorable and challenging situations.

Resumo

Neste projeto desenvolveu-se uma solução completa para a aquisição de eletrocardiograma (ECG) de forma adaptativa. A aquisição de ECG foi inicialmente desenvolvida para aplicação em ambiente clínico e hospitalar, esta apresenta um enorme potencial na avaliação clínica de pacientes, fornecendo informação essencial ao cardiologista sobre o funcionamento do coração. No entanto, avanços tecnológicos e uma consciencialização por parte do público, no que diz respeito à saúde e a uma melhor qualidade de vida, fez aumentar a demanda por dispositivos *consumer electronics* para aplicações não-clínicas com a finalidade de monitorização de bio-sinais em contexto desportivo, bem como no decorrer da vida quotidiana. Estes são designados por *wearable devices*.

Este projeto tem como objetivo o desenvolvimento de uma nova abordagem à aquisição de ECG, ao criar um sistema que adapta as suas caraterísticas dinamicamente, conforme necessitado por cada sujeito ou contexto de aquisição, e que em conjunto com um algoritmo de avaliação da qualidade (*quality assessement*) de ECG capaz de identificar as fontes mais comuns de distorção no sinal eletrocardiográfico e avaliar o seu impacto, permitiu desenvolver uma solução de aquisição adaptativa.

Foram considerados vários cenários de teste para o sistema, desde aplicações teóricas a contextos no mundo real, desde aquisição em repouso até a aplicação no volante munido de elétrodos condutores durante a condução. O sistema mostrou potencial para aplicações em contextos desafiantes e dinâmicos.

Resumo Alargado

Neste projeto desenvolveu-se uma solução completa para a aquisição de eletrocardiograma (ECG) de forma adaptativa, pretendendo dar resposta aos novos desafios inerentes aos contextos de aquisição criados pelo aumento da demanda por dispositivos *wearable*. Esta nova abordagem adapta dinamicamente as suas caraterísticas conforme o contexto de aquisição ditar, tirando partido de um algoritmo de *quality assessement* capaz de identificar um conjunto de interferências no sinal eletrocardiográfico. A solução desenvolvida tem capacidade de aquisição de ECG com uma grande variedade de elétrodos, sejam estes com eletrólito de gel ou elétrodos secos, em condições desfavoráveis ou dinâmicas. A capacidade de suportar um vasto leque de contextos de aquisição é bastante relevante para aquisição em dispositivos *wearable*, visto estes dispositivos terem como aplicação a monitorização de bio-sinais em contextos não-clínicos, desde o decorrer da vida quotidiana até atividades desportivas, tipicamente com recurso a elétrodos secos, tais como têxteis condutores.

O sistema tem capacidade de identificação de um conjunto de tipos de interferência presentes durante a aquisição através do algoritmo de *quality assessement* e apresenta como vantagem comparativamente à abordagem tradicional o ajuste dinâmico de parâmetros do *front-end* analógico do eletrocardiógrafo como forma de mitigar os efeitos de distorção de sinal criados pelas referidas interferências.

A solução desenvolvida é completa e composta por várias camadas, nomeadamente:

- *Software*: Algoritmo de *quality assessement*,
- *Hardware*: Sistema físico,
- *Firmware*: Interface entre microcontrolador e *front-end* analógico,
- *User interface*: Interface gráfica do utilizador.

O algoritmo de *quality assessement*, implementado em MATLAB, tem a capacidade de deteção das seguintes fontes de interferência:

- Saturação,
- *Baseline wander*,
- *Power line interference*.

Para tal tira partido de *thresholds* definidos para o sinal, bem como de uma série de ferramentas de processamento de sinal como a transformada de Fourier e a transformada de Wavelets.

O *hardware* desenvolvido tem flexibilidade ao nível de vários parâmetros do *front-end* analógico.

(Conteúdo removido ao abrigo da alínea 3ª do Artigo 17º do Anexo do Despacho n.º 10934/2020, publicado em Diário da República Portuguesa n.º 217/2020, Série II de 6 de Novembro de 2020.)

Este *hardware* comunica com um PC através de uma interface USB de onde provém também a sua alimentação. Embora este tipo de interface seja compatível com a generalidade dos PCs modernos, é pressuposto da solução desenvolvida que a interface seja feita com um PC portátil, realizando o desacoplamento galvânico da rede elétrica, de modo ao contexto de aquisição se aproximar ao de um dispositivo *wearable*.

O *firmware* desenvolvido para este sistema tem como finalidade garantir a frequência de amostragem, permitir o envio dos dados recolhidos para o PC e receber comandos de ajuste do mesmo, permitindo alterar as características do *front-end* analógico. O *firmware* foi desenvolvido em linguagem MicroPython, executado num MCU Raspberry Pi Pico.

Num PC correm as camadas de *quality assessement* e de *user interface*, implementadas em MATLAB e MATLAB *App Designer* respetivamente. A interface gráfica para o utilizador, *user interface*, faz o *display* dos dados recolhidos pelo sistema, permite ao utilizador definir os parâmetros de ajuste de forma manual ou automática, bem como fazer a gravação dos dados recebidos para um ficheiro.

Foram criados cenários de teste diversificados de forma a testar qualitativamente e quantitativamente o desempenho do sistema. Os testes criados incluem testes funcionais aos parâmetros ajustáveis, testes em humanos em contextos diversos e testes com tipos de elétrodos variados.

Contents

List of Tables

List of Figures

List of Acronyms

ADC Analog-to-Digital Converter

AFE Analog Front-End

BW Baseline Wander

CWT Continuous Wavelet Transform

CMR Common-Mode Rejection

CMRR Common-Mode Rejection Ratio

CPU Central Processing Unit

DWT Discrete Wavelet Transform

DMA Direct Memory Access

DSP Digital Signal Processing

ECG Electrocardiogram

EMA Electrode Motion Artifacts

FFT Fast Fourier Transform

FR Fast Restore

FT Fourier Transform

GPIO General Purpose Input/Output

GUI Graphical User Interface

HFN High Frequency Noise

IA Instrumentation Amplifier

IC Integrated Circuit

IMSC *Instrumentação Médica, Sensores e Circuitos*

MCU Micro-Controller Unit

PC Personal Computer

PCB Printed Circuit Board

PLI Power Line Interference

QA Quality Assessment

RE Reference Electrode

RLD Right Leg Drive

SAT Saturation

SDI Serial Data In

SDO Serial Data Out

SPI Serial Peripheral Interface

TF Transfer Function

UART Universal Asynchronous Receiver-Transmitter

USB Universal Serial Bus

WT Wavelet Transform

Chapter 1

Introduction

The Electrocardiogram (ECG) is one of the primary cardiovascular screening tools. It measures the electrical activity of the heart to obtain a better understanding of its functioning [1]. Medical-grade ECG recordings are performed in controlled conditions with multi-channel devices with several features for interference mitigation such as Reference Electrode (RE) and gel coated electrodes. These devices are usually large in size, accessible only on health-care facilities, and recordings are performed with the patient in a resting state.

Technological advancements and public awareness towards a better quality of life have driven a demand for *health-tech*, non-medical-grade wearable devices, allowing telemonitoring of human biosignals through activities of daily life. These devices provide users with the ability to keep track of parameters such as activity levels, heart rate, blood oxygen level, etc. In regards to ECG monitoring, the current state-of-the-art is single-channel devices with no electrical reference using dry contact electrodes. These devices are expected to perform in moderate to high physical activity conditions while being cost-effective in order to be made accessible to the general public.

Due to technical constraints and adverse acquisition conditions, noise sources that currently are non-issues in medical-grade recording devices have become major sources of signal distortion in recordings with wearable devices (e.g., power line interference). Furthermore, since ECG recording devices have fixed characteristics, the usage of wearable devices in dynamic conditions means that achieving the perfect signal conditioning for all scenarios is not feasible. Since signal interference sources affecting the ECG recordings significantly overlap its band of interest, the outcome is a trade-off between signal quality and interference rejection, as the most restrictive filtering conditions will limit device applications from biometrics to heart rate detection.

For over 6 years, I have been a part of the engineering team at CardioID Technologies, developing its core product, CardioWheel, a system that acquires the ECG to continuously detect fatigue, drowsiness, and cardiac health problems, with a particular focus on automotive applications. Currently, CardioID is a partner at the i-DREAMS consortium, which is a 3-year project funded by the European Union's Horizon 2020 research and innovation program that aims to increase driver safety with as accurate as possible risk monitoring, by creating a *safety tolerance zone* to prevent drivers from getting too close to the boundaries of unsafe vehicle operation, in which fitness-to-drive (fatigue, drowsiness, stress, and other factors) emerge as critical risks for all drivers.

ECG plays a role in the detection of these parameters that will be performed by CardioWheel via the monitoring and processing of the driver's ECG signal by proprietary and patented algorithms, in which signal quality has a direct impact on the ability of the system to quantify these risk factors. Achieving the best quality acquisition is of the utmost importance since it will result in a safer environment for all road users as a result

of traffic accident risk mitigation.

1.1 Project Aim and Contributions

Some sources of signal distortion affecting ECG recordings are able to force device saturation for considerable periods of time, rendering the original signal irrecoverable by Digital Signal Processing (DSP) techniques.

This project aims to develop a solution with added resilience to most common signal distortion sources affecting ECG recordings by addressing these issues directly at hardware level with dynamically changing Analog Front-End (AFE) characteristics as required by the acquisition context. This system will represent a novel approach to ECG AFE design by creating an adaptive ECG circuit architecture to validate the viability of this solution.

This design will be adjusted as a function of the outputs from a Quality Assessment (QA) algorithm. This algorithm will be able to identify and quantify the different issues affecting ECG recording and control the AFE as a function of its output.

Project goals can be summarized as:

1. Gain understanding on the most common signal distortion sources affecting ECG recordings.
2. Develop an adaptive ECG AFE and its associated control circuit.
3. Evaluate and implement an ECG QA algorithm.
4. Implement and validate the system in various scenarios.

As a result of this dissertation, a paper was presented at *ENBENG 2023 - 7th IEEE Portuguese Meeting on Bioengineering* with the title *Electrocardiographic Signal Quality Assessment Without Morphology Analysis*. The paper focuses on the implementation of an ECG QA algorithm and methodology for situations where the system cannot directly analyze the ECG signal due to regulatory restrictions.

1.2 Scope & Limitations

Although the ECG signal carries great clinical significance, this analysis is beyond the scope of this project, which will focus solely on the intent of mitigating the issues described in order to provide the best possible ECG recording for further analysis. Any interaction with clinical staff will be restricted to research purposes only.

1.3 Organization of Document

This document is organized as follows:

- **Chapter 2**: Provides the necessary foundations for the understanding of the ECG signal, the electrophysiological processes in the heart, and the terminology used throughout the thesis, including the origin of biopotencials, the anatomy and physiology of the human heart, ECG lead systems, normal ECG signal, and the technical aspects of ECG recording, including ECG acquisition systems, artifacts, and interference. It is followed by the state of the art of ECG acquisition as well as relevant literature.
- **Chapter 3**: Describes the methodology applied to this project, including the medical-grade ECG databases used, primary data acquisition hardware and acquisition context, and mathematical background of the analysis tools used.

- **Chapter 4**: Describes the development process of the ECG QA algorithm to detect relevant noise and distortion sources.
- **Chapter 5**: Describes the development of the ECG acquisition system by detailing system architecture, analog signal conditioning, hardware implementation, Micro-Controller Unit (MCU) selection, firmware development, communication protocols, and Printed Circuit Board (PCB) design.
- **Chapter 6**: Details the graphical user interface, displayed data, controls and adaptation algorithm.
- **Chapter 7**: Presents a discussion on the results obtained with a multitude of electrode types, acquisition scenarios, and test subjects.

Chapter 2

Concepts & State of the Art

2.1 Biopotentials

Biopotentials are generated by the electrochemical activity of a specific group of cells called excitable cells. These cells exhibit a resting potential when not stimulated and undergo an action potential in response to appropriate stimulation. The are many measurable biopotencials with medical significance, such as: ECG, EEG (electroencephalography), EMG (electromyography), EOG (electrooculography) and AAP (Axon Action Potential). Overall, electrophysiological signals have low amplitude ($1\mu V$ to $100mV$) and their spectral content is comprised mostly of low frequencies ($0Hz$ up to $10kHz$) [2].

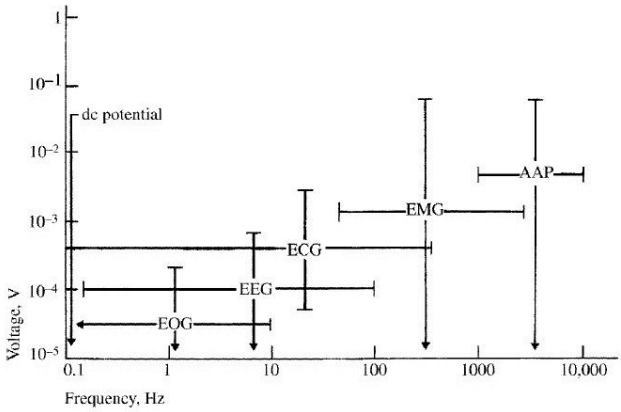

Figure 2.1: Voltage and frequency of various biopotencial signals. Figure from [2].

Figure 2.1 displays how different biopotencials cover different amplitudes and portions of the frequency spectrum. These characteristics set constrains of gain and frequency-response that must be taken in to consideration when designing a biopotencial amplifier. The amplifier for a particular biosignal must be designed to handle that potential by providing appropriate signal conditioning and amplification at its output. All biopotencial amplifiers must meet certain requirements: they must have high input impedance, so that they provide minimal loading of the signal being measured, and the input circuit must be safe to the organism being studied [2].

An appropriate transducer for the biosignal being captured is applied to the patient in order to convert energy, or information, to another form, usually electric. This energy provides an analog signal able to be conditioned and processed to be displayed to humans.

2.1.1 The Electrocardiogram

The heart is the muscular organ that pumps blood though the blood vessels of the circulatory system. The pumping is performed in a cycle of coordinated contractions of the ventricles and atria in which every contraction is governed by corresponding electrical impulses. These vital electrical impulses ensure synchronized and efficient pumping of blood.

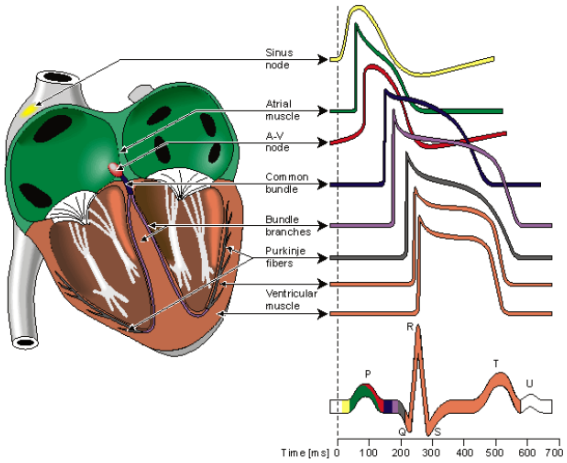

Figure 2.2: The genesis of the electrocardiogram. Figure from [3].

The cells of the cardiac muscle, called myocardium, have the capability of self-stimulation, generating the cardiac rhythm, normally, a regular sequence of heart beats. As illustrated in Figure 2.2, a regular cardiac cycle is initiated by the sinoatrial node (SA node) and followed by the atrioventricular node (AV node). The SA nodal cells are self-excitatory pacemaker cells, generating an action potential at the rate of about 70 per minute. Between them, the internodal atrial connects the SA and AV nodes and regulates the passage of the cardiac impulse from the atria to the ventricles [4].

This system enables the electrical triggering impulses generated at the SA node to be propagated from the wall of the right atrium (where the SA node is located), to the deeper tissues of the ventricular muscles. From the inner side of the ventricular wall, the many activation sites cause the formation of a wavefront, which propagates through the ventricular mass toward the outer wall. This process results from cell-to-cell activation. After each ventricular muscle region has depolarized, repolarization occurs. The termination of activity appears as if it were propagating from epicardium (the outer side of the cardiac muscle) toward the endocardium (the inner side of the cardiac muscle). The heart can therefore be viewed as an bio-electrical generator. The electrical pulses generated by the components of the cardiac activity displayed in Figure 2.2 propagate though the body and can therefore be detected at its surface. The graphical reproduction of the heart's electrical activity as registered on the bodies surface is called ECG [4].

The orderly pattern of all the ECG components generates the characteristic ECG pulse: the P wave (atrial depolarization), the QRS complex (ventricular depolarization) and the T and U wave (ventricular re-polarization), seen in Figures 2.2 and 2.3. Each complex has a particular spectral content: the P wave, with a duration of approximately 150ms and spectral content up to 10Hz; the QRS complex has a relatively higher amplitude compared with the other waves, with a duration of approximately 100ms in a normal heartbeat and has mostly frequencies between 10 to 250Hz; the T wave, with a duration of approximately 300ms and spectral content up to 8Hz, is mostly dependent on the heart rate [34]. The heart rate can be obtained as the inverse of R-R interval, the period between two successive R waves on the electrocardiogram.

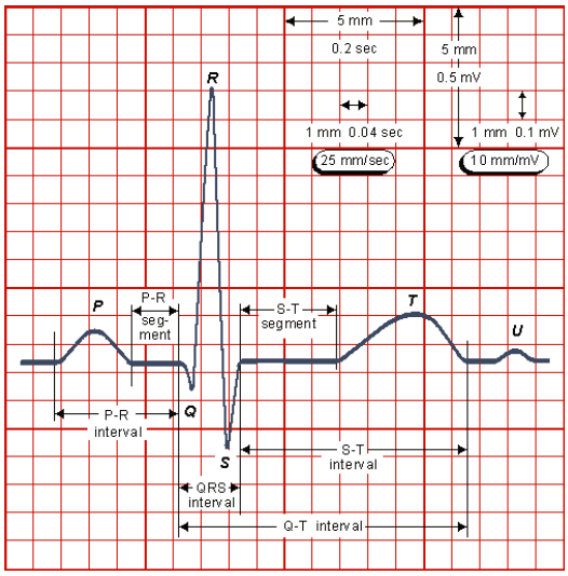

Figure 2.3: Schematic diagram of normal heart rhythm for a human heart as seen on ECG. Figure from [3].

2.2 The Electrocardiograph

2.2.1 Historical Development

Augustus Désiré Waller (1856-1922), a British physiologist from the late 19th century, experimented with bio-electromagnetism and developed an apparatus based on a Lippmann capillary electrometer that, in conjunction with the developments of Étienne-Jules Marey (1830–1904) in chronophotography, lead him to develop the first electrocardiograph, apparatus shown in Figure 2.4. His work was published in the *Journal of Physiology* in 1887 and displayed at the *Physiological Society* meeting at London in the same year [4].

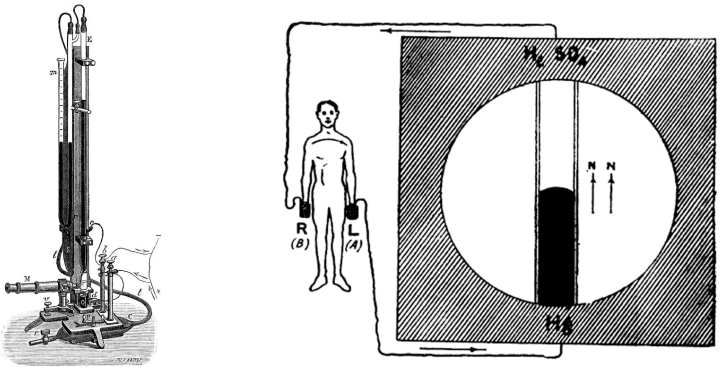

Figure 2.4: Lippmann capillary electrometer (left) and diagram of the connection between patient and device(right).

The Lippmann electrometer consisted in a reservoir ending in a glass capillary filled with with mercury (bottom half) and sulphuric acid (top half). Changes in electric current affected the surface tension of the mercury, allowing it to move in the capillary tube. The inertia of the mercury column and the friction in the capillary caused distortion on the electrocardiography tracings, as displayed in Figure 2.5. This was a known issued accepted as inevitable.

Willem Einthoven (1860-1927) continued to develop the apparatus used by Waller, which led him to dominate the published papers in the history of electrocardiography and

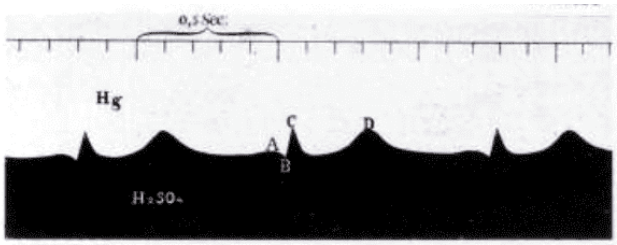

Figure 2.5: Lippmann capillary electrometer ECG recording. Adapted from [5].

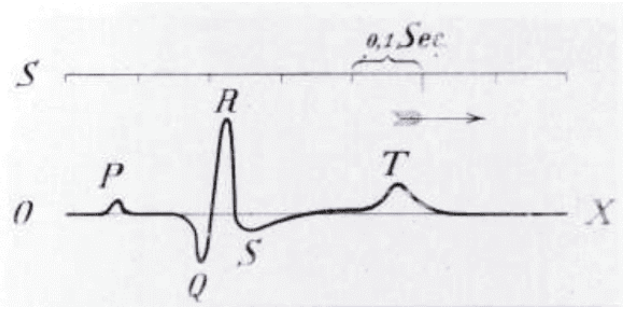

Figure 2.6: Mathematically corrected capillary electrometer ECG recording. Adapted from [5].

win the Nobel Prize in Physiology or Medicine in 1924. In 1893, Einthoven introduces the term *electro-cardiogrammem* at a meeting of the *Dutch Medical Association*. In 1885, he derived a mathematical correction that compensated for the inertia and friction of mercury column in the Lippmann capillary electrometer, allowing for superimposing the mathematically corrected curve on the uncorrected tracing. He also labeled the corrected deflections as P, Q, R, S and T (previously named ABCD), as shown in Figures 2.5 and 2.6.

Still dissatisfied that the mathematical correction had to be repeated for every tracing, making the process cumbersome for widespread clinical use, Einthoven set out to develop an instrument which would be both rapid and sensitive enough to prevent the need for correction. Whereas Lippmann's electrometer was sensitive but slow, the galvanometer developed by Jacques-Arsène d'Arsonval (1851-1940) was rapid but lacked the required sensitivity to register the heart's action currents. Einthoven devised a number of improvements in order to overcome the galvanometer's shortcomings. The solution developed by Einthoven used a single thin and short wire of silver-coated quartz placed in a narrow space between the poles of a strong electromagnet. Each of the poles was perforated by holes through which the string could be illuminated and observed by two microscopes.

Figure 2.7: One of the first electrocardiograms with the string galvanometer, published by Einthoven in 1902. Adapted from [5].

The construction of the string galvanometer was completed by 1901. The first elec-

trocardiograms obtained by the new apparatus equalled Einthoven's mathematically corrected Lippmann electrometer tracings, validating both his correction method and string galvanometer apparatus, as shown in Figure 2.7. By 1906, Einthoven's laboratory was connected with the academic hospital, at a distance of over 1km via an underground telephone cables, allowing for the first series of *tele-cardiograms* from patients could be recorded. These systems continued development trough the years, culminating in the modern systems with digital media signal storage.

2.2.2 Electrocardiogram Leads

The electric activity generated by the beating heart can be approximately represented as a vector quantity. A simple model to represented the electric activity of the heart was developed, in which the heart consists of an electric dipole located in the conducting medium of the thorax, as shown in Figure 2.8. The potentials generated by the heart appear throughout the body's surface, and these can be are determined by placing electrodes on it and measuring the voltage between them. Pairing electrodes at different locations yields different voltages due to the spatial dependence of the electric field of the heart [2].

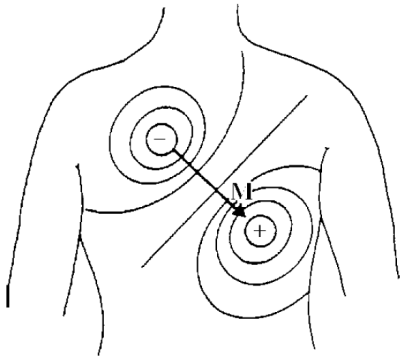

Figure 2.8: Representation of the dipole filed of the heart when the R wave is maximal. Figure from [2].

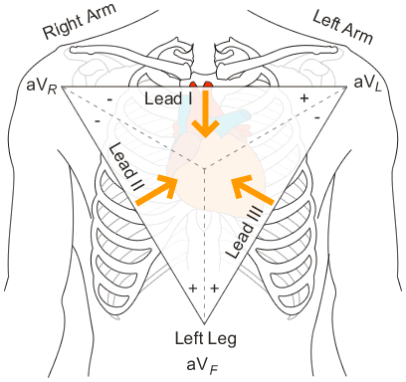

Figure 2.9: *Einthoven's Triangle*. Figure from [6]

The *Einthoven's Triangle* refers to the imaginary inverted equilateral triangle centered on the chest, with the vertices representing the standard leads on the arms and leg, Figure 2.9. Later, Frank Norman Wilson (1890–1952) proposed a new method where ECG unipolar potentials can be defined, using the central terminal as reference, this method is still being used in the present day [4]. The unipolar potentials result from the connection of a resistor from each terminal of the limb leads to a common point,

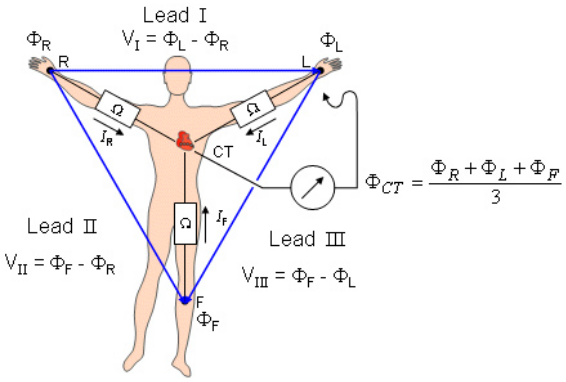

Figure 2.10: The Wilson central terminal (CT) is found at the center of the *Einthoven's Triangle*. Redrawn and adapted from [4] .

the central terminal (CT), as shown in Figure 2.10. That unipolar potentials should be measured with respect to this terminal. So, the Wilson central terminal represents the average of the limb potentials, because the total current into the central terminal from the limb leads must add to zero to satisfy the conservation of current (Kirchhoff's 1st Law describe that the algebraic sum of currents in a network of conductors meeting at a point is zero ($IR + IL + IF = 0$)) [4] . The resistance value of each terminal has significant importance and, gratefully, nowadays the input impedance of the biopotential amplifiers, Instrumentation Amplifier (IA), is high, which increases the Common-Mode Rejection (CMR), as will be described in Section 2.2.3. In Figure 2.10 is also illustrated, within the *Einthoven's Triangle*, the bipolar limb leads which are usually designated as Lead-I, II and III and they track the electrical potential of the heart when three electrodes are placed on the right and left hand, as well as the left foot. The voltages and potentials represented are:

- V_I = the voltage of Lead-I;
- V_{II} = the voltage of Lead-II;
- V_{III} = the voltage of Lead-III;
- Φ_L = potential at the left hand;
- Φ_R = potential at the right hand;
- Φ_F = potential at the left foot.

Another category of lead orientation is the precordial leads (V1, V2, V3, V4, V5, V6) which are recorded with 6 additional electrodes attached to the chest and give more information within the electrocardiogram, as illustrated in Figure 2.11. This acquisition topology provides 6 vertical axes and 6 horizontal axes and is the typical configuration for medial-grade devices providing the most clinical information. The large amount of connections needed makes this implementation impractical for wearable devices.

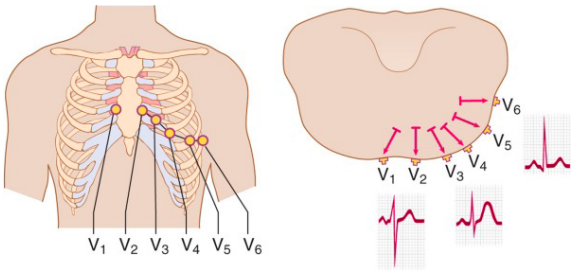

Figure 2.11: Precordial leads. Adapted from [4].

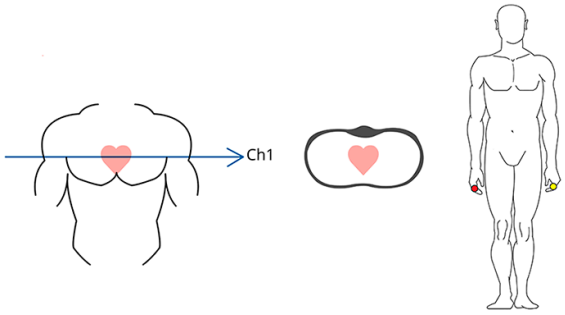

Figure 2.12: Representation of Lead-I ECG. Figure from [7].

Figure 2.12 displays the minimum viable topology for ECG recording, providing 1 axis o measurement. Lead-I is the typical configuration used on wearable devices.

2.2.3 The Instrumentation Amplifier

In general, bioelectric potential signals exhibit extremely small amplitudes, necessitating amplification and conditioning before they can be recorded and processed. As a result, the utilization of a biopotential amplifier becomes indispensable, as it serves the critical purpose of enhancing the amplitudes of these delicate potential differences originating from biological electric signals.

An IA is widely used as a biopotential amplifier. It has some characteristics that make it appropriate for measuring signals from low-level output transducers in noisy environments. The IA amplifies the difference between two input signal voltages while rejecting any signals that are common to both input terminals.

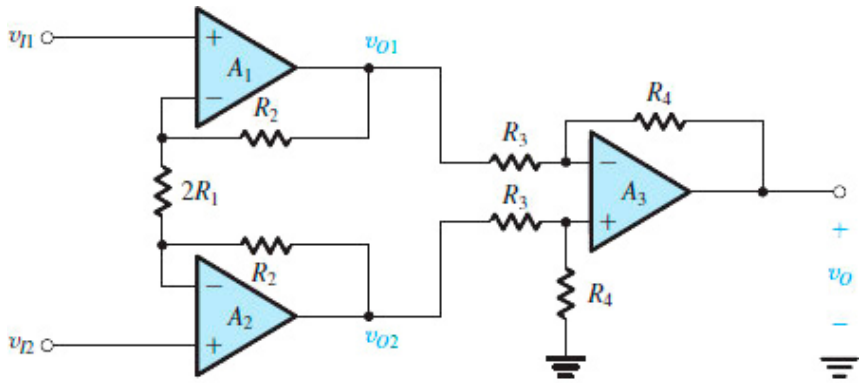

Figure 2.13: Instrumentation amplifier circuit topology. Adapted from [8].

The IA consists of two stages of operational amplifiers (op-amp) in cascade configuration. Regarding Figure 2.13, the first stage of the IA is formed by op-amps $A1$ and $A2$, each in a non-inverting configuration, realize a gain, G, of:

$$G_{A_{1,2}} = 1 + \frac{R_2}{R_1} \tag{2.1}$$

Therefore:

$$v_{O2} - v_{O1} = \left(1 + \frac{R_2}{R_1}\right).(v_{I2} - v_{I1}) \tag{2.2}$$

The second stage, op-amp $A3$ and its four associated resistors, implement a difference amplifier and provide at its output:

$$v_O = \frac{R4}{R_3}\left(1 + \frac{R_2}{R_1}\right).(v_{I2} - v_{I1}) \tag{2.3}$$

Thus, differential gain can be presented as:

$$A_d = \frac{v_O}{v_{Id}} = \frac{R4}{R_3}\left(1 + \frac{R_2}{R_1}\right); v_{Id} = v_{I2} - v_{I1} \tag{2.4}$$

From Equation 2.4 it is possible to conclude that IA gain can be varied by changing only one resistor value, R_1. In most common Integrated Circuit (IC) implementations of IA all resistors are implement internally with the exception of R_1, which can be connected via the IC device pins, implementing a way for gain to be set in circuit design. Such devices are widely employed in a variety of electronic instruments as differential amplifier circuits.

On an ideal IA, common-mode gain will be zero because of the subtractive action of the differential amplifier amplifier. In fact, CMR is the most important function that an IA provides, the property of canceling out any signals that are common on both input terminals, while amplifying any signals that are differential between the inputs. Both DC and AC CMR are important, since inadequate CMR of undesired sources, such as offset DC voltage, may cause errors difficult to remove afterwards. Fortunately, most modern IA provide excellent DC and AC CMR. Figure 2.14 provides a functional block diagram of an IA with the undesired common-mode voltage.

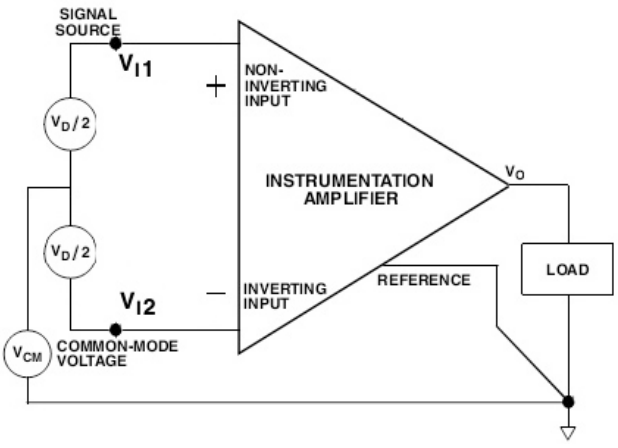

Figure 2.14: Differential vs common-mode input sources. Redrawn and adapted from [9].

Unfortunately, due to manufacture conditions and material temperature, it is impossible com completely cancel out common-mode errors in the IA. Mathematically, Common-Mode Rejection Ratio (CMRR) can be represented as:

$$CMRR = 20log_{10}\left(\frac{A_d}{A_{cm}}\right) \tag{2.5}$$

In Equation 2.5, CMRR is expressed in decibels (dB), A_d is the differential mode voltage gain of the amplifier and A_{cm} is the common mode voltage gain of the amplifier. Higher the CMRR values represent better rejecting of common mode signals.

2.2.4 Modern Topology - Characteristics & Requirements

Modern systems can be divided in to two parts: the AFE and the back-end. The AFE is responsible for signal conditioning, while the back-end is responsible for signal digitization, processing, and storage. These back-end functions are usually performed by an MCU.

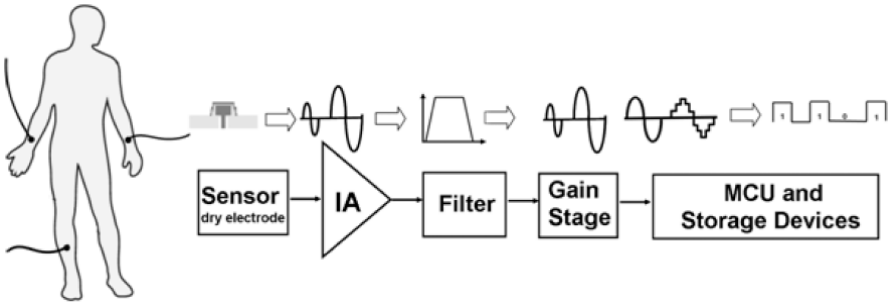

Figure 2.15: Generic electrocardiograph topology. Figure from [2].

Due to the electrocardiograph wide-spread use as a diagnostic tool, standardization is necessary, such as *IEC 60601*, a series of technical standards for the safety and essential performance of medical electrical equipment [10]. In particular, *IEC 60601-2-47:2012* concerns ambulatory ECG systems and provides the groundwork for all the new specifications such as *ISO/IEC 80601-2-86*, a work-in-progress by the *ISO/IEC Joint Work Group 22* [11], [12]. These standards, in conjunction with recommendations for standardization and specifications to be used for automated electrocardiography classification [13], define a set of specific criteria regarding filtering, sampling rate, and Analog-to-Digital Converter (ADC) for ECG devices, summarized as:

- **Instrumentation Amplifier (IA)**
  - **CMRR**: $89dB$ minimum for standard ECG and $60dB$ minimum for ambulatory recorders [14].
- **Filter**
  - **Low cut-off frequency**: 0.05 to $0.5Hz$ [13].
  - **High cut-off frequency**: $125Hz$ or more [13].
- **Gain Stage (and ADC)**
  - **Sampling Rate**: $500Hz$ at 10-bit resolution (minimum voltage resolution of $10\mu V$) [13].

2.2.5 The Electrode-Skin Interface

Biopotential measurements at the skin surface requires an interface between the body and the measuring circuit that allows the passage of current to an electrode and subsequently into the electronic circuit. This interface is called the electrode-electrolyte interface; the electrolyte is either a body fluid containing ions, sweat, or a gel electrolyte solution applied between the skin and the electrode; the electrode is an electrically conductive material. The electrode-electrolyte interface occurs when an ion-electron exchange (or electric current) flows from the skin to the electrically conductive material trough the electrolyte.

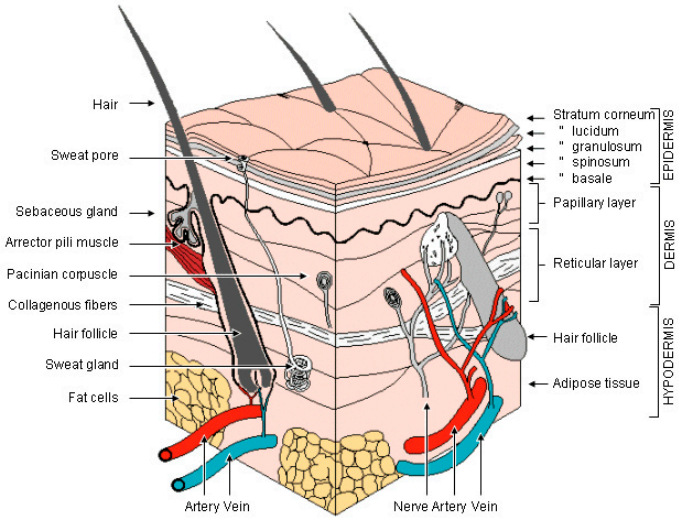

Figure 2.16: Human skin anatomy, showing the various layers. Adapted from [3].

The skin anatomy is displayed in Figure 2.16. It consists of three principal layers: hypodermis, which is the deepest one, the dermis and the epidermis, at the surface. These layers protect the body from its environment. The deeper layers of the skin contain blood vessels, nerves, sweat glands and hair follicles. The uppermost layer, the epidermis, is composed of dead cells (*stratum corneum*), keratin, and lipids on the surface of the skin, and thus, it has a high impedance [3].

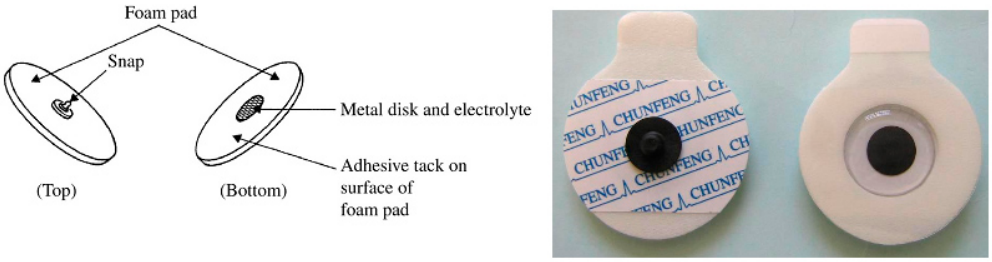

Figure 2.17: Ag/AgCl Gel body surface biopotential electrodes often used in ECG acquisition apparatus.

The standard electrode in clinical practice is the Agarose (Ag/AgCl) gel coated electrode, henceforth referred to as gel electrodes, displayed in Figure 2.17. The gel provides good electrical contact (low impedance) and provides mechanical stable connections for accurate bio-signal acquisitions. The electrode-electrolyte interface of the gel electrode is described by the models shown in Figure 2.18.

Analysing the circuit shown in Figure 2.18, the characteristics of the electrodes can be modelled by a non-linear *RC* circuit whose components are frequency and current

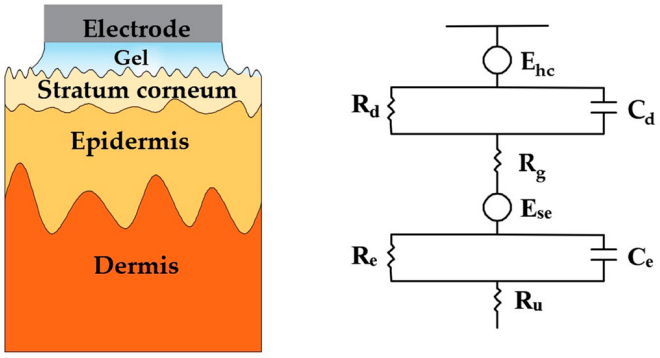

Figure 2.18: Schematic and electrical equivalent circuit model of electrode–skin interface for gel electrodes. Figure from [15].

dependent [2]. E_{hc} is the half-cell is formed at the electrochemical electrode–electrolyte interface when the electrodes are attached to the body. The structure of the interface is modelled by a capacitor C_d and resistor R_d in parallel. Resistance R_g represents the effective resistance associated with interface effects of the gel between the electrode and the skin. A difference in ionic concentration across the *stratum corneum* results in a potential E_{se}. The entire epidermis is treated equivalently with a resistance R_e and a capacitance C_e in parallel. The dermis and subcutaneous tissues can be treated as a pure resistor, R_u, since it's capacitance can be neglected [15].

Although gel electrodes have excellent proprieties, their usage requires skin preparation, hair-cutting, skin cleaning and gel coating; this process can be considerably time-consuming. Also, gel electrodes conductive gels suffer with dehydration over time, degrading their quality.

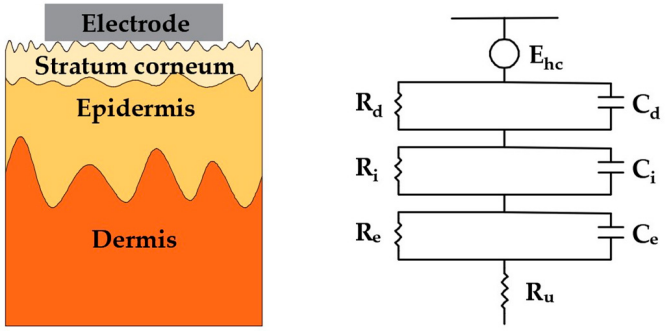

Figure 2.19: Schematic and electrical equivalent circuit model of electrode–skin interface for surface dry electrodes. Figure from [15].

Dry electrodes without conductive gels have the potential to address these issues, being advantageous in portability and ease-of-use. These are non-invasive electrodes with close contact to the skin, of which an equivalent circuit model is shown in Figure 2.19. Comparatively to conventional electrodes, there is no conductive gel between the electrode and the skin surface, therefore, the resistance R_g from Figure 2.18 is replaced by a capacitance C_i and a resistance R_i connected in parallel. Benefiting from their simple manufacturing processes and not causing discomfort to the user, dry electrodes are the most widely used type of electrode in wearable applications. They can maintain contact with the skin, even during motion, and are thus suitable for use in ambulant applications. When compared

to gel electrodes, dry electrodes present higher impedance, resulting in signals with lower amplitude and are more susceptible to motion artifacts and noise [15].

Another consequence of the electrode-skin interface is the offset DC voltage. When the electrodes are attached to the skin in different contact points, a few hundred mV are generated due to the impedance values associated with each electrode-skin interface. Fortunately, nowadays there are AFE amplifiers that can reduce this undesired offset. When the electrode is moved with respect to the electrolyte (mechanical alteration of the electrode-electrolyte interface), this movement cause a momentary change of the half-cell potential and thus a potential difference appears between the two electrodes during this movement. This momentary potential is known as Electrode Motion Artifacts (EMA) and can be a serious problem of interference in the measurement of biopotentials, as illustrated in Figure 2.15. Observation of this matter reveals that a major component of this noise is at low frequencies. Thus, EMA can be the most difficult type of noise to cancel, particularly when the spectrum of motion artifact overlaps with the desire signal.

2.2.6 Reference Electrode and Right Leg Drive

In an ECG system, a large amount of electromagnetic interference is coupled to the patient's body through the skin. As discussed in Section 2.2.2 and shown in Figure 2.9, bipolar ECG acquisition with *Einthoven's Triangle* configuration entails placing 3 electrodes, on the right and left wrist (or shoulders) and one in the on the left ankle (or left lower abdomen). Acquisition is performed on 2 of those leads with the 3rd lead acting as an electrical RE. The RE in ECG devices establishes a low-impedance reference point, serving as a fixed potential reference against which the voltages from other electrodes are measured. It provides a stable baseline voltage for the ECG recording, allowing differentiation between the desired cardiac signals and any external interference or noise, resulting in a clearer and more reliable ECG recording [2], [6], [7].

One technique to further improve CMRR performance is driving the common-mode voltage through the patient's body, known as Right Leg Drive (RLD). This reference point is typically driven by an amplifier circuit that generates an inverse signal to the common-mode noise present in the ECG signals. By doing so, the RLD circuit helps to minimize the impact of common-mode voltage variations, such as those caused by power line interference or patient movement, on the ECG signal. This improves the signal-to-noise ratio and enhances the accuracy of ECG measurements [2], [16]. Further details are provided in Section 5.1.1.

2.3 Issues in ECG Acquisition

The purpose of the AFE is to isolate unwanted noise from desired inputs. However, there are some sources of noise that affect the IA principles of acquisition.

2.3.1 Baseline Wander

Baseline Wander (BW) is the predominant low frequency noise that affects the ECG signal. The maximum frequency of the BW lies bellow $0.5Hz$ being caused mainly by patient's breathing (respiration). Increased movement of the body during exercise or stress test may increase the frequency content of BW.

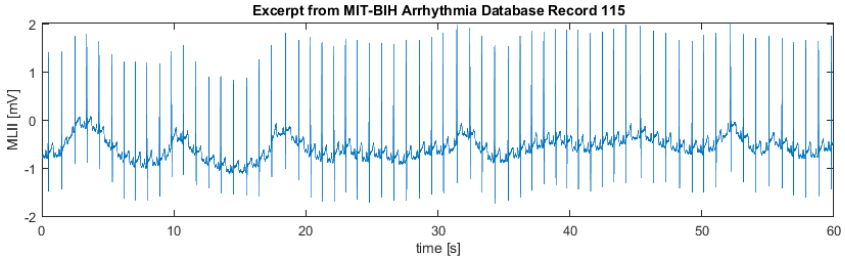

Figure 2.20: ECG corrupted with BW, obtained from MIT-BIH ADB record number 115.

When BW is present in a recording it can typically be observed throughout a majority of the recording. To reduce BW, techniques such as high-pass filtering, baseline correction, and signal averaging may be employed.

2.3.2 Electrode Motion Artifact

EMA is usually caused by intermittent mechanical forces acting on the electrodes when the subject moves. This may cause the skin to stretch or the electrodes to move or become dislodged, resulting in a momentary change in contact area with the electrode. Both of these factors can cause the input impedance to change.

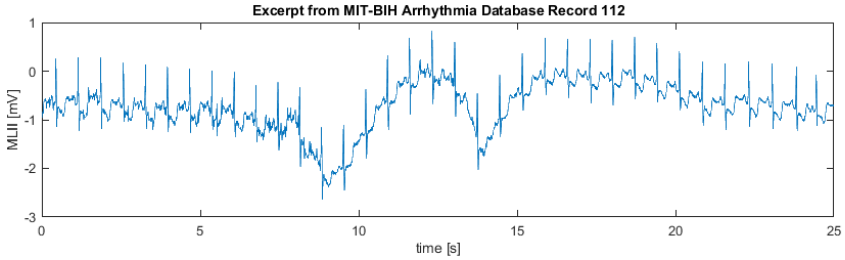

Figure 2.21: ECG corrupted with EMA, obtained from MIT-BIH ADB record number 112.

Unlike BW that can observed throughout the entirety of the recording, EMA are present only in short bursts.

2.3.3 Saturation

Saturation (SAT) is considered as a local zero amplitude DC line that occurs due device saturation.

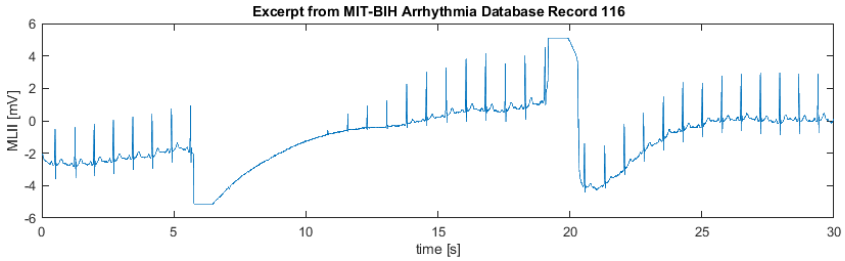

Figure 2.22: ECG corrupted with SAT, obtained from MIT-BIH ADB record number 116.

Following device SAT there is a settling period in which the time constant required to bring the ECG back into the amplifier's active region of operation is determined by the high-pass corner frequency of the amplifier's filtering section.[2]. Situations like show in Figure 2.22 can be due extreme cases of BW or EMA.

2.3.4 Power Line Interference Noise

In biopotential applications the high frequency signals from radio frequency and the signal components from electric power lines are undesired sources of noise. These components are added with the desired signal and appear at the input of the biopotential amplifier. These, cause displacement currents which flow to electrodes and create a differential voltage between the impedance of electrode-skin interface as well as the impedance of the user body [2].

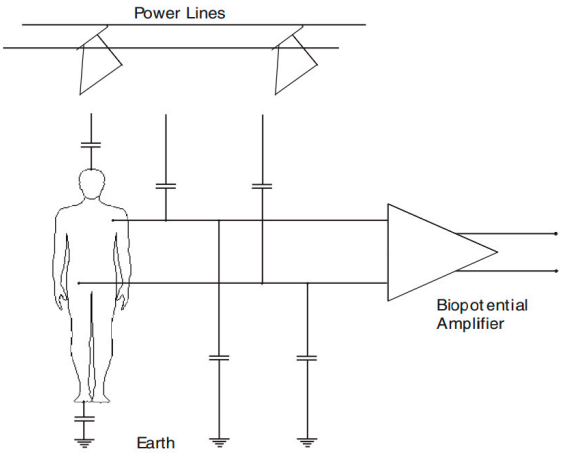

Figure 2.23: Coupling capacitances between the power line and lead wires causes parasite currents to flow through skin-electrode impedances. Figure from [17].

In fact, the signal from power lines would be the main source of external interference (noise) in biopotential measurements. Power lines are connected to equipment and appliances everywhere, mainly inside the floor and walls. Equations 2.6 trough 2.10 describe how this noise is injected and affects the biosignals acquisition, and in Figure 2.23 can be visualized a scenario occurring when the current flows from the power lines through the body and generate a common-voltage v_{cm} called common mode voltage. The v_{cm} is defined by the Equation 2.6, where i is the current generated by the electromagnetic field from the power lines, and Z_G is the impedance between the human body and the ground.

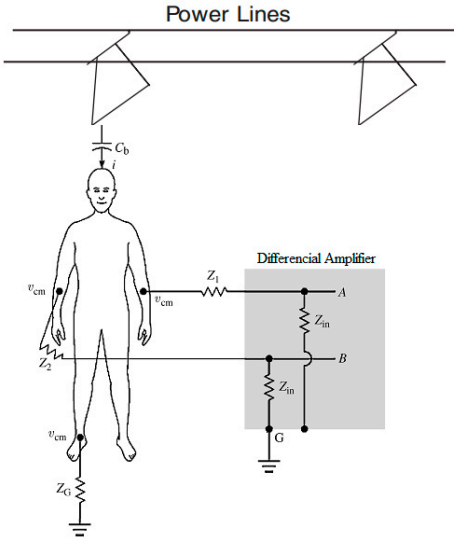

Figure 2.24: A common-mode voltage on the body is created by currents flow from the power line through the body to ground. Figure from [2].

$$v_{cm} = i.Z_G \tag{2.6}$$

Substituting the Equation 2.6 for the typical values [2], we have:

$$v_{cm} = (1\mu A).(100k\Omega) = 100mV \tag{2.7}$$

In poor electrical environments in which $i > 1\mu A$, v_{cm} can be greater than $100mV$. For ideal Amplifiers this would not cause any problem, because they can perfectly reject the common mode voltage ($Z_{in} = 1$). However, real Amplifiers have finite input impedance Z_{in} and this factor should be taken into account. Thus, v_{cm} will be affected by the attenuator action of the skin-electrode impedances (Z_1 and Z_2) and Z_{in}. Calculating again the noise level from this source, we obtain:

$$v_A - v_B = v_{cm}\left(\frac{Z_2}{Z_{in} + Z_2} - \frac{Z_1}{Z_{in} + Z_1}\right) \tag{2.8}$$

Since Z_{in} is much higher than Z_1 and Z_2,

$$v_D = v_A - v_B = v_{cm}\left(\frac{Z_2 - Z_1}{Z_{in}}\right) \tag{2.9}$$

Substituting with reference values, we obtain:

$$v_D = (100mV).\left(\frac{20k\Omega}{100M\Omega}\right) = 200\mu V \tag{2.10}$$

As described by the Equations 2.7 and 2.10, some v_{cm} is always present, so it is a critical factor to provide biopotential amplifiers with high CMRR, since the aim is to minimize the impact of this undesired voltage. Another source of interference is a magnetic induction from power lines. If such magnetic field pass through the effective single-turn coil produced by the biopotential circuit, lead wires, and the user, an induced voltage is presented in this loop, as illustrated in Figure 2.25a. However it can be reduced by twisting the lead wires together and keeping them close to the body, as illustrated in Figure 2.25b.

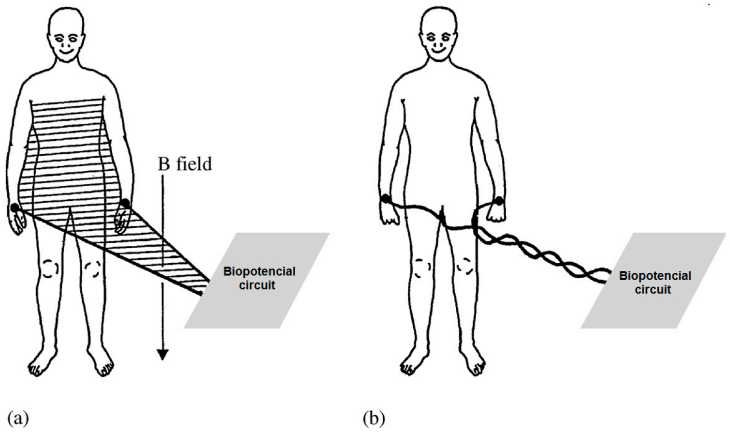

Figure 2.25: Magnetic interference presented in Biopotential measurement. Figure from [2].

Electromagnetic fields caused by a power line represent a common noise source in the ECG as well as to any other bioelectrical signal recorded from the body surface. Such power line interference (PLI) noise is characterized by 50 or $60Hz$ sinusoidal interference. It is possible for this interference to surpass the ECG signal in magnitude, if AFE saturation is reached this will result in a number of harmonics to the power line frequency being

present in the recording. Power Line Interference (PLI) is removable by narrow-band filtering. [18]

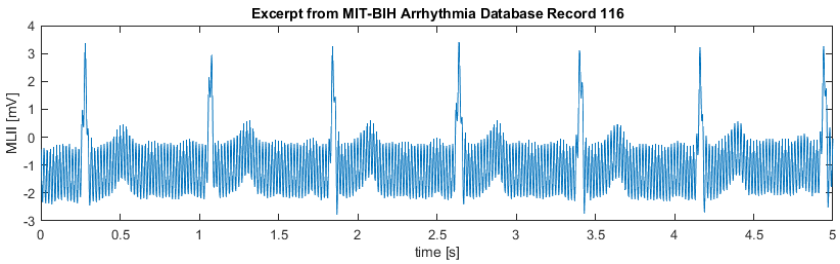

Figure 2.26: ECG corrupted with synthetic added power line interference, obtained from MIT-BIH ADB record number 232.

Figure 2.26 shows a typical acquisition of an ECG signal distorted by PLI.

2.3.5 Summary

Congruent with the aims set in Section 1.1, this project will focus mainly in noise sources that are able to reach AFE SAT by dynamical adapting AFE characteristic to the acquisition conditions. Development will focus in mitigating BW, SAT and PLI. Resilience to BW can be increased by adjusting the high-pass corner frequency of the amplifier's filtering section. For PLI mitigation, a switchable narrow-band filter will be implemented. High-frequency noise is rarely able to reach AFE SAT, for this noise source a fixed, a fixed low-pass corner frequency for the amplifier's filtering section will be set according to the requirements specified in Section . To mitigate SAT, AFE gain will be dynamically adjusted.

2.4 Literature Review

2.4.1 Quality Assessment

In *Signal Processing Techniques for Removing Noise from ECG Signals*, [18], the authors describe mainly four types of artifacts encountered in ECG signals: BW, PLI, electromyographic noise and EMA. Various signal processing methods for removing the artifacts from ECG signal are described ranging from signal filtering to Wavelet transform [18].

In *Automatic ECG analysis using principal component analysis and wavelet transformation*, the main objective was to develop methods to analyze and detect small changes in ECG waves and complexes that indicate cardiac diseases and disorders. This paper provides a great deal of information on the technical aspects of ECG recording including ECG electrodes, ECG artifacts and interference, it also provides the mathematical background of all methods described including wavelet transformation, the state of the art in ECG signal processing and ECG signal preconditioning. [3]

In *An automated ECG signal quality assessment method for unsupervised diagnostic systems*, the authors present an automated method for quality assessment of ECG signal, of which a flowchart is displayed in Figure 2.27. The proposed method, based on wavelet decomposition, is able to detect, localize and classify ECG noises including flat line (FL), time-varying noise or pause (TVN), BW, abrupt change (AB), PLI, muscle artifacts (MA) and additive white Gaussian noise (AWGN) as defined by the authors [19].

In *Signal Quality Indices for Ambulatory Electrocardiograms Used in Myocardial Ischemia Monitoring*, contrary to the previous scientific literature this paper concerns ECG acquisition in dynamic conditions. This study proposes and validates gating system for

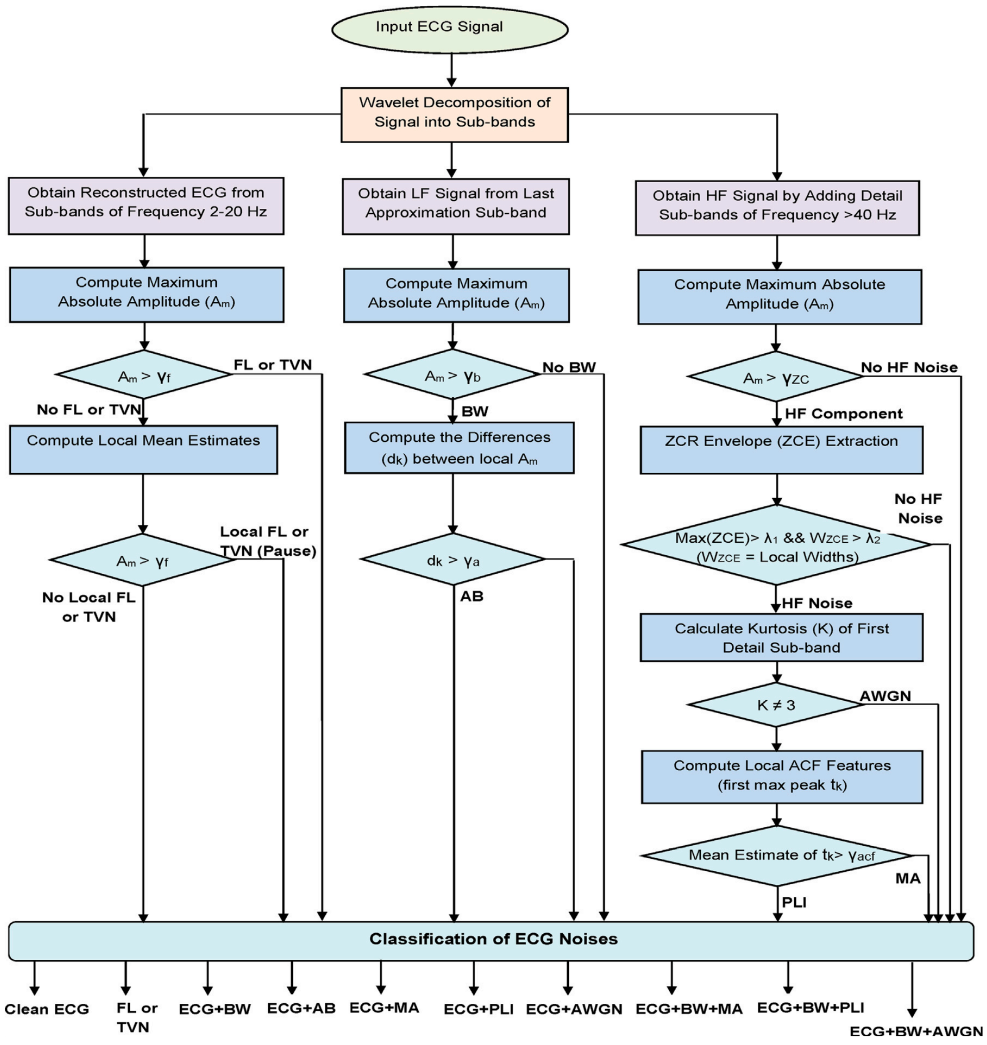

Figure 2.27: Simplified flow chart of the proposed method. Figure from [19].

monitoring of a specific medical condition, myocardial ischemia (partial or complete blockage of coronary arteries). The monitoring system relies on ambulatory electrocardiogram acquisition, since patients at risk are encouraged to ambulate to aid recovery, deteriorating the signal quality of the ECG leading to false alarms. The proposed alarm gating system computes a signal quality index (SQI) to quantify the ECG signal quality and rejects alarms with a low SQI. This solution employs a signal quality analysis algorithm based on signal-to-noise ratio (SNR) [20].

2.4.2 Hardware Based Methods

In *Design of a gel-less two-electrode ECG monitor*, an ECG amplifier design specifically to interface two gel-less electrodes for low-power portable applications, is presented. The goal is to develop a circuit with performance sufficient to extract heart rate information reliably using digital signal processing techniques, when measuring a subject engaging in moderate physical activity (such as walking). This application, having no reference electrode, requires biasing of the input to avoid amplifier saturation, all the while maintaining a sufficiently high noise CMR [21].

In *A Comparative Analysis of CMOS Amplifiers for ECG Signals* [22], this paper presents the evolution of the methodologies used for overcoming the faults of various amplification techniques by comparative analysis of amplifiers for better amplification of

ECG signals comprised of either differential amplifier, operational amplifier or Operational Transconductance Amplifiers (OTA) [22].

In *Software Automatic Gain Control for Common Mode Interference Stabilization*, the authors provide initial concepts into automatic gain control (AGC) and applied to ECG applications. They are able to implementing software AGC resulting in maximization the used dynamic range of the ADC and increases the SNR in the digitized signal. In a *Automatic Common Mode Electrode-Amplifier Impedance Balance: Implementation and Results*, by the same authors, design is validates by application in CMR improvement via application to a software phase-locked-loop with the intent of minimizing power-line interference. Results prove that power-line interference is canceled at the hardware level without affecting the spectrum of the useful signal [23], [24].

2.4.3 Summary

Upon reviewing the available literature, it becomes apparent that all the available systems perform acquisition in an open-loop configuration and QA as post-processing. There are available DSP tools to detect and classify ECG noise sources, as well as tools that allow optimization of ECG front-end design for specific acquisitions scenarios. However, there is a lack of interaction between these two components in such a way that allows for dynamic optimization of the front-end characteristics for dynamic conditions, such as the conditions that wearable devices are expected to perform in.

Chapter 3

Methodology

This chapter presents the methodological approach adopted in this project. It provides an overview of the primary and secondary data sources, software resources utilized, and fundamental mathematical concepts employed for signal analysis. Furthermore, a comprehensive set of acquisition contexts in which the developed solution is expected to excel is clearly defined. Finally, a well-defined set of performance metrics and goals is established to guide the evaluation process.

3.1 Hardware Resources

In this section, an overview of the available hardware resources will be provided. These devices are essential for primary data collection in the development of the QA algorithms, can be used as benchmark devices, or serve as tools for hardware development. Note that in Chapter 7, the solution resulting from this project, as described in this document, will also be considered a primary data source.

3.1.1 BITalino

Developed at *Instituto de Telecomunicações* by a multidisciplinary team and formalised by José Guerreiro in *A Biosignal Embedded System for Physiological Computing* as a dissertation for Master's Degree in Electronics and Telecommunications Engineering at ISEL, BITalino, shown in Figure 3.1a, is a versatile platform that integrates multiple measurement sensors for bioelectrical and biomechanical data acquisition, encompassing individual sensor blocks for ECG, Electromiography (EMG), Electrodermal Activity (EDA) and Accelerometry (ACC) [25]. Of particular interest to this project is the ECG sensor block, shown in Figure 3.1b.

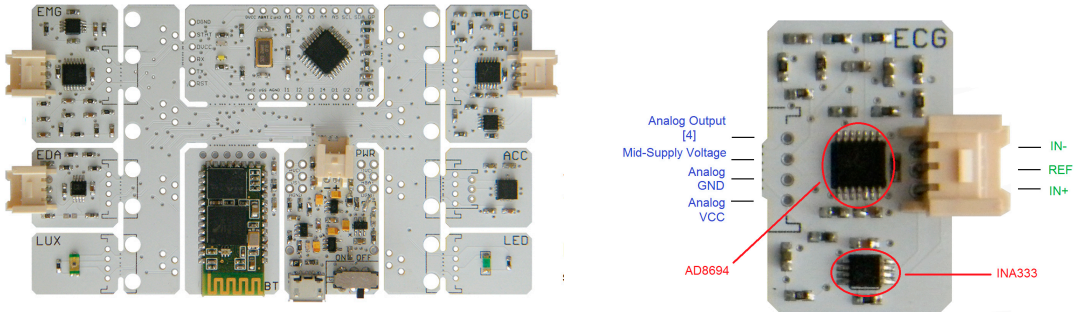

(a) BITalino device.

(b) BITalino ECG sensor block in detail.

Figure 3.1: BITalino. From [25].

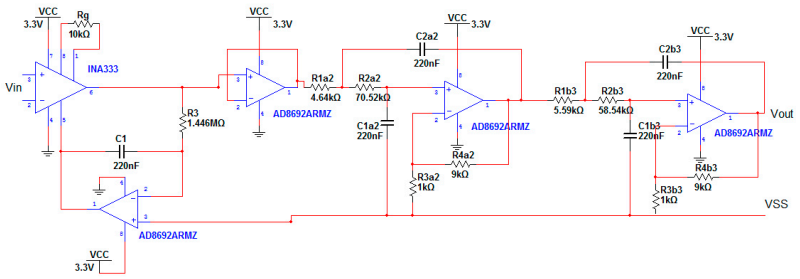

Figure 3.2: BITalino ECG sensor block schematic. From [25].

To measure the low potentials associated with ECG signals, this sensor block includes a Microchip INA333 IA and AD869x operational amplifiers to perform band-pass filtering and amplification.

The first stage of signal conditioning is an AC-coupled instrumentation amplifier circuit. This technique rejects DC input voltages by negative feedback of the amplified output voltage. The following stage is a 4^{th} order low-pass Butterworth filter implemented by cascading two stages of second-order filter used in Sallen-Key architecture [25], shown in Figure 3.2.

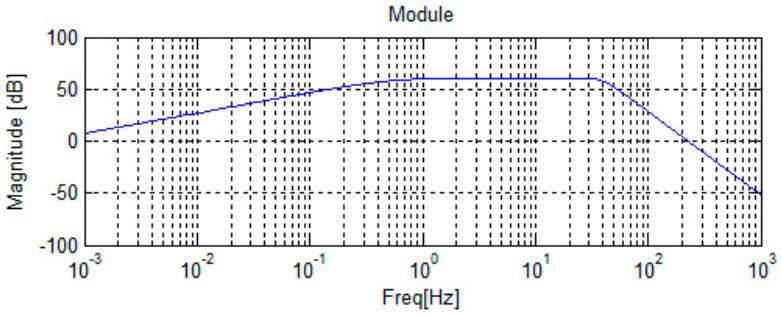

Figure 3.3: BITalino ECG sensor block filtering frequency response. Adapted from [25].

Overall circuit gain is set at 1100 ($60.83dB$), band-pass filtering (attenuation of $3dB$) is set as a 1^{st} order high-pass filter resulting in an attenuation of $20dB/decade$ under $f_{hp} = 0.5Hz$ and the 4^{th} order low-pass Butterworth filter providing an attenuation of $80dB/decade$ above the $40Hz$ and also serving a anti-aliasing function [25]. These characteristics are summarized in table 3.1.

Table 3.1: BITalino basic front-end characteristics.

Parameter	Value	Units
f_{hp}	0.5	Hz
IA Gain	11	V/V
Total AFE Gain	1100	V/V

3.1.2 IMSC Project

Developed as part of *Instrumentação Médica: Sensores e Circuitos* (IMSC) course at ISEL, the aim of this project was to design and implement several essential hardware and software components for the acquisition of ECG. The design included signal conditioning blocks, analog-to-digital conversion as well as post processing.

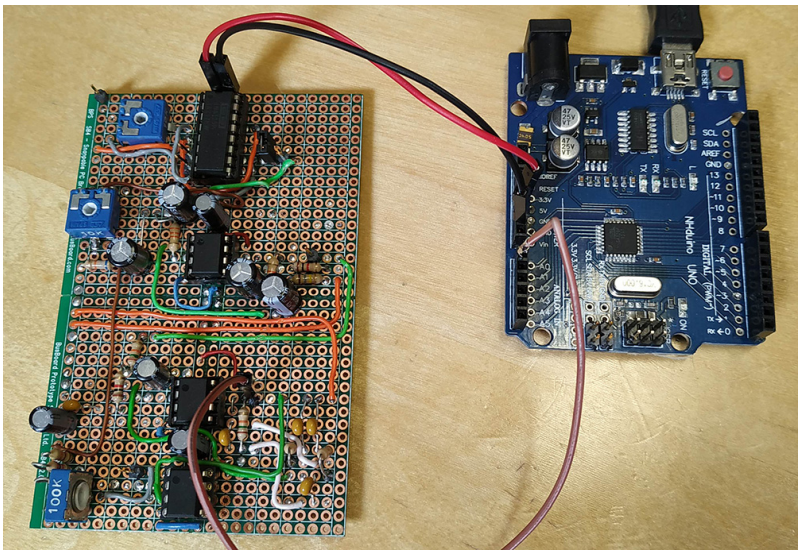

Figure 3.4: IMSC Project.

The developed solution was based on a INA125P IA, and in shown in Figure 3.4. The remainder of the components provide the required filtering and amplification for successful signal conditioning. Acquisition was performed with an ATmega328 MCU on a Arduino UNO board interfacing with a Personal Computer (PC) via Universal Serial Bus (USB). The acquired signal was able to be recorded for post-processing.

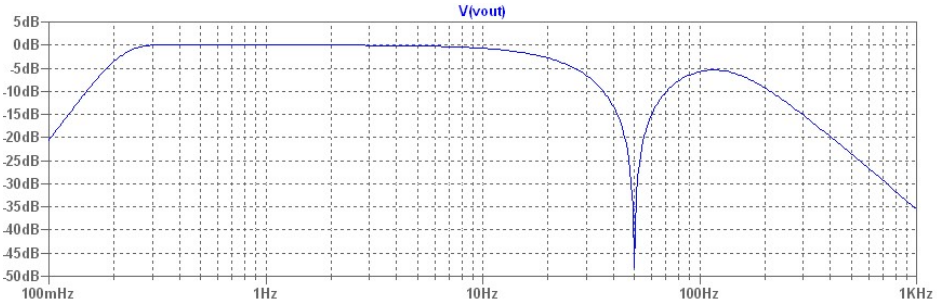

Figure 3.5: IMSC Project filtering frequency response.

Band-pass filtering (attenuation of $3dB$) is set as a 4^{th} order high-pass filter resulting in an attenuation of $80dB/decad$e under $0.25Hz$ and the 2^{nd} order low-pass Butterworth filter providing an attenuation of $40dB/decade$ above the $130Hz$ and also serving a anti-aliasing function.

$$Q = \frac{f_m}{f_{3dB}} = 0.25 \tag{3.1}$$

Additionally there is a narrow-band notch filter with f_m set at local power line frequency of $50Hz$ in a $Twin\text{-}T$ configuration. This filter topology has the drawback of a low Q factor fixed at $Q = 0.25$. As per Equation 3.1, with $f_m = 50Hz$ the rejection band corner frequencies (attenuation of $3dB$) are calculated to be from $20Hz$ to $200Hz$.

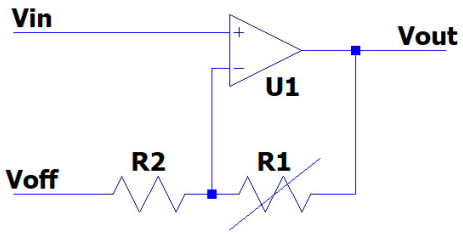

Figure 3.6: ADC dynamic range maximizing stage.

$$A_v = 1 + \frac{R_1}{R_2} \tag{3.2}$$

Another functionality of this project was an additional gain stage at the end of the chain design to maximize the Arduino UNO 10-bit ADC. This circuit was based on a non-inverting amplifier from Figure 3.6 and Equation 3.2 sets circuit gain. The control voltage V_{off} sets the center voltage of this circuit, thereby maximizing the ADC. Both the gain and center voltage were set manually via trimmer resistors in this circuit.

3.1.3 CardioID CardioWheel

CardioWheel is an Advanced Driver Assistance System (ADAS) that acquires the ECG to continuously detect drowsiness, cardiac health problems and perform biometric identity recognition, shown in Figure 3.7a.

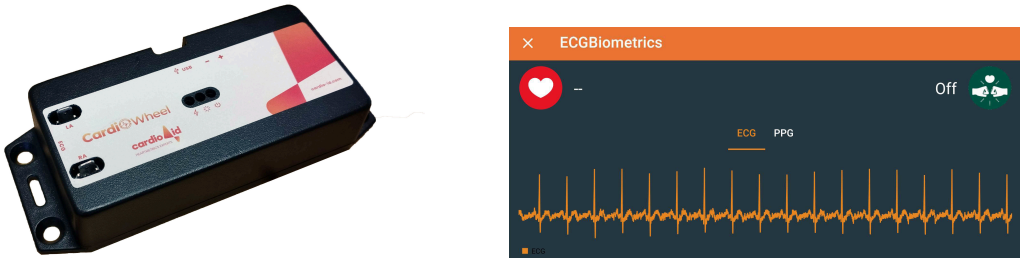

(a) CardioWheel device. (b) ECG Biometrics app.

Figure 3.7: CardioID CardioWheel.

CardioWheel was developed as a solution for automotive applications, performing ECG acquisition from the driver's hands while holding the steering wheel. It is comprised of an analog front-end that acquires 1-channel ECG signal, a processing unit that performs signal processing and biometric evaluation, and a Bluetooth Low Energy (BLE) wireless communication interface that can interface with a smart-phone app. The capability to be battery-powered, making the unit completely wireless, enables CardioWheel to perform ECG monitoring as a wearable device. CardioWheel utilizes a custom implementation of the AD8232 integrated amplifier and signal conditioning block for ECG. It is designed to extract, amplify, and filter small biopotential signals in the presence of noisy conditions.

This device interfaces with the Android app *ECG Biometrics*, shown in Figure 3.7b, which connects to the CardioWheel device via Bluetooth. The app is able to perform ECG signal recording, storing the acquisition information on a smartphone device.

3.1.4 Non-Intrusive ECG Acquisition Test-bed

One major hurdle to overcome in ECG signal acquisition is systematic and reproducible testing over varying hardware and subjects under test. Human factors such as weight, age

or physical aptitude and technical factors such as circuit topology, front-end frequency response or skin-electrode impedance all affect the output signal. In order to fine tune a quality assessment algorithm these varying factors have to be controlled.

Developed by Daniel Almeida the *Non-Intrusive ECG Acquisition Test-bed* as a dissertation for Master's Degree in Electronics and Telecommunications Engineering at ISEL, this device is able to connect to any ECG AFE and reproduce any desired wave form. This device is also able to perform simulation of the skin electrode equivalent circuit for different applications [26], shown in Figure 3.8.

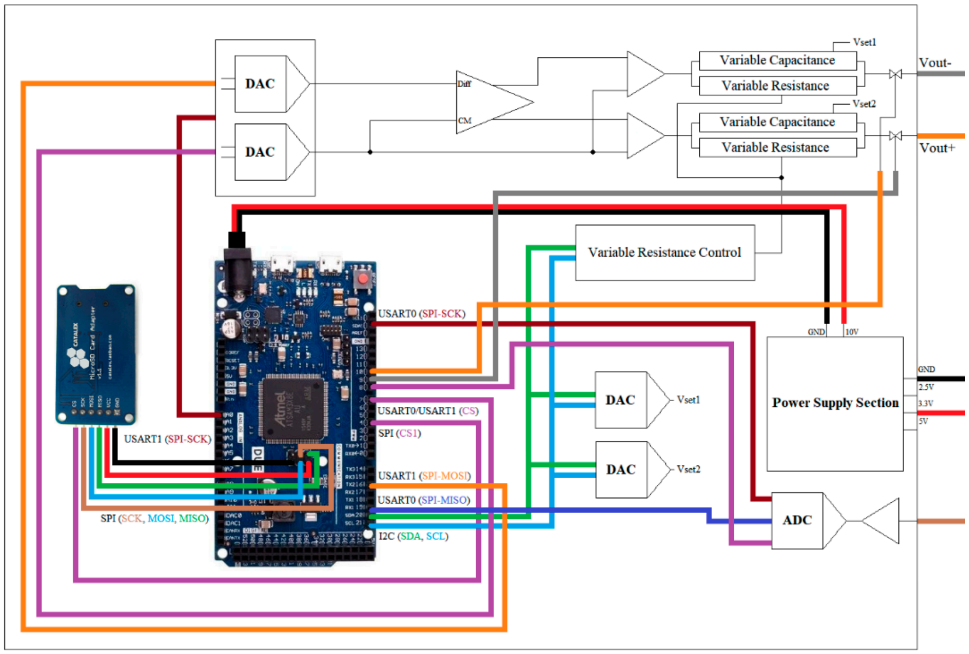

Figure 3.8: Schematic representation of the ECG test system, showing MCU connections. From [26].

This device will allow for systematic testing of any ECG front-end by the removal of the human factor and providing control over the technical factors.

3.1.5 Agilent 33250A Arbitrary Waveform Generator

The Agilent Technologies 33250A is a high-performance $80MHz$ synthesized function generator with built-in arbitrary waveform and pulse capabilities [27]. Of particular interest to this project was the *cardiac* waveform displayed in Figure 3.9, which allowed control over the input signal characteristics, proving itself to be a valuable tool in the early stages of development and fine-tuning of the AFE filtering.

Figure 3.9: Agilent 33250A "cardiac" waveform. Picture from [27].

3.2 Secondary Data Sources

This project will use existing medical-grade ECG recordings as a source of secondary data. These recordings will allow for validation of the QA algorithm prior to hardware design.

The *Computing in Cardiology Challenge 2011 (CinC11) Training Dataset* is a collection of 1000 twelve-lead ECG, each with a minimum length of 10 seconds with full diagnostic bandwidth (0.05 through $100Hz$). It is used as a training set for the *PhysioNet/Computers in Cardiology Challenge 2011*, which entailed determining which of the recordings in the set are acceptable for interpretation [28].

The *MIT-BIH Arrhythmia* and *MIT-BIH Noise Stress Databases* were recorded between 1975 and 1979 in the Boston's Beth Israel Hospital (now the Beth Israel Deaconess Medical Center) to support MIT research into arrhythmia analysis and related subjects. The recordings were digitized at 360 samples per second per channel with 11-bit resolution over a $10mV$ range, and two or more cardiologists independently annotated each recording. This data is freely available and encompassed by *Open Data Commons Attribution License (ODC-By)* [29].

The *MIT-BIH Arrhythmia Database* was the first generally available set of standard test material for evaluation of arrhythmia detectors. It provides 48 half-hour excerpts of two-channel ambulatory ECG recordings obtained from 47 subjects studied by the BIH Arrhythmia Laboratory. [30]

The *MIT-BIH Noise Stress Database* provides a realistic simulation of real-world noisy ECG recordings. This database includes 12 half-hour ECG recordings and 3 half-hour recordings of noise typical in ambulatory ECG recordings. The ECG recordings were created using two clean recordings (118 and 119) from the *MIT-BIH Arrhythmia Database*, to which calibrated amounts of noise were added. [31]

3.3 Software Resources

- **Circuit Simulation:** LTSpice v17.0.22.0
- **PCB Design:** Altium Designer v20.2.5
- **MCU Programming:**
  - Thonny v3.3.13 running Python v3.7.9 - Thonny's is a integrated development environment supporting MicroPython. Initial development was performed at the Institute of Computer Science of University of Tartu, Estonia, and is supported by the Raspberry Pi Foundation. This software was used for Raspberry Pi Pico firmware development.
  - Arduino IDE v1.8.19 - This software was used for Arduino H7 Portenta firmware development.
- **Signal Processing & Graphical User Interface:**
  - MATLAB 9.10.0.1602886 (R2021a).
  - Anaconda v2020.11 and Spyder 4.1.5 running Python 3.8.5.

3.4 Methods of Analysis

3.4.1 Fourier analysis

One of the most well-known method of signal analysis is Fourier analysis which breaks down a signal into constituent frequencies, an infinite number of sine/cosine waves (harmonics), and may be regarded as a mathematical technique for transforming the signal

from the time domain to the frequency domain. For a continuous signal $x(t)$, the Fourier Transform (FT) is defined as follows:

$$X(f) = \int_{-\infty}^{\infty} x(t)e^{-j2\pi ft}dt \tag{3.3}$$

The analysis coefficients, also called spectra $F(\omega)$, are calculated as inner products of the signal with sinusoidal basis functions of infinite duration.

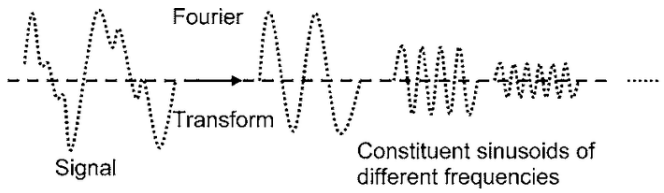

Figure 3.10: FT of a signal - graphical representation. Adapted from [32].

Time domain and frequency domain constitute two alternative ways of looking at a signal. The FT serves as a bridge between these domains, facilitating the transition between them, although it does not allow for a simultaneous combination of both. Instead, it excels in analyzing harmonic signals or those where local information is not a prerequisite.

One limitation of the FT is the absence of time information, making it impossible to determine the exact timing of specific events within a signal. Many signals possess transient characteristics such as drifts, trends, abrupt changes, and the initiation and conclusion of events. These transient features often constitute the most significant aspects of a signal and cannot be fully comprehended through Fourier analysis alone.

Physiological signals, such as the ECG, are inherently non-stationary, necessitating a unified time-frequency interpretation. The concept of a time-frequency representation for signals aims to transform a one-dimensional signal of time, $x(t)$, into a two-dimensional function that encompasses both time and frequency domains. Doing so, seamlessly combines the temporal and spectral aspects of the signal.

In 1946, Dennis Gabor (1900-1979) introduced the concept of the windowed FT, also known as the Short Time Fourier Transform (STFT). The idea behind this approach was to utilize a time-localization window function, denoted as $g(t-\tau)$, to extract localized information from the FT. The parameter τ represents the window's position in time, and by varying τ, the window is shifted across the entire time domain, effectively covering the entire signal.

$$\mathrm{STFT}_x^g(\tau, f) = \int_{-\infty}^{+\infty} x(t)g(t-\tau)e^{-j2\pi ft}dt \tag{3.4}$$

While the Short Time Fourier Transform (STFT) addresses the limitations of the Fourier Transform (FT), it introduces a challenge regarding time and frequency resolution. This issue arises from the fundamental concept known as the *uncertainty principle*, which states that a signal cannot have an exact time-frequency representation simultaneously [33]. Spectral components at each time instant cannot be precisely determined. We can only identify the time interval of a specific frequency band. A wider window enhances frequency resolution but sacrifices time resolution, while a shorter window improves time resolution at the expense of frequency resolution. Once the window is chosen for the STFT, the time-frequency resolution remains fixed. However, practical signals, such as ECG, often demand a more flexible approach to achieve the desired resolution.

3.4.2 Wavelet analysis

The Wavelet Transform (WT) is a mathematical tool for analyzing signals and functions, designed to address the limitations of the STFT. It decomposes a signal into compactly supported basis functions called wavelets, derived from a single prototype wavelet through dilation and translation.

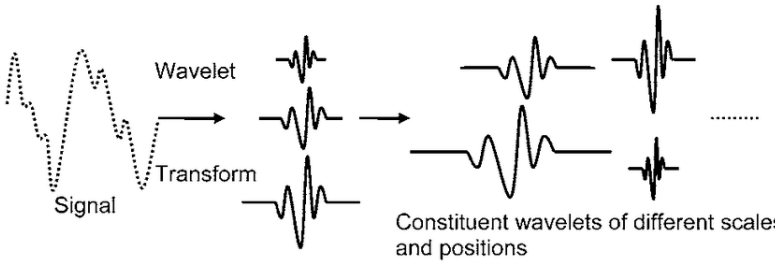

Figure 3.11: WT of a signal - graphical representation. Adapted from [32].

Contrary to the FT, wavelets are aperiodic, irregular, and localized waves of energy. Wavelets have their energy concentrated in time or space, making them suitable for analyzing transient signals. These signals often contain non-periodic components and high-frequency content with a significant magnitude, unlike harmonic signals.

The Continuous Wavelet Transform (CWT), $\omega(s,\tau)$, of a signal $x(t)$ is defined by the inner product of the signal and a scaled and translated version of a single prototype wavelet ψ and can be described as:

$$\omega(s,\tau) = \int_{-\infty}^{+\infty} x(t)\frac{1}{\sqrt{s}}\psi\left(\frac{t-\tau}{s}\right)dt \tag{3.5}$$

Equation 3.5 can also be interpreted as a linear filtering operation between the signal $x(t)$ and a filter of impulse response $\frac{1}{\sqrt{s}}\psi\left(\frac{-t}{s}\right)$.

In wavelet analysis, the parameter τ represents the translation of the wavelet, while s denotes the dilation parameter or scale factor. Scaling a wavelet involves stretching or compressing it. A greater stretching of the wavelet corresponds to comparing it with a longer portion of the signal, resulting in coarser measurements of signal features captured by the wavelet coefficients. This establishes a relationship between wavelet scale and frequency in wavelet analysis. A lower scale indicates a compressed wavelet, capturing rapidly changing details in high frequency. On the other hand, a higher scale represents a stretched wavelet, capturing slowly changing features and low frequency components, as shown in Figure 3.11.

When dyadic (powers of two) scales and positions are selected, the analysis is referred to as the Discrete Wavelet Transform (DWT). The DWT is known for its efficiency and accuracy, making it a favorable alternative to the CWT [3], [32]. The DWT is based on the sampling of the translation-scale plane by using dyadic sampling of the two parameter:

$$s = 2^{-j}, \tau = k2{-}j; s, \tau \in \mathbb{Z} \tag{3.6}$$

The discretized wavelet function is then defined by:

$$\psi j, k(t) = 2^{j/2}\psi(2^j t - k) \tag{3.7}$$

Inserting into CWT Equation 3.5, we obtain:

$$DWT_x^{\psi}(j,k) = \int_{-\infty}^{+\infty} x(t)\psi_{j,k}(t)dt = 2^{j/2}\int_{-\infty}^{+\infty} x(t)\psi(2^j t - k)dt \tag{3.8}$$

A signal can be viewed as the sum of a coarse part and a detailed part. the smooth part reflects the main features of the signal, therefore called the approximation signal, whereas the faster fluctuations represent the details of the signal.

The signal separation into two parts is determined by the resolution of analysis. Increasing the resolution provides a better approximation of the signal by including finer details. The approximation of the signal $x(t)$ at scale j is denoted as $x_j(t)$, and at the next scale $j+1$, the approximation x_{j+1}(t) is composed of $x_j(t)$ and the details $y_j(t)$ at that level such that:

$$x_{j+1}(t) = x_j(t) + y_j(t) \tag{3.9}$$

By adding detail to $x_j(t)$, we achieve a dyadic multiresolution representation of the signal $x(t)$, comprising a smooth part and a sum of various details:

$$x(t) = x_j(t) + \sum_{k=j}^{\infty} y_k(t) \tag{3.10}$$

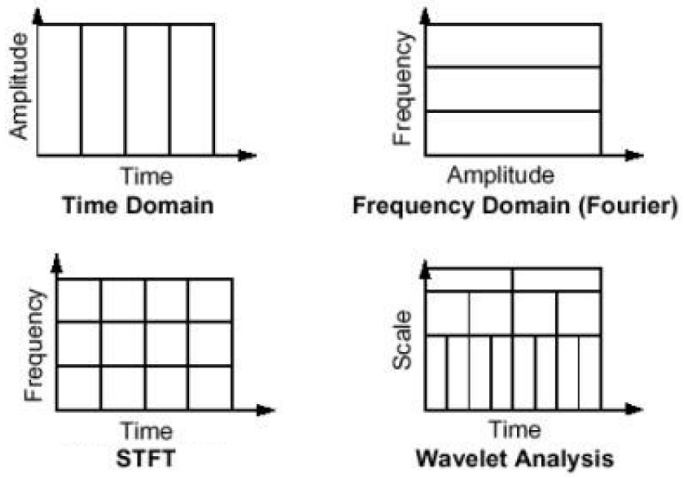

Figure 3.12: Different signal representation methods. Adapted from [3]

Figure 3.12 compares the resolution of four signal representations of $x(t)$.

The original time-domain signal has got no time resolution problem, since we know the value of the signal at every instant of time. The Fourier transformed version provides accurate frequency information but lacks resolution in the time domain. In the two bottom diagrams, each box represents an equal area of the time-frequency plane, but with varying sizes, provide different proportions to time and frequency. All the boxes have the same size in the STFT representation, meaning that the time and frequency resolutions remain constant across the entire time-frequency plane. In wavelet transform, at low frequencies (high scales), the boxes have shorter heights, indicating better frequency resolution due to less ambiguity in the exact frequency value. However, their widths are longer, indicating poorer time resolution with more ambiguity in the exact time value. Conversely, at higher frequencies (low scales), the width of the boxes decreases, leading to improved time resolution, while the height of the boxes increases, resulting in decreased frequency resolution.

Analogously to dyadic sampling of the wavelet function, Equation 3.7, equation $\varphi(t)$, an also be generalized through dyadic sampling. This allows for the generation of a set of orthonormal scaling functions, enabling approximations at different resolutions.

$$\varphi j, k(t) = 2^{j/2}\varphi(2^j t - k) \tag{3.11}$$

Orthonormality applies only to different translation indices k for a fixed scale j, and the scaling functions are thus not required to be orthonormal between different scales. With these basis functions, the approximation signal $x_j(t)$ is given by:

$$x_j(t) = \sum_{n=-\infty}^{\infty} c_j(n)\varphi_{j,n}(t) = 2^{j/2} \sum_{n=-\infty}^{\infty} c_j(n)\varphi(2^j t - n) \tag{3.12}$$

where:

$$c_j(k) = \int_{-\infty}^{+\infty} x(t)\varphi_{j,k}(t)dt \tag{3.13}$$

It is crucial to recognize that as j increases above 0, the temporal span expands due to the contraction of $\varphi_{j,n}(t)$. Consequently, the approximation signal $x_j(t)$ becomes capable of better representing the finer details of $x(t)$. Conversely, when j is negative, $\varphi_{j,n}(t)$ expands, limiting the representation to coarser information.

The same mathematical interpretation can be make for Equation 3.7.

$$y_j(t) = \sum_{n=-\infty}^{\infty} d_j(n)\psi_{j,n}(t) = 2^{j/2} \sum_{n=-\infty}^{\infty} c_j(n)\psi(2^j t - n) \tag{3.14}$$

where:

$$d_j(k) = \int_{-\infty}^{+\infty} x(t)\psi_{j,k}(t)dt \tag{3.15}$$

This equation described the wavelet coefficient. Providing a correlation or similarity between the original signal $x(t)$ and the wavelet function $\psi_{j,k}(t)$ at a specific scale and position. At scale j_0, the signal $x(t)$ can be expressed as a wavelet series expansion in terms of the *scaling coefficients* $c_j(k)$ and the *wavelet coefficients* $d_j(k)$:

$$x(t) = \sum_{n=-\infty}^{\infty} c_{j0}(n)\psi_{j0,n}(t) + \sum_{j=j0}^{\infty} \sum_{n=-\infty}^{\infty} d_j(n)\psi_{j,n}(t) \tag{3.16}$$

The expression combines the scaling coefficients and wavelet coefficients at different scales and positions to reconstruct the original signal. The scaling coefficients, denoted as $c_{j0}(n)$, represent the low-frequency components of the signal at the coarsest scale j_0 and position n. They are used to approximate the signal. The wavelet function at the initial scale j_0 and position n, denoted as $\psi_{j0,n}(t)$, serves as a basis function to capture the low-frequency components. On the other hand, the wavelet coefficients $d_j(n)$ represent the high-frequency details or the difference between the original signal and the approximations at different scales j and positions n. The wavelet function $\psi_{j,n}(t)$, at scale j and position n, acts as a basis function to capture the high-frequency components of the signal. The first term of the expression corresponds to the approximation or the low-frequency components of the signal at the initial scale. It is obtained by multiplying the scaling coefficients with the corresponding wavelet functions. The second term represents the details or the high-frequency components at progressively finer scales. It involves summing up the wavelet coefficients multiplied by the respective wavelet functions. The given expression enables the reconstruction of the original signal by combining the scaling coefficients and wavelet coefficients, capturing both low and high-frequency components at different scales and positions.

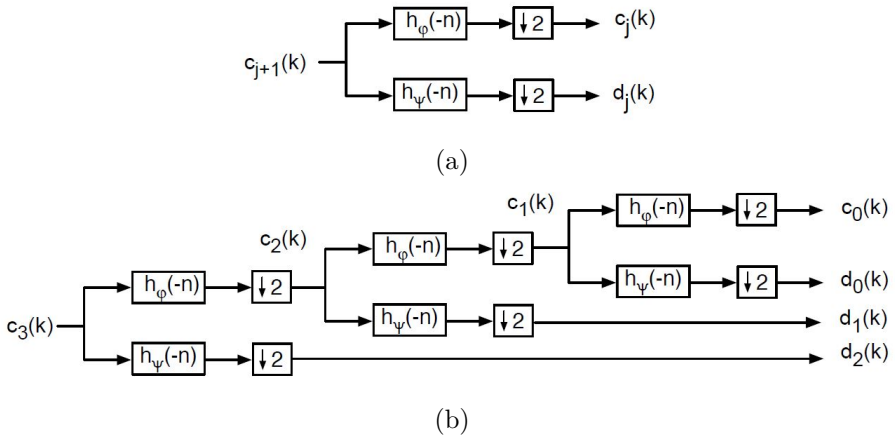

Figure 3.13: Calculation of the DWT coefficients implemented using the two-channel analysis filter bank.

The two-channel analysis filter bank is a widely used method for wavelet decomposition and reconstruction. It is visualized in Figure 3.13 as a graphical representation of the process.

In Figure 3.13a, a two-channel filter bank is depicted. This filter bank is responsible for calculating the coefficients of the wavelet series expansion. The original signal is fed into the filter bank, which separates it into two components: the low-frequency components and the high-frequency components. The operation of the filter bank involves downsampling, this serves multiple purposes and brings several advantages. Firstly, it enhances computational efficiency by reducing the number of samples that need to be processed. Secondly, it enables multiresolution analysis, allowing the capture of frequency information at different scales. Additionally, downsampling facilitates the separation of frequencies, as the low-frequency components are preserved while the high-frequency components are isolated. Lastly, downsampling helps in maintaining orthogonality between the analysis and synthesis filter banks, which is crucial for accurate signal reconstruction. In Figure 3.13b, the DWT based on the filter bank in Figure 3.13a is depicted. In this case, the process is applied recursively to the approximation coefficients, leading to multiple levels of decomposition. This recursive nature allows for a hierarchical representation of the signal, with each level capturing different frequency details and approximations. The resulting decomposition provides a comprehensive analysis of the signal's frequency content at different scales.

It is also possible to reconstruct the original signal from the wavelet coefficients (approximation and detail coefficients), this process is named synthesis, inverse DWT or IDWT. This process is the reverse of the analysis step and involves upsampling and filtering.

Figure 3.14 aims to provide a visual representation of this process. In Figure 3.14a displays a two-channel synthesis filter bank. In Figure 3.14b the DWT based on the filterbank in Figure 3.14a, which, is repeated iteratively, using the approximation coefficients from each level, until the original signal is fully reconstructed. The synthesis step restores the original signal by upsampling the coefficients and applying appropriate synthesis filters to recover both the low-frequency approximations and the high-frequency details. It allows for the reconstruction of the signal with minimal loss of information. This process is essential for signal reconstruction and recovery of the original signal from its wavelet coefficients. It completes the full cycle of the DWT analysis and synthesis, enabling the application of wavelet-based techniques such as denoising, compression, and signal processing.

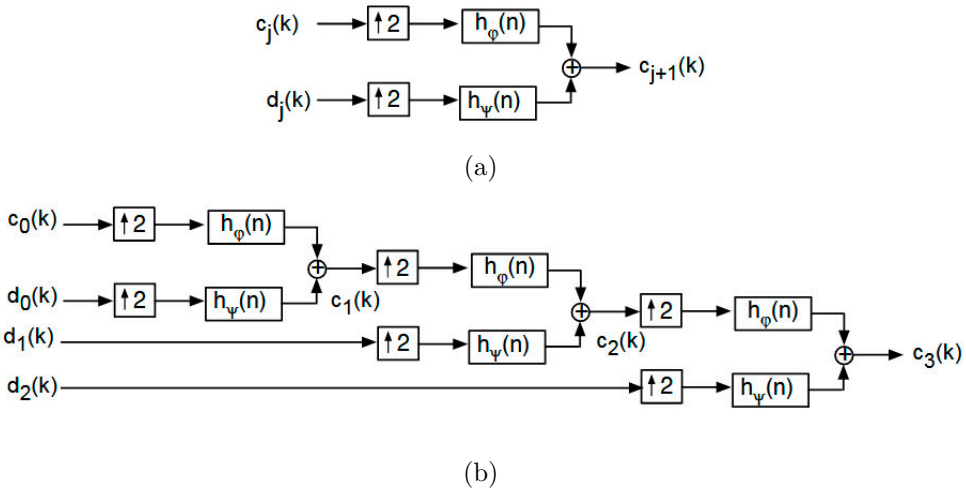

Figure 3.14: Calculation of the DWT coefficients implemented using the two-channel synthesis filter bank.

It is also possible to perform a partial DWT reconstruction by selectively using a subset of the wavelet coefficients. Partial DWT reconstruction is useful in situations where specific frequency bands are desired. It allows for trade-offs between computational efficiency and signal fidelity, depending on the specific application or analysis requirements.

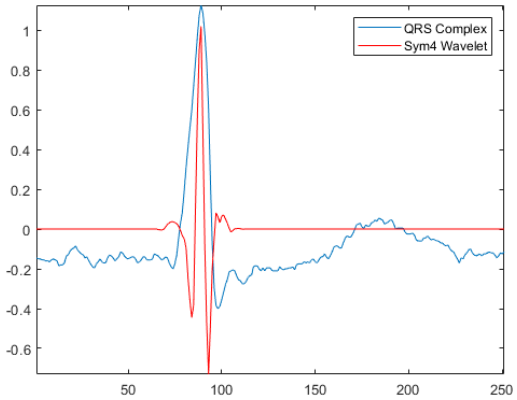

Figure 3.15: Comparison of Sym4 Wavelet and QRS Complex. Adapted from [34].

An example of a decomposition analysis of the ECG signal is shown in Figure 3.16. The ECG signal was treated with DWT in the Python software environment using the wavelet shown in Figure 3.15.

Regarding Figure 3.16, the original signal is decomposed in approximation (cA) and details (cD). The first level approximation (cA) is further analyzed and decomposed into a second level approximation signal ($cA2$) and details ($cD2$). The reconstructed signal is compared to the original signal to examine how much information was lost during the wavelet transformation. Note that, in the present work, the wavelet analysis is employed to identify the most important ECG signal features and quantify their amplitude rather than to de-noise a signal.

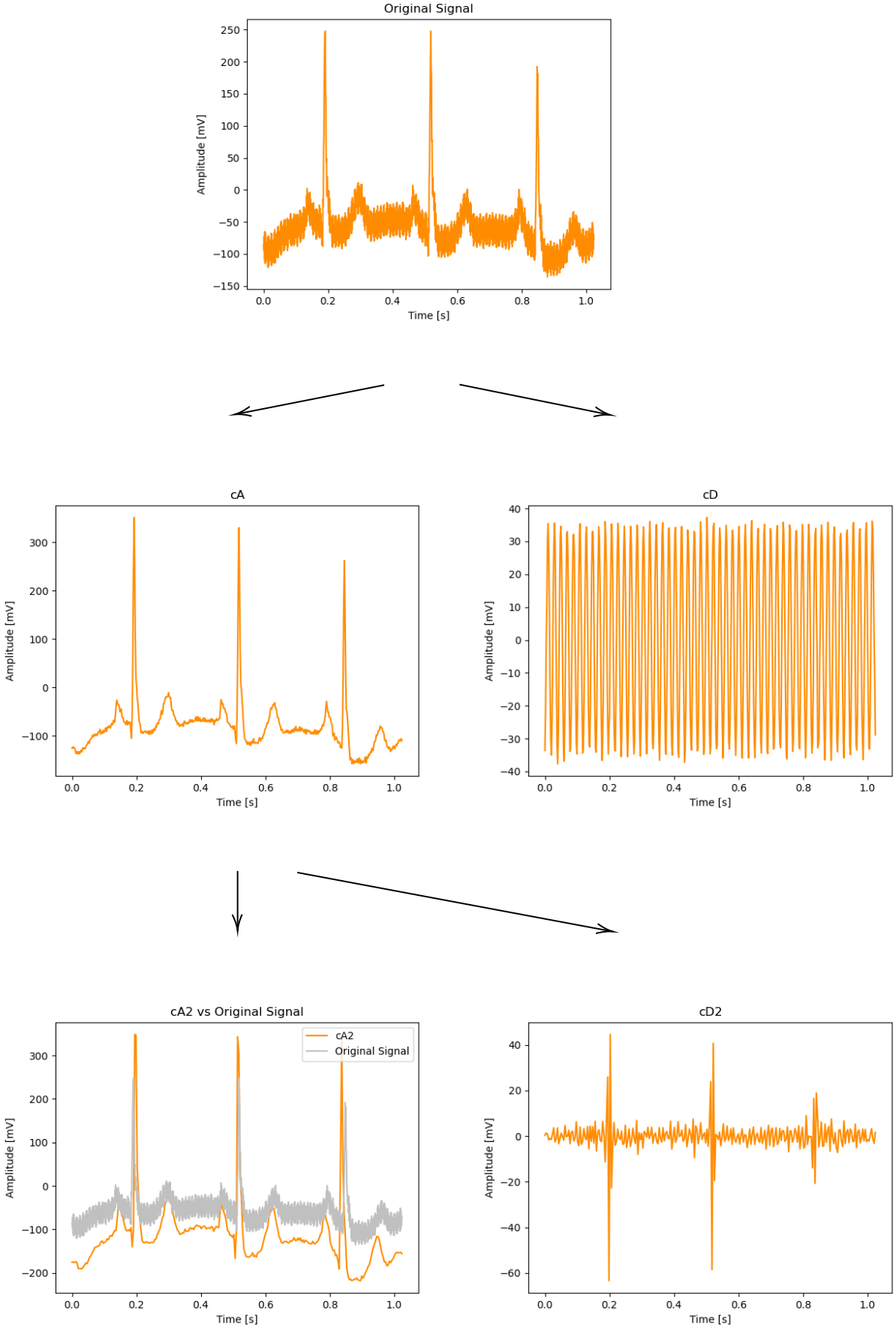

Figure 3.16: ECG signal decomposition, de-noising, and reconstruction.

3.5 Acquisition Contexts

In the section the scenarios in which the developed solution performance will be tested are described.

3.5.1 Resting Acquisition

The primary acquisition scenario involves acquiring data from the test subject in a resting state, similar to a standard ECG. The recordings will be conducted in a Lead-I configuration.

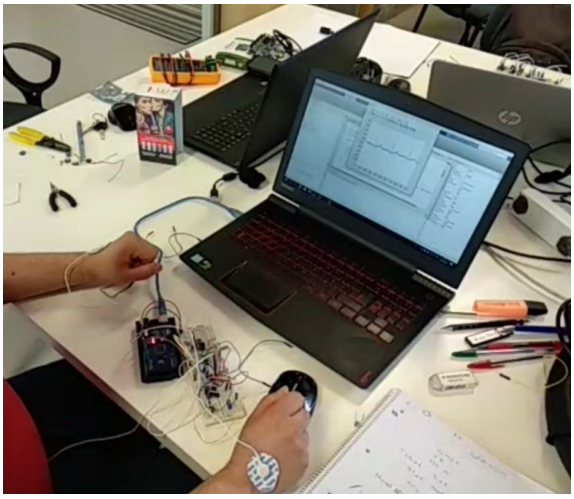

Figure 3.17: Resting acquisition with IMSC project in development.

3.5.2 Moving Acquisition

The system will be tested under dynamic conditions to simulate wearable device usage.

Figure 3.18: Wearable device example - Chest-strap heart monitors.

3.5.3 Vehicle Simulator Acquisition

ISEL (*Instituto Superior de Engenharia de Lisboa*) houses a vehicle simulator developed as part of IDI&CA 2020 project HANDVISOR. This full-scale driving simulator serves as a platform for multidisciplinary research on monitoring technologies for assessing the driver's psychophysiological state. Additionally, it incorporates natural interfaces with the car cockpit to enhance the research capabilities and overall simulation experience.

Figure 3.19: Simulator acquisition setup.

3.5.4 In-car Acquisition

Figure 3.20: In-car Acquisition.

In terms of applying the knowledge and expertise gained from this project to automotive applications, particularly in collaboration with CardioID and the i-DREAMS project, the developed system will undergo testing for an in-vehicle application. The focus will be on enhancing the quality of the ECG measurements in real-time, leveraging the advancements achieved through this project.

3.6 Performance Metrics

The system's performance will be evaluated using both qualitative and quantitative measures across the following parameters:

1. Ability to dynamically control essential AFE parameters.
2. Effectiveness of ECG acquisition while accurately identifying various types of noises.
3. Dynamic optimization of ECG signal acquisition across diverse test subjects and scenarios.
4. Percentage improvement over existing systems.

Chapter 4

ECG Quality Assessment Algorithm

In the following sections, a step-by-step formulation of the proposed algorithm for ECG QA will be presented.

4.1 Wavelet Analysis of ECG Signal

Wavelet decomposition is the widely used signal processing tool for extracting the features used in R-peak detection, ECG characteristics points delineation, compression, and many other different ECG analysis applications. It provides clinically acceptable detection rates with low computing power requirements [3].

Since temporal and spectral information about ECG local waves and different low-frequency and high-frequency noises are available, the wavelet transform can be utilized to decompose the signal into different frequency sub-signals.

The main advantage of wavelet analysis is that it provides spectral information of the signal in each sub-band. From the decompositions, various time-domain global and local features including amplitude-dependent threshold, zero-crossings, kurtosis, auto-correlation first maximum peak, auto-correlation decaying function are extracted for detection, localization and classification of different ECG noises.

Fully detailed ECG signal wavelet decomposition is provided in Figure A.1, in appendix.

4.2 Classification ECG noises

The noise detection problem is usually formulated as a hypothesis testing problem given by:

$$H = \begin{cases} 1: & noise\ present \\ 0: & noise\ absent \end{cases} \tag{4.1}$$

Where H is a boolean hypothesis for detecting the presence of noise. Noise will be categorize it into one of the following classes:

- H_1 : Baseline wander
- H_2 : Saturation
- H_3 : Power Line Interference

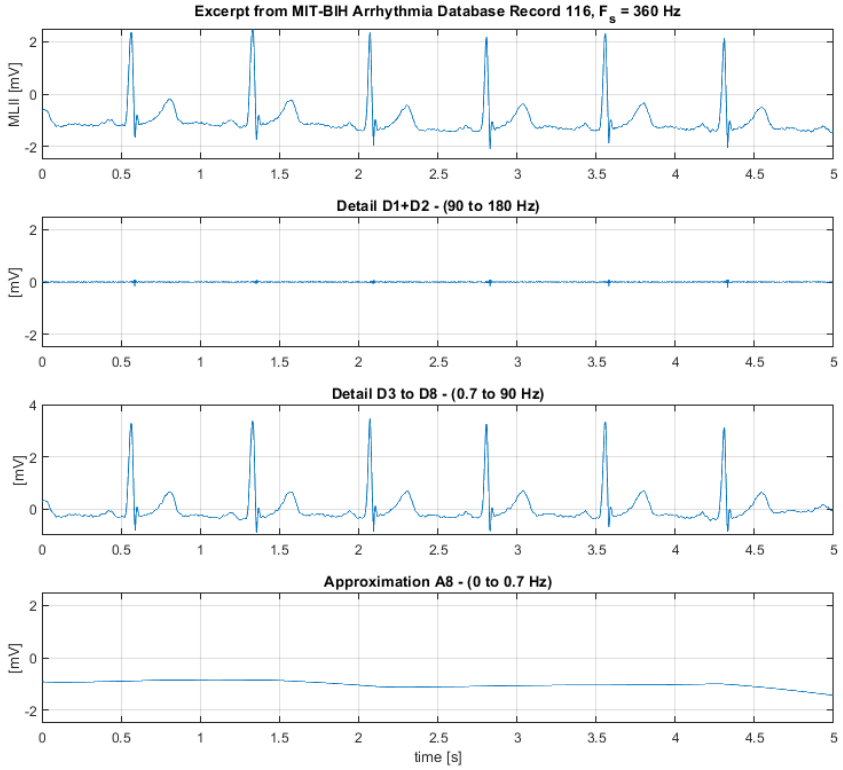

Figure 4.1: Wavelet Decomposition of ECG Signal.

4.2.1 Baseline wander detection

As mentioned earlier, BW is one of the predominant LF noise that affects the ECG signal. The maximum frequency content of the BW lies below $1Hz$ and hence BW is captured in the last level of decomposition (A8). The detection hypothesis H_1 is given by:

$$H_1 = \begin{cases} 1: & \{min|x_b(n)|\} < \gamma_{BW} \quad \vee \quad \{max|x_b(n)|\} < (1-\gamma_{BW}) \\ 0: & otherwise \end{cases} \tag{4.2}$$

```
% Baseline Wander Detection
load('MIT-BIH\115m.mat');% Load signal to "val" matrix
ECGSignal = val; % Conversion to mv
ECGSignal(2,:)=[]; % Remove Ch 2
t0 = 110; % Acq Start
t= 60; % Acq Time
ECGSignal = ECGSignal( t0*Fs : (t0+t)*Fs );

% Perform a multilevel wavelet decomposition of a signal.
[C,L] = wavedec(s,8,'sym4');
% Reconstruct the Level 8
A8 = wrcoef('a',C,L,'sym4',8);

% Detect BW
BW = abs(A8) > Y_BW;
```

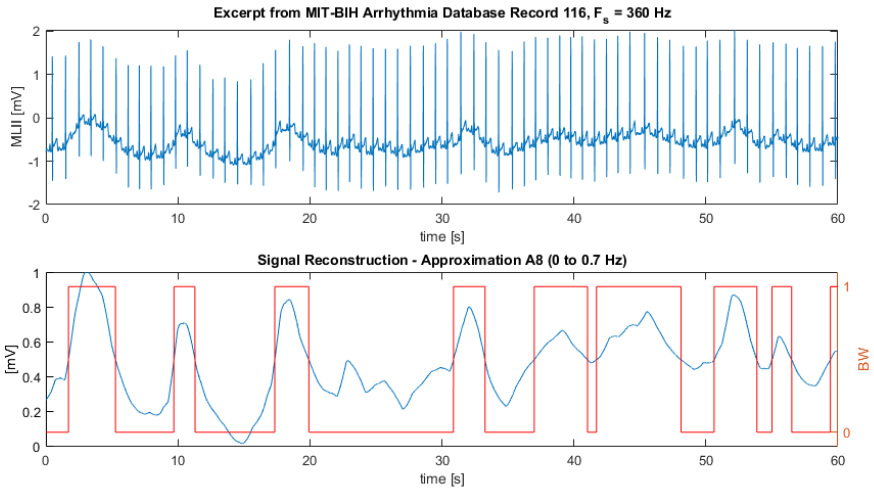

Figure 4.2: BW detection example.

4.2.2 Saturation detection

SAT is characterised by a zero amplitude DC line, this can be seen as a pause in the signal as illustrated in Figure 2.22. SAT detection can be formed by:

$$H_2a = \begin{cases} 1: & H_2a \quad \vee \quad H_2b \\ 0: & otherwise \end{cases} \tag{4.3}$$

Where H_2 is the detection hypothesis for detecting the SAT and γ_f is the amplitude threshold.

$$H_2a = \begin{cases} 1: & \{min|x_b(n)|\} < \gamma_{SAT_1} \quad \vee \quad \{max|x_b(n)|\} < (1 - \gamma_{SAT_1}) \\ 0: & otherwise \end{cases} \tag{4.4}$$

The MATLAB implementation of this conditions would be as follows:

```
% Baseline Wander Detection
load('MIT-BIH\116m.mat'); % Load signal to "val" matrix
ECGSignal = val; % Conversion to mv
ECGSignal(2,:)=[]; % Remove Ch 2
t0 = 1385; % Acq Start
t= 30; % Acq Time
ECGSignal = ECGSignal( t0*Fs : (t0+t)*Fs );
t=(0:length(ECGSignal)-1)/Fs;

% Perform a multilevel wavelet decomposition of a signal.
[C,L] = wavedec(s,8,'sym4');
% Reconstruct the Level 8
A8 = wrcoef('a',C,L,'sym4',8);

% Detect SAT
SAT = abs(A8) > Y_SAT;
```

The result of the algorithm is displayed in Figure 4.3.

Another option to detect SAT would be analysing spectral content using the Fast Fourier Transform (FFT).

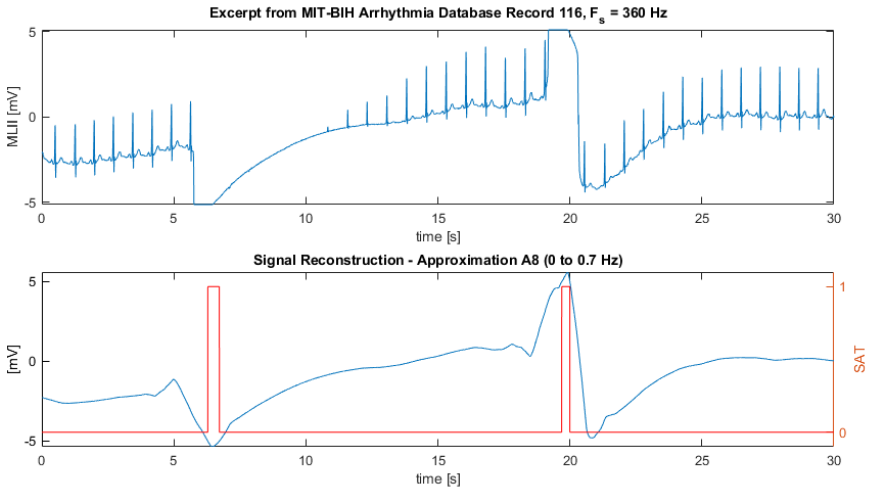

Figure 4.3: SAT detection example.

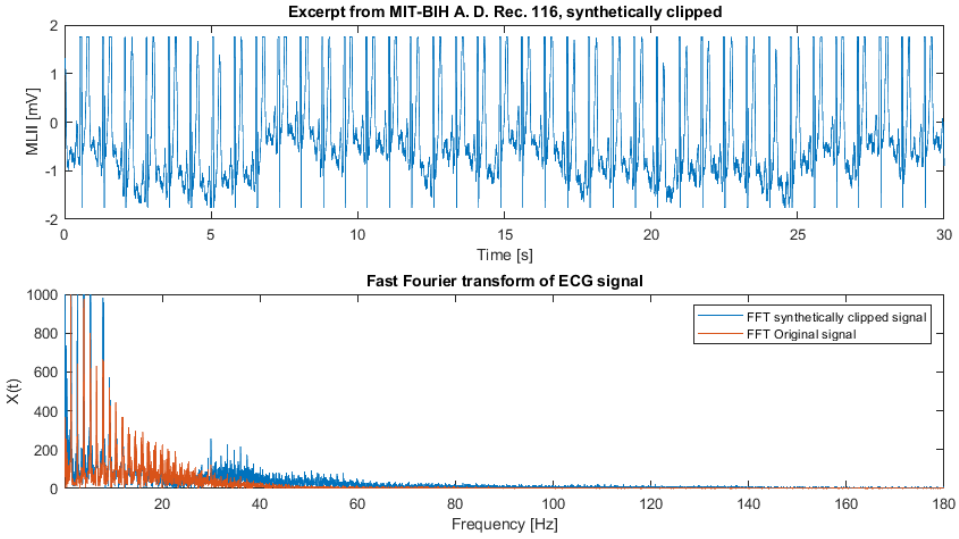

Figure 4.4: FFT of ECG Signal - Synthetically clipped.

$$H_2b = \begin{cases} 1: & \sum_{f_1}^{f_2} X(t) > \gamma_{SAT_2} \\ 0: & otherwise \end{cases} \tag{4.5}$$

SAT hypothesis can therefore be defined as:

$$H_2 = \begin{cases} 1: & H_2a \quad \vee \quad H_2b \\ 0: & otherwise \end{cases} \tag{4.6}$$

4.2.3 Power Line Interference detection

Figure 4.5 displays the FFT of excerpt from Figure 2.26. From this analysis it is possible do detect PLI from Fourier analysis, taking advantage that the local power grid operates at a frequency of $50Hz$. PLI hypothesis can therefore be defined as:

$$H_3 = \begin{cases} 1: & X(50) > \gamma_{PLI} \\ 0: & otherwise \end{cases} \tag{4.7}$$

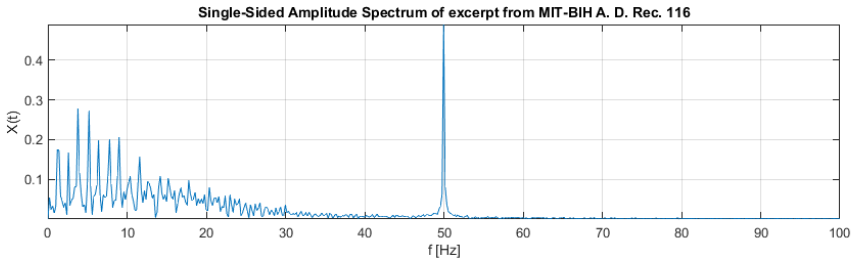

Figure 4.5: FFT of ECG signal corrupted with PLI.

4.3 Dynamic Range Optimization

A key objective of this project is to maximize the ADC dynamic range. Amplitude was adjusted to meet the criteria of 80% ADC dynamic range utilization.

4.4 Algorithm Flowchart

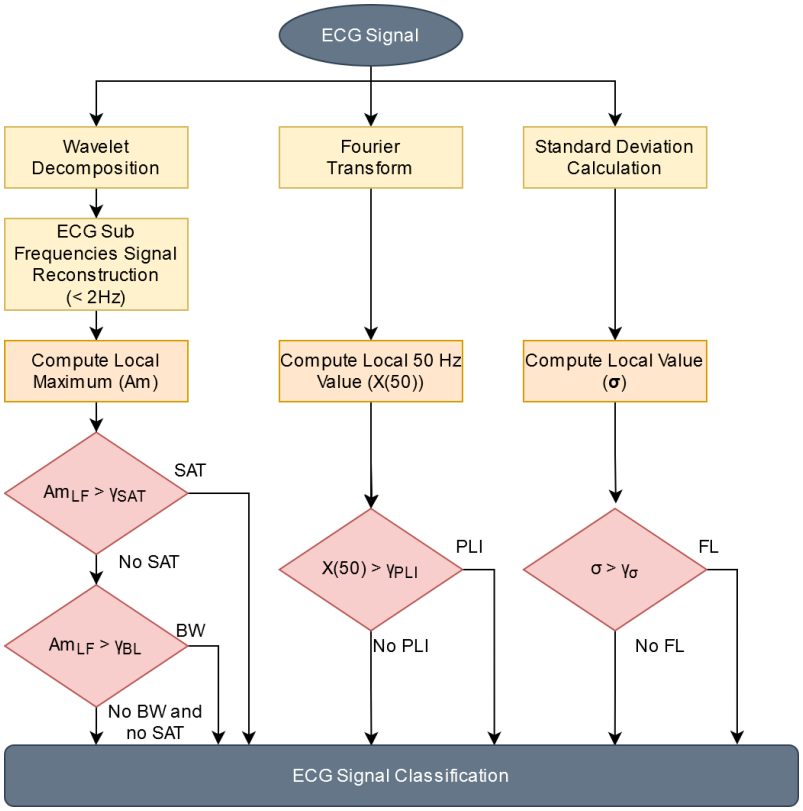

Figure 4.6: Simplified flow chart of the proposed method. Figure from [35].

The flow chart of the proposed method is illustrated in 4.6. Our proposed method works in three stages: Wavelet decomposition of ECG signal into detail and approximation sub-bands, simultaneous ECG signal and noise reconstruction and features extraction from these sub-bands for detection and classification of ECG noises.

Please note that in Figure 4.6, adapted from the article *Electrocardiographic Signal Quality Assessment Without Morphology Analysis*, the QA algorithm includes Flat Line (FL) detection, which is based on local maximum computation using standard deviation calculations. However, this analysis is not relevant to the current project and will therefore be omitted.

Chapter 5

Adaptive ECG System Design

This chapter will focus on describing the process and design decisions encompassed by the hardware development stage of this project. From the analysis performed in Section 2.3 and 2.3.4, it was concluded that the most pressing issues able to compromise signal integrity trough distortion are: SAT, BW and PLI. To fulfill the goals stated in Section 1.1, the hardware design will focus mainly on improving system resilience to these issues by taking dynamic adaptation of several key parameters of the AFE, as well as maximizing the usage of the dynamic range of the ADC.

5.1 Adaptative ECG Analog Front-End Design

(Conteúdo removido ao abrigo da alínea 3ª do Artigo 17º do Anexo do Despacho n.º 10934/2020, publicado em Diário da República Portuguesa n.º 217/2020, Série II de 6 de Novembro de 2020.)

5.1.1 Right Led Drive Design

5.1.2 Instrumentation Amplifier & High Pass Filter

(Conteúdo removido ao abrigo da alínea 3ª do Artigo 17º do Anexo do Despacho n.º 10934/2020, publicado em Diário da República Portuguesa n.º 217/2020, Série II de 6 de Novembro de 2020.)

5.1.3 Final Gain Stage and Offset Adjust

(Conteúdo removido ao abrigo da alínea 3ª do Artigo 17º do Anexo do Despacho n.º 10934/2020, publicado em Diário da República Portuguesa n.º 217/2020, Série II de 6 de Novembro de 2020.)

5.2 Micro-Controller Unit

Since firmware development is not the primary focus of this project, the goal was to implement the project using a MCU development board that, when combined with the development environment, would fulfill the project requirements and streamline the development process. After conducting initial research on available development boards and considering the project's constraints, two options were considered: the Arduino H7 Portenta and the Raspberry Pi Pico.

Table 5.1: Arduino Portenta H7 & Raspberry Pi Pico features.

	Arduino Portenta H7	**Raspberry Pi Pico**
MCU	STM32H747VI Dual core Cortex-M7+M4	RP2040 Dual core Cortex-M0+
MCU Frequency [MHz]	480(M7), 240(M4)	133MHz
Memory	8MB SDRAM + 16MB Flash	264kB SRAM + 2MB Flash
Interfaces	80 total GPIO pins 8 Analog Pins 4x UART 6x SPI 1x USB-C Full Speed (10Gbit/s)	26 total GPIO pins 3 Analog Pins 2x UART 2x I2C Controllers 1x USB 1.1 (12 Mbit/s)
ADC	3x 16-bit @ 3.6MSPS	1x 12-bit SAR @ 500kSPS
Supported Programming Languages\Environments	Arduino C C++ MicroPython	Arduino C C++ CircuitPython MicroPython
Price [€]	99	5

Despite the price difference, the development of this project initially began with the Arduino Portenta H7 due to its specifications and the author's familiarity with the Arduino IDE environment. However, the development process encountered challenges such as suboptimal interfacing with the Arduino IDE, frequent bugs, and unfinished modules. These issues caused significant delays in the development timeline as resolving unexpected problems proved time-consuming. Furthermore, the H7 Portenta suffered from poor documentation and a low adoption rate within the community, resulting in limited support. Attempts were made to switch to other supported languages such as C and C++, but the encountered support was also inadequate. Consequently, a decision was made to proceed with implementing this project using the Raspberry Pi Pico and MicroPython. This choice proved to be a better fit for the project, offering comprehensive documentation, strong community support, and a more cost-effective approach for replicating the system during various stages of development iterations.

5.2.1 Analog to Digital Conversion

For the intended application, the most critical task performed by the MCU is ADC acquisition, for which the Raspberry Pi Pico advertises a maximum ADC sampling rate of $0.5MHz$. The adaptive ECG system is intended to operate at a sampling rate $f_s = 1kHz$ sampling 2 ADC channels. The maximum allowable sampling time per channel is $t_s = 1/(2.f_s) = 500\mu s$. In order to maximize usage of the hardware resources provided by the Raspberry Pi Pico several tests were performed. Firstly, MicroPython code was developed taking advantage of the built-in ADC library, as follows:

```
from machine import Pin, ADC
import time
pin_adc = machine.ADC(28) # ADC Pin
init_time = time.ticks_us() # Time before sampling [us]
value = pin_adc.read_u16() # ADC read
end_time = time.ticks_us() # Time after sampling [us]
execution_time=end_time-init_time # Calculate ADC read time
print("Execution time: ",execution_time, "[us]") # Output value
```

This test uses the *time* module from MicroPython to measure the elapsed time during ADC sampling. The resulting output from this test was:

```
>>> %Run -c $EDITOR_CONTENT
  Execution time: 90 [us]
```

Execution of this code shows that the system is able to perform single channel ADC acquisition in approximately $90\mu s$, enabling a maximum sampling rate above $10kSPS/channel$. This suffices for the intents of this project, however, it is under-performing when compared to the maximum advertised value. Additional sampling rate could be used to perform signal over-sampling and averaging providing a multitude of benefits for DSP applications [36]. The following test was performed with Direct Memory Access (DMA) and is an adaptation of the article *Pi Pico ADC input using DMA and MicroPython* [37].

```
import time, array, uctypes, rp_devices as devs

adc = devs.ADC_DEVICE

DMA_CHAN = 0 # Define DMA channel
dma_chan = devs.DMA_CHANS[DMA_CHAN] #
dma = devs.DMA_DEVICE #
NSAMPLES = 1000 # Define number of samples
RATE = 500000 # Define sampling rate [Samples/s]

adc.FCS.EN = adc.FCS.DREQ_EN = 1 # enable the ADC FIFO
adc_buff = array.array('H', (0 for _ in range(NSAMPLES))) # Create a 16-bit
    buffer to hold the samples
adc.DIV_REG = (48000000 // RATE - 1) << 8 # Set sample rate
adc.FCS.THRESH = adc.FCS.OVER = adc.FCS.UNDER = 1

dma_chan.READ_ADDR_REG = devs.ADC_FIFO_ADDR DMA source addr
dma_chan.WRITE_ADDR_REG = uctypes.addressof(adc_buff)# DMA destination addr
dma_chan.TRANS_COUNT_REG = NSAMPLES # DMA sample count

dma_chan.CTRL_TRIG_REG = 0
dma_chan.CTRL_TRIG.CHAIN_TO = DMA_CHAN
dma_chan.CTRL_TRIG.INCR_WRITE = dma_chan.CTRL_TRIG.IRQ_QUIET = 1 # auto-increment
dma_chan.CTRL_TRIG.TREQ_SEL = devs.DR EQ_ADC
dma_chan.CTRL_TRIG.DATA_SIZE = 1
dma_chan.CTRL_TRIG.EN = 1

while adc.FCS.LEVEL: # Clear down the ADC FIFO
    x = adc.FIFO_REG # to avoid old readings

init_time = time.ticks_us() #Time before sampling [us]
adc.CS.START_MANY = 1
while dma_chan.CTRL_TRIG.BUSY:
    time.sleep_us(1)
adc.CS.START_MANY = 0
end_time = time.ticks_us() # Time after sampling [us]
execution_time=end_time-init_time # Calculate ADC read time
print("Execution time: ",execution_time, "[us]") # Output value

dma_chan.CTRL_TRIG.EN = 0
```

Similarly to the first test, this test utilizes the *time* module from MicroPython to measure the elapsed time during ADC sampling. The resulting output from this test was:

```
>>> %Run -c $EDITOR_CONTENT
   Execution time: 4034 [us]
```

Execution time was $4ms$ for 1000 samples, thus showing that the system is able to perform single channel ADC acquisition in approximately $4\mu s$, enabling a maximum sampling rate approaching $250kSPS$.

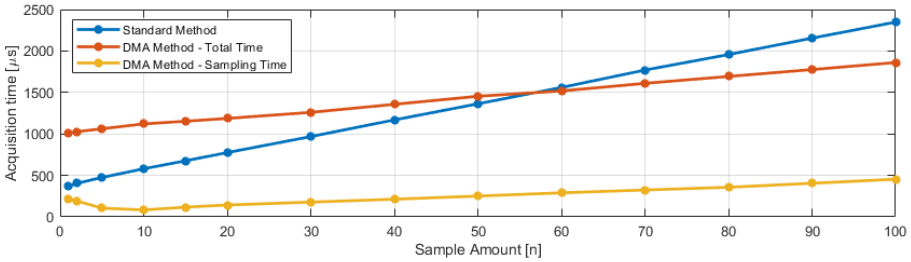

Figure 5.1: Raspberry Pi Pico analog read performance benchmark - Sampling time.

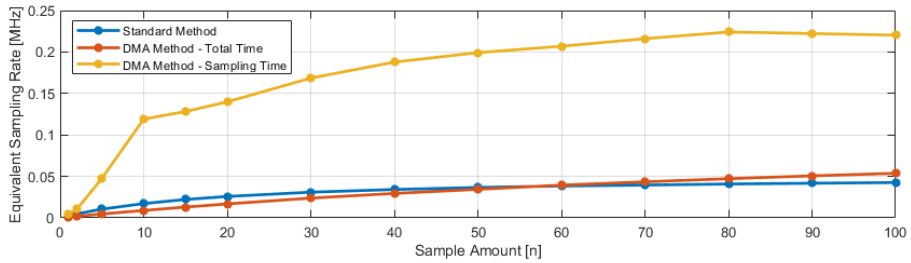

Figure 5.2: Raspberry Pi Pico analog read performance benchmark - Sampling rate.

Both tests were conducted for a multitude of sample amounts, and Figures 5.1 and 5.2 display the results of the performance benchmarks. It is visible that the DMA method provides absolute highest sampling rate; however, due to a 1 millisecond time penalty for DMA set-up, this method makes it unfeasible for this application. The time penalty concerning the DMA method is most likely related to the configuration of ADC into *free-running mode*, which allows for maximum sampling rate for a single ADC channel [37]. However, for this project, acquisition of multiple ADC channels is desired, and compounding set-up times results in a significant decrease in effective sampling rate. Tanking into consideration these results, only the standard method meets the performance requirements for this application.

5.2.2 SPI Communication

(Conteúdo removido ao abrigo da alínea 3ª do Artigo 17º do Anexo do Despacho n.º 10934/2020, publicado em Diário da República Portuguesa n.º 217/2020, Série II de 6 de Novembro de 2020.)

5.2.3 UART & USB Communication Protocol

The Raspberry Pi Pico posses one dedicated USB port; however, by using MicroPython to program the MCU, configuration of this port is limited. Therefore, it was decided to allocate the Pi Pico USB port for firmware uploading and debugging only and utilize one of the Universal Asynchronous Receiver-Transmitter (UART) controllers to interface with the PC. This necessitates a UART to USB interface.

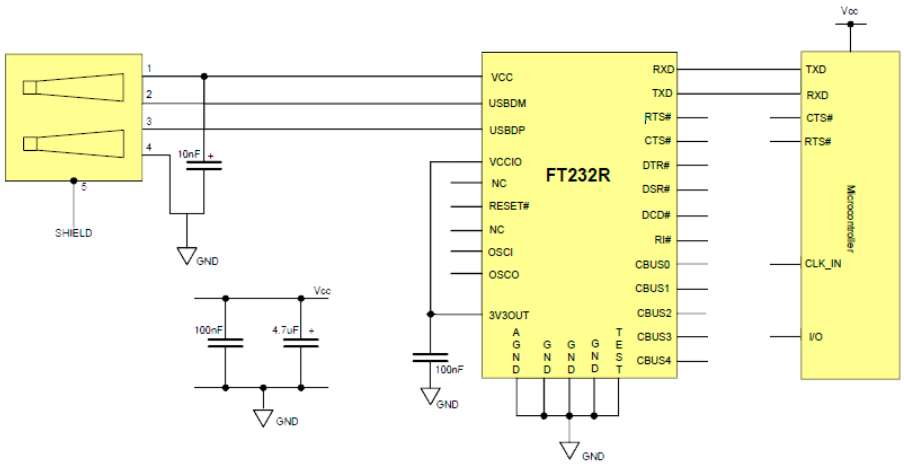

Figure 5.3: FTDI FT232R - USB to MCU UART Interface. Adapted from [38].

For this application, the chosen part was the FTDI FT232R, which is a single-chip USB to asynchronous serial data transfer interface. In this project, it will be used as a RS232 to USB converter. Circuit implementation will follow the *USB to MCU UART Interface* recommended layout by the manufacturer in the device data sheet [38], presented in Figure 5.3.

Table 5.2: Data UART frame.

Field name	Start bit	START	N	ADC1	ADC2	STOP	CR	PB	Stop bit
Size [Bit]	1	8	8	16	16	8	8	1	1

$$R_{b_{min}} = \frac{67[bit/frame].1000[frame/s]}{1[s]} = 67[kbit/s] \tag{5.1}$$

$$BaudRate_{min} = \frac{R_{b_{min}}}{\#bits/baud} = 67000[baud] \tag{5.2}$$

Table 5.3: Control UART frame.

Field name	START	-	-	-	-	-	-	STOP	CR	PB	Stop bit
Size [Bit]	1	8	8	8	8	8	8	8	8	1	1

Presented in equations 5.1 and 5.2 are the minimum bit rate and baud rate, respectively, required to ensure the data transfer necessary to support the determined sampling rate and number of ADC channels, standard control fields of the RS232 data frame along with additional application-specific control fields.

Following the analysis presented in the following section, USB speed the was set at 115200*baud*, in order to guarantee appropriate timing for other tasks running on the same MCU thread, as further detailed in the next section.

5.2.4 Dual Core Multi-Threaded Operation & Timing

The Raspberry Pi Pico possesses 2 processor cores. To take full advantage of the available processing capacity, it was decided to implement a multi-threaded workflow, the flowchart of which is presented in Figure 5.4.

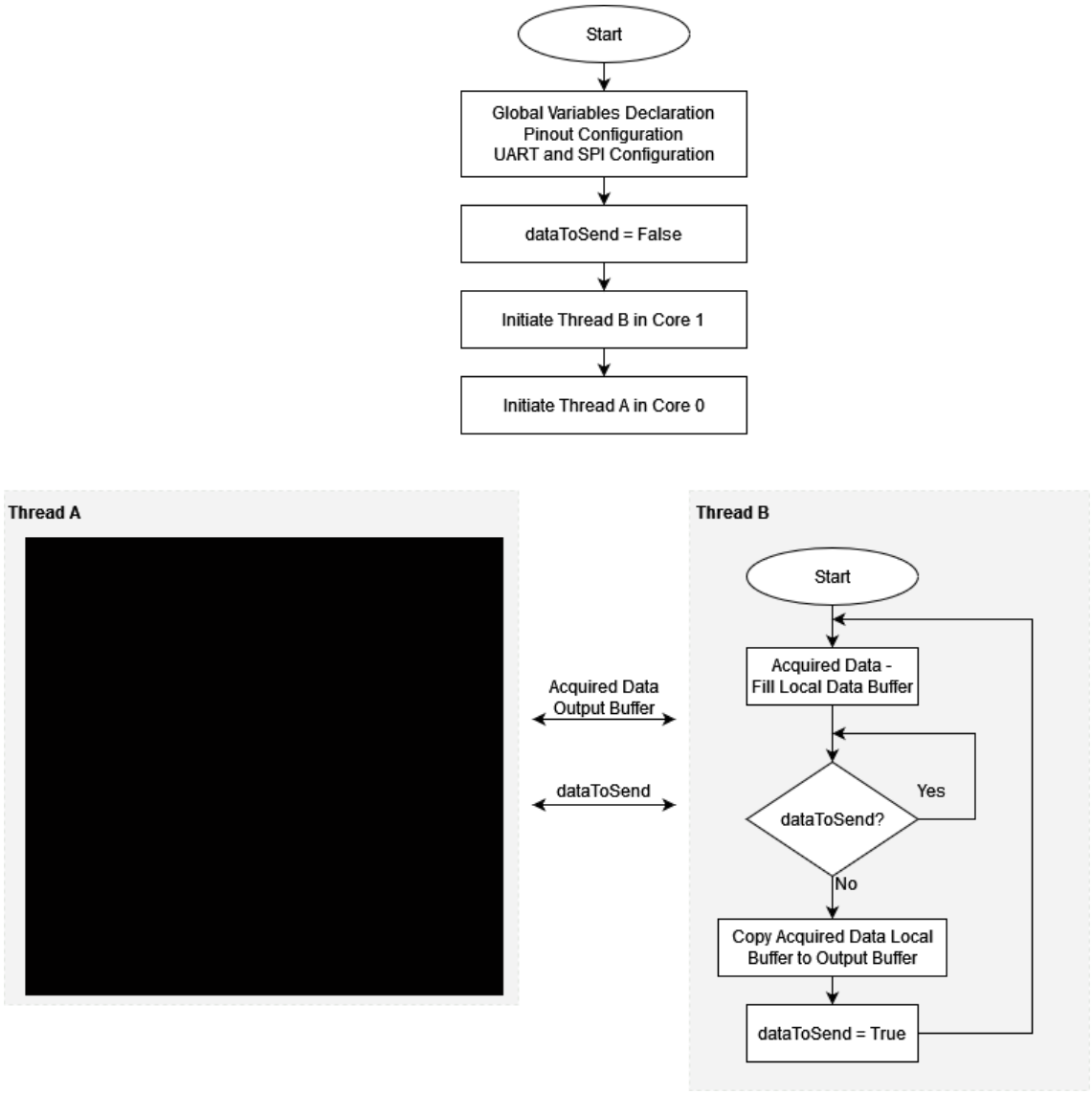

Figure 5.4: CPU Flowchart.

(Conteúdo removido ao abrigo da alínea 3ª do Artigo 17º do Anexo do Despacho n.º 10934/2020, publicado em Diário da República Portuguesa n.º 217/2020, Série II de 6 de Novembro de 2020.)

Thread A executed, by MCU processor core 0, is responsible for handling UART communication with the PC and Serial Peripheral Interface (SPI) communication. Thread B, executed by core 1, is responsible the timing and acquisition of the required analog channels. To ensure data integrity, the proposed data flow uses a double-buffering technique. Thread B has a local data buffer that is filled at the required sampling rate. When this buffer is full, the data copied to the output buffer and shared with Thread A to be sent to the PC. The data buffers size are calculated as a function of the sampling rate and data display refresh rate. The proposed data flow is agnostic to the data buffer size.

For this operation to succeed, timing is of the utmost importance. UART and SPI data rates where chosen in such a way that all communication can be performed during acquisition time. However, the *dataToSend* control flag was implemented as a safeguard to ensure data protection. The program is implemented in such a way that this condition is not activated in normal operation.

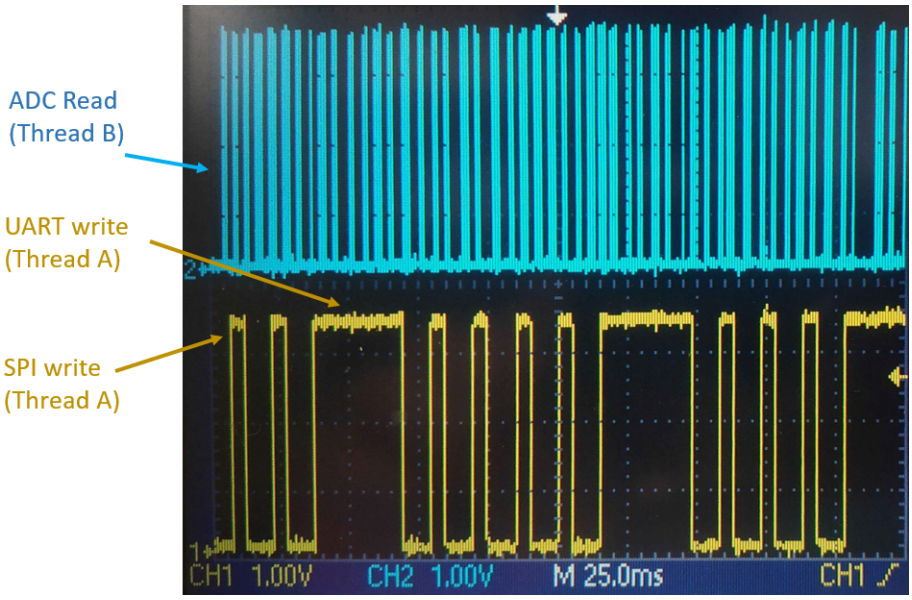

Figure 5.5: Multi-threaded operation. Timescale $25ms$.

Figure 5.5 displays the result of this multi-threaded operation. Two General Purpose Input/Output (GPIO) pins were temporarily allocated for this purpose. One was programmed to be active when communication was being performed (UART or SPI), displayed in channel 1 on the oscilloscope, and the other was programmed to be active when the ADC acquisition is being performed, displayed in channel 2 on the oscilloscope. As observed, there is concurrent operation on each of the available Central Processing Unit (CPU) cores. UART write takes approximately 30ms, performed every 100ms. SPI write takes approximately 5ms. ADC sampling is performed at $1kHz$. Some visual aliasing is present in channel 2. Furthered detailed in Figure 5.6.

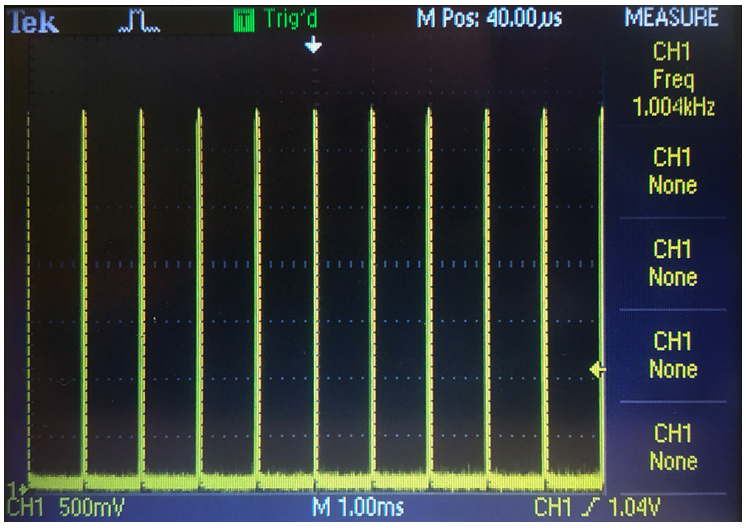

Figure 5.6: Sampling rate $f_s = 1kHz$. Timescale $1ms$

In Figure 5.6, similarly to Figure 5.5, an GPIO pin was allocated and programmed to be driven to a high logic level whilst ADC acquisition is being performed, the output of this pin displayed in the oscilloscope. As observed there is a periodic timing of $T_s = 1ms$ in between acquisitions, coherent with a sampling rate $f_s = 1kHz$, with $f_s = 1/T_s$.

5.3 Power Supply

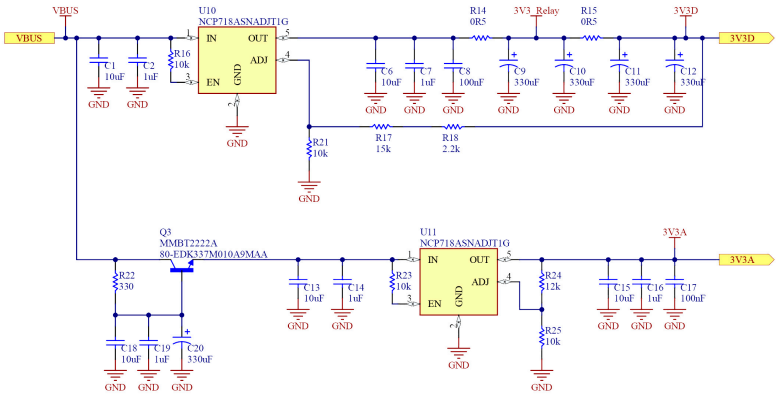

Figure 5.7: Detail of circuit schematic - Power Supply

Power conditioning to the system is provided by the USB connector to the PC. Individual power supply rails were design for both analog and digital portions of the system. Voltage regulations is provided by a linear voltage regulator with voltage sense feedback. The voltage regulator designated for the analog portion of the circuit is preceded by a capacitance multiplier in order to provided additional resilience from any digital noise interference originated in the USB communication or MCU. Figure 5.8 displays the power section transfer function.

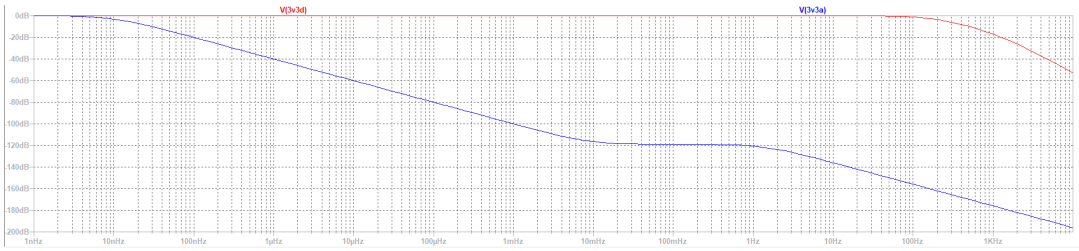

Figure 5.8: Power conditioning stage frequency response.

5.4 Printed Circuit Board Design

After the development process, the complete circuit was implemented using Altium Designer PCB Design software. At an early stage of project development, an initial PCB design was made, displayed in Figure 5.9. This design preceded MCU selection, the relevant inputs and outputs were made available via header connectors in order to remain versatile to MCU selection.

Once a decision was made in favor of the Raspberry Pi Pico, the following design iteration was produced. This version encompassed a socket for the chosen MCU, power section improvements, and UART to USB conversion. The design philosophy had limited concern with hardware miniaturization. A standard size of 100x100mm for the PCB outline was chosen, with ample area for integrated circuits in though-hole Dual In-line Packages (DIP) to provide ease of assembly and rework flexibility.

Figure 5.10 displays the overall design of the final iteration of the PCB design whilst 5.11 further details the design with respect to the layout of the relevant functional blocks that comprise overall operation.

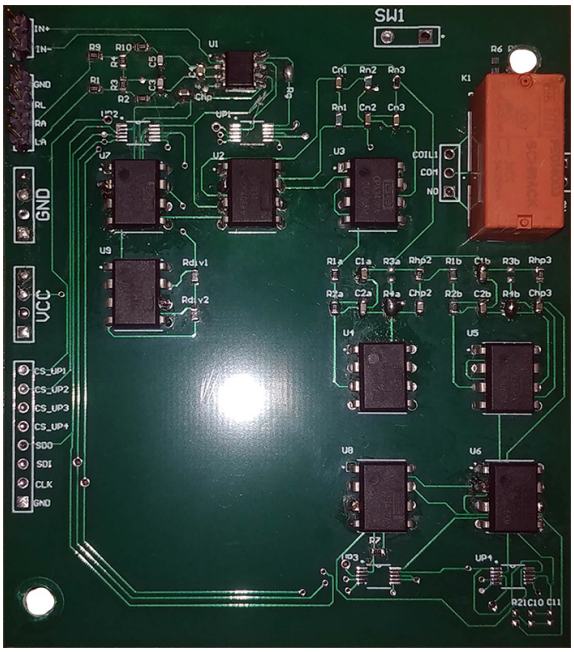

Figure 5.9: First PCB Design.

Several headers connections were implemented in the PCB design in order to allow connections for debugging, expansion and rework. A multitude of test-points were created for circuit testing, ranging from power rails to the AFE stages. These are described in Appendix D.1 and refer to Appendix D.2 which contains the full schematic.

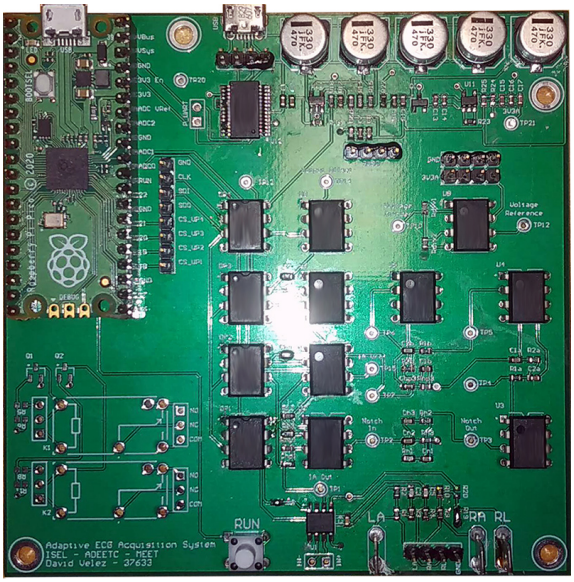

Figure 5.10: Second PCB Design for Raspberry Pi Pico.

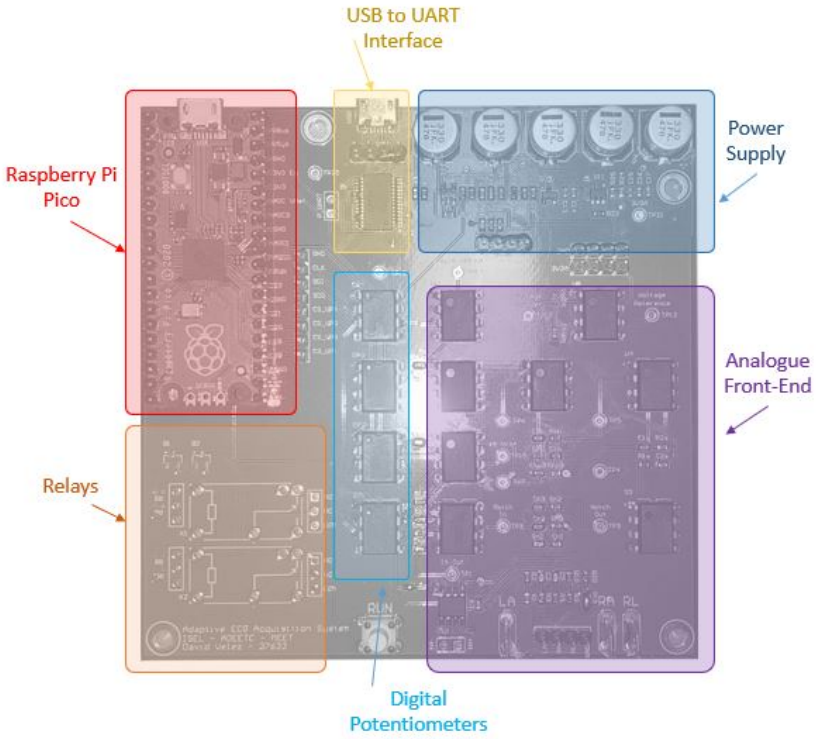

Figure 5.11: Second PCB Design - Detailed Layout

Chapter 6

Graphical User Interface & Adaptive Parameter Control

Taking in to account the groundwork laid in Chapter 4 on the QA algorithm, an application was developed in MATLAB *App Designer*. This application will function as a graphical interface for the user of the system by displaying the acquired data from the hardware, showing the relevant parameters for QA as well as offer manual or automatic optimization of the key AFE parameters. It communicates with the hardware as described in Section 5.2.3.

(Conteúdo removido ao abrigo da alínea 3ª do Artigo 17º do Anexo do Despacho n.º 10934/2020, publicado em Diário da República Portuguesa n.º 217/2020, Série II de 6 de Novembro de 2020.)

6.1 Data Logging Protocol

The developed GUI also performs recording of the ECG acquisition for future analysis, thus a specific data protocol was defined. Data is to be logged in a *.txt* file, in the PC's secondary storage, time-stamped with the start time of the recording as file name.

(Conteúdo removido ao abrigo da alínea 3ª do Artigo 17º do Anexo do Despacho n.º 10934/2020, publicado em Diário da República Portuguesa n.º 217/2020, Série II de 6 de Novembro de 2020.)

6.2 Parameter Adaptation Strategy

(Conteúdo removido ao abrigo da alínea 3ª do Artigo 17º do Anexo do Despacho n.º 10934/2020, publicado em Diário da República Portuguesa n.º 217/2020, Série II de 6 de Novembro de 2020.)

Chapter 7

Results & Discussion

In this chapter, the results of several tests performed on the system are described and presented with the aim of meeting the goals defined in Section 3.6. Primary data recordings will refer to the anonymized and individual test subject #. A full list of test subjects is provided in Appendix C with additional information on biological sex, weight, age, height and preexisting heart conditions.

7.1 Quality Assessment Algorithm Results

This section aims to validate the QA algorithm on the commonly used CinC11 Dataset [28]. The determination of the thresholds used for each of the decisions rules is at the present time calculated using a training dataset, as values for γ_{BW}, γ_{SAT} and γ_{σ} depend on AFE characteristics such as dynamic range and gain. For each decision rule, the recordings were split into acceptable or unacceptable for interpretation, as determined per the PhysioNet reference classifications based on the current available information.

7.1.1 Baseline Wander Detection in CinC11

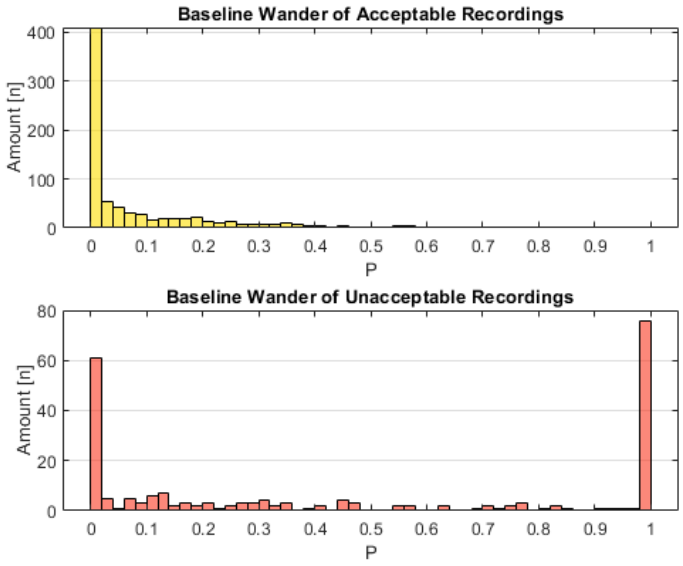

Figure 7.1: BW Analysis on CinC11 recordings.

In Figure 7.1, it is visible that 33.7% of unacceptable recordings present BW throughout the recording, whereas the acceptable recordings present low amounts of BW.

7.1.2 Saturation Detection in CinC11

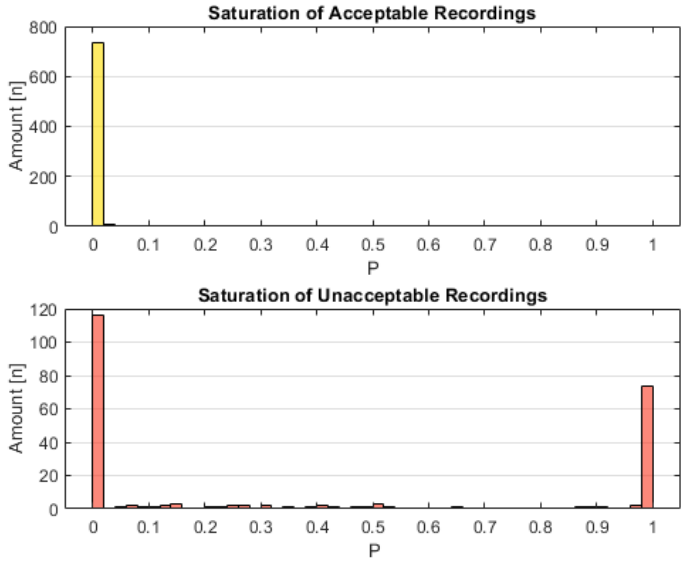

Figure 7.2: SAT Analysis on CinC11 recordings.

In Figure 7.2 is is visible that 32.8% of unacceptable recordings present SAT throughout the recording, whereas the acceptable recordings present low amounts of SAT.

7.1.3 Standard Deviation Calculation - CinC11

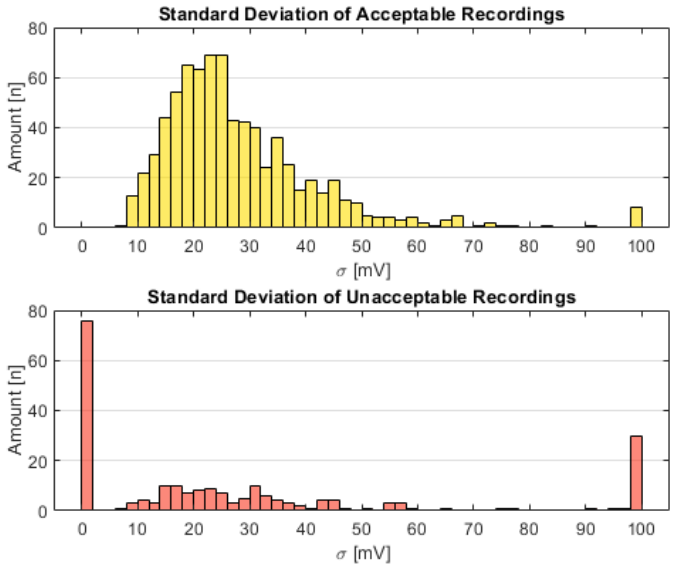

Figure 7.3: Standard Deviation Calculation Analysis on CinC11 recordings.

In Figure 7.3, it is visible that acceptable recordings present a standard deviation between 5 and $95mV$, which represents 99% of cases. This figure is contrasted by the unacceptable recordings, where 47.1% of recordings present either minimum (flat-line) of excessive amounts of standard deviations.

7.1.4 Quality Assessment of CinC11 Results

Table 7.1 presents the overall results from the CinC11 dataset as a confusion matrix. These results were obtained using a disjunction logical operation, that is, if one of the interferences was triggered the record was considered unacceptable.

Table 7.1: ECG quality assessment results confusion matrix.

		Predicted	
		Acceptable	Unacceptable
Actual	Acceptable	755 97.4%	20 2.6%
	Unacceptable	109 48.4%	116 51.6%

It was observed that the developed algorithm shows promising results given that the algorithm does not use the ECG signal directly, but rather relies on the noise and decomposition of the ECG signal into components related with the artifacts. The results present a very high success rate (over 97%) of acceptable recording prediction once values for γ_{BW}, γ_{SAT} and γ_{σ} are optimized for the present dataset.

7.2 Adaptive AFE Functionality Tests

This section presents a range of tests to validate basic functionality and control of the adaptive characteristics of the AFE.

(Conteúdo removido ao abrigo da alínea 3ª do Artigo 17º do Anexo do Despacho n.º 10934/2020, publicado em Diário da República Portuguesa n.º 217/2020, Série II de 6 de Novembro de 2020.)

7.3 Adaptive Tests Under Resting Condition

These tests were design to satisfy parameters #2 and #3 of the performance metrics defined in section 3.6. The tests were performed with the device connected to a human test subject in resting condition, using diverse test subjects and electrode types in Lead-I configuration as shown in Figure 2.12. When applicable, RE was placed in the abdomen on the right iliac region. The device was connected via USB to a laptop PC disconnected from mains power and ground, thus simulating a portable, battery-powered wearable device. Subjects are anonymized and will be identified solely by their respective subject number. Subject data is provided in table C.1 in appendix. Note that performance metrics and characteristics obtained assume ideal filter behavior.

7.3.1 Gel Electrolyte Electrodes

This section details test results performed with gel coated electrodes. Although the majority of test subjects in Appendix C were tested under these conditions, only a portion will be detailed, either as standard recordings or as outlier signals of particular interest.

Test subject #1:

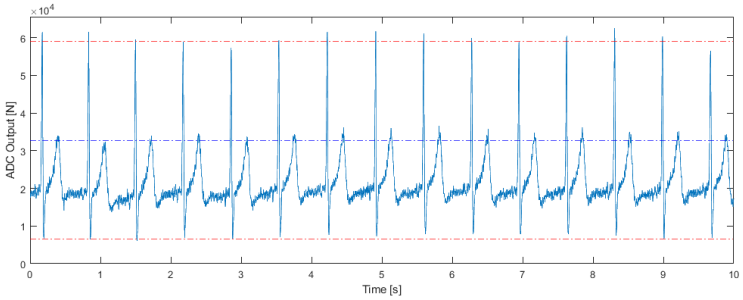

Figure 7.4: Test subject #1 results - Gel electrolyte electrodes with RE .

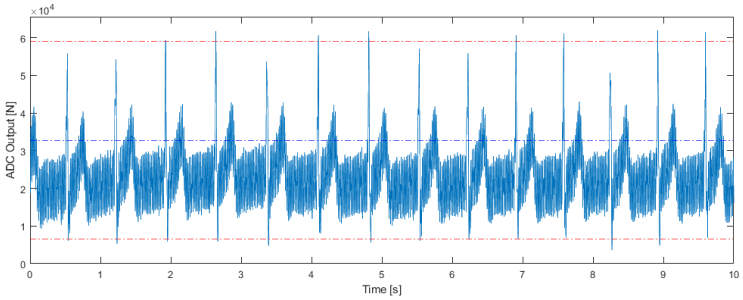

Figure 7.5: Test subject #1 results - Gel electrolyte electrodes without RE.

Results for this test subject are as expected. Acquired ECG signal morphology is clearly defined and ADC dynamic range is optimized as detailed in Figure 7.4 and 7.5. Table 7.2 summarizes the AFE parameters obtained.

Table 7.2: Test subject #1 results.

Parameter	**Value**	**Unit**
f_{hp}	0.39	Hz
IA Gain	65	V/V
FS Gain	4.7	V/V
Total AFE Gain	3036	V/V
Estimated ECG Signal Amplitude	604	μV
Notch Filter	Off	Status

Test subject #4:

Test subject #4 presents a preexisting medically diagnosed condition. The ECG signal of this test subject presents a R-peak significantly higher than the S-peak, displayed in Figures 7.6 and 7.7.

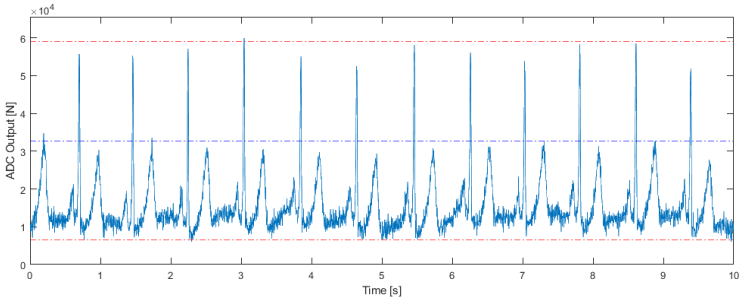

Figure 7.6: Test subject #4 results - Gel electrolyte electrodes with RE .

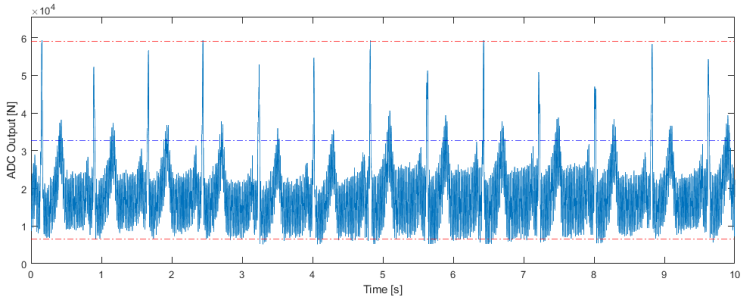

Figure 7.7: Test subject #4 results - Gel electrolyte electrodes without RE.

The adaptive AFE has performed a significant voltage offset of the signal baseline from the ADC half-range values that, in conjunction with appropriate gain, performs ADC dynamic range optimization. Table 7.3 summarizes the AFE parameters obtained.

Table 7.3: Test subject #4 results.

Parameter	**Value**	**Unit**
f_{hp}	0.35	Hz
IA Gain	55	V/V
FS Gain	6.1	V/V
Total AFE Gain	3376	V/V
Estimated ECG Signal Amplitude	543	μV
Notch Filter	Off	Status

Test subject #5:

This test subject presented the additional challenge of being the youngest test subject, a female with the smallest height and lightest weight. These conditions are associated with decreased ECG amplitude [39]. Results were obtained with reference electrode.

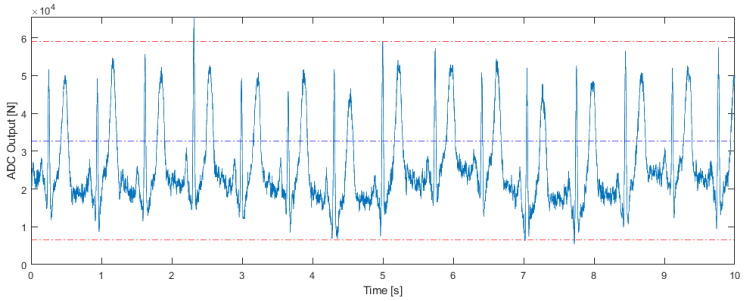

Figure 7.8: Test subject #5 results - Gel electrolyte electrodes.

Table 7.4: Test subject #5 results.

Parameter	**Value**	**Unit**
f_{hp}	0.08	Hz
IA Gain	501	V/V
FS Gain	2.8	V/V
Total AFE Gain	13908	V/V
Estimated ECG Signal Amplitude	190	μV
Notch Filter	Off	Status

Presented in Figure 7.8 is an excerpt from test subject #5 results, with the relevant AFE parameters detailed in Table 7.4. As expected the input signal was of a very small amplitude, however the AFE possesses sufficient gain adaptability to maximize the ADC dynamic range as intended, providing clearly defined signal morphology.

Regarding ADC dynamic range utilization of the adaptive AFE in comparison to a static configuration system such as BITalino, of which relevant AFE specifications are defined Table 3.1, it would be expected for this specific test subject to obtain a mere 6.4% of the BITalino's ADC dynamic range, comparatively to the 80% of the adaptive AFE which is able to provide a 12.6 fold increase in gain to satisfy the desired optimization conditions.

Test subject #11:

This test subject presented arrhythmia during ECG recording, observable by the uneven R-R interval displayed in Figure 7.9; there is regular medical follow-up regarding this issue, although it wasn't possible to obtain the exact cause of the arrhythmia as a matter of record.

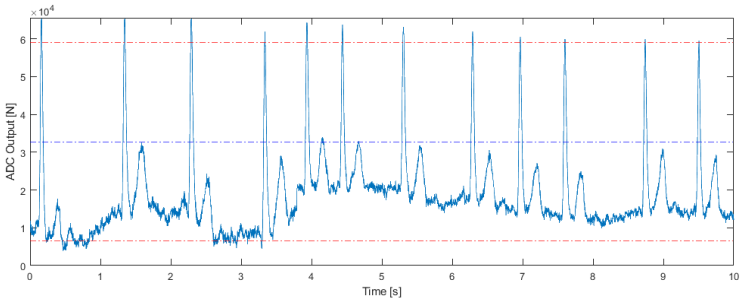

Figure 7.9: Test subject #11 results - Gel electrolyte electrodes.

Table 7.5: Test subject #11 results.

Parameter	Value	Unit
f_{hp}	0.07	Hz
IA Gain	212	V/V
FS Gain	1.36	V/V
Total AFE Gain	2895	V/V
Estimated ECG Signal Amplitude	912	μV
Notch Filter	Off	Status

Signal morphology is clearly defined. In conjunction with a medical validated fibrillation and arrhythmia detection algorithm, the developed solution could conceivably be used as the acquisition source, constantly adapting it's settings to provide the best possible chance at documenting abnormal heart rhythms. Otherwise, the parameters regarding signal conditioning are as expected, detailed in Table 7.5. Recording was performed with reference electrode.

7.3.2 Dry electrodes

This section details the test results obtained with the following dry electrode types:

- metal electrodes,
- conductive polymer electrodes,
- conductive plastic electrodes,

- conductive leather electrodes.

7.3.3 Metal Electrodes

Figure 7.10: Metal Electrodes.

The chosen metal electrode is comprised a SAE 304 stainless steel plate, displayed in Figure 7.10.

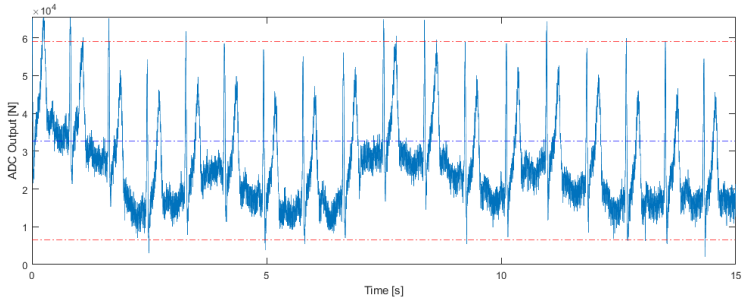

Figure 7.11: ECG signal acquired with conductive metal electrodes - test subject #1.

Table 7.6: Metal electrodes test results - test subject #1.

Parameter	Value	Unit
f_{hp}	2.38	Hz
IA Gain	91.78	V/V
FS Gain	5.22	V/V
Total AFE Gain	4790	V/V
Estimated ECG Signal Amplitude	560	μV

Figure 7.11 displays the results of ECG acquisition with the metal electrodes. ECG signal recording is possible; however, these electrodes present a significant amount of BW noise linked to motion artifacts, mainly due to test subject breathing. AFE parameters for ADC optimization are detailed in Table 7.6.

7.3.4 Conductive Silicone Electrodes

The chosen silicone polymer electrodes were manufacture from Primasil PR610 Series conductive silicone compound . In order to achieve electrical conductive properties with silicone rubber compound, the item is doped with carbon black. Claimed volumetric

resistivity is $< 5[\Omega.cm]$, measured as per *Standard Test Method for Rubber Property—Volume Resistivity Of Electrically Conductive and Antistatic Products* ASTM D991 – 89 standard [40]. The electrode is displayed in Figure 7.12

Figure 7.12: Silicone Electrodes.

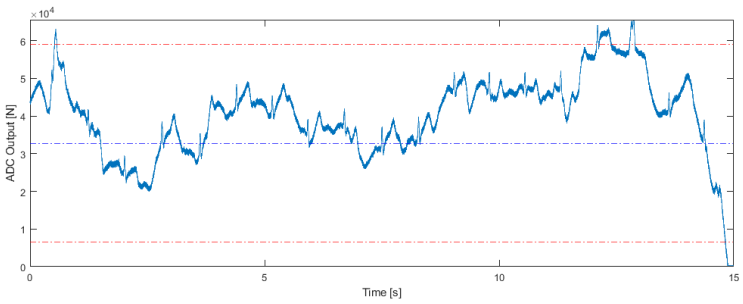

Figure 7.13: ECG signal acquired with conductive silicone electrodes - test subject #1.

Table 7.7: Conductive silicone electrodes test results - test subject #1.

Parameter	Value	Unit
f_{hp}	5.46	Hz
IA Gain	10.8	V/V
FS Gain	5.46	V/V
Total AFE Gain	549	V/V

Figure 7.13 displays the results of ECG acquisition with the silicone electrodes. ECG signal recording is possible. It was observed that these electrodes present a very high amount of BW noise linked to motion artifacts resulting in unstable signal acquisition. Most likely test subject induced motion artifacts have a compounding effect with silicone elasticity due to the low durometer rubber and silicone-to-stainless steel dry interface inconsistencies. AFE parameters for ADC optimization are detailed in Table 7.7. Estimated ECG signal amplitude is presented as signal was properly maximized.

7.3.5 Conductive Plastic Electrodes

To test the adaptive AFE with conductive plastics, Protopasta CDP1xxxx Series 3D printer PLA (Polylactic acid) filament was chosen. Similarly to the conductive silicone electrodes, this filament carbon black doped to achieve the desired electric proprieties. The claimed volumetric resistivity is $15[\Omega.cm]$ (isotropic model) [41]. Figure 7.14 displays

the overall appearance of the conductive PLA electrode, and its mechanical dimensions are identical to the conductive silicone electrodes.

Figure 7.14: PLA 3D printed plastic electrodes.

PLA is a thermoplastic polyester lactic acid monomer. PLA is most commonly derived from renewable, organic sources such as corn starch or sugar cane.

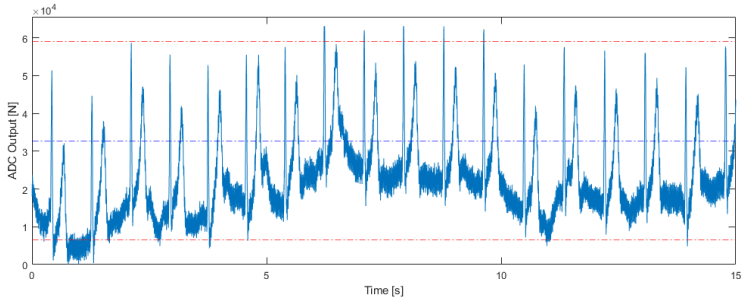

Figure 7.15: ECG signal acquired with conductive plastic electrodes - test subject #1.

Table 7.8: Conductive plastic electrodes test results - test subject #1.

Parameter	**Value**	**Unit**
f_{hp}	2.89	Hz
IA Gain	38	V/V
FS Gain	8.28	V/V
Total AFE Gain	3110	V/V
Estimated ECG Signal Amplitude	849	μV
Notch Filter	On	Status

Figure 7.16: Seat cover with applied conductive plastic electrodes.

To further test the developed system under unique scenarios, the PLA electrodes were affixed to an experimental seat cover designed to acquire ECG signals from the subject's posterior thigh during a resting state. This was done to explore the possibility of ECG signal acquisition in unconventional settings.

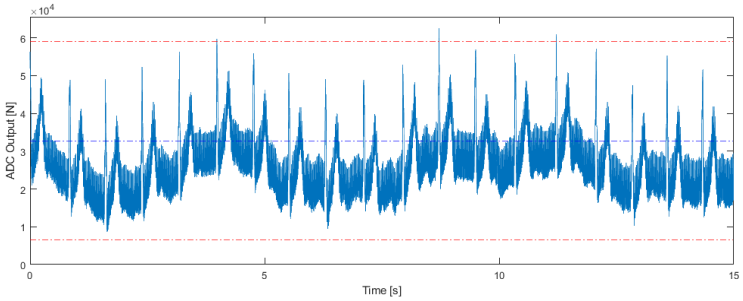

Figure 7.17: ECG signal acquired with conductive plastic electrodes coupled to the posterior thigh - test subject #1.

Table 7.9: Conductive plastic electrodes coupled to the posterior thigh test results - test subject #1.

Parameter	**Value**	**Unit**
f_{hp}	0.88	Hz
IA Gain	316	V/V
FS Gain	11	V/V
Total AFE Gain	34353	V/V
Estimated ECG Signal Amplitude	86	μV
Notch Filter	On	Status

The results are presented in Figure 7.17. Please note that due to the small level of ECG signal present, the device reached the maximum gain possible with the current configuration. This large amount of overall gain also affects the PLI noise present in the recording, resulting in a signal-to-noise ratio degradation. However, the ECG signal is present and it's characteristic morphology is clearly defined. It was observed that for test

subject #1, the amplitude of the ECG signal acquired in the subject's posterior thigh presents an approximate 10-fold reduction in amplitude.

7.3.6 Conductive Textile Electrodes

To test the system with conductive textiles, a CardioID Sensitee shirt was used, detailed in Figure 7.18. The Sensitee shirt was developed with the aim of providing a system for continuous ECG monitoring for lone-workers in scenarios of increased health and safety risk. This shirt provides two electrically conductive textile electrodes located on the test subject's torso bellow both axillary regions, thus proving electrode placement coherent with Lead-I acquisition.

(a) Sensitee shirt. (b) Sensitee shirt detail - textile electrode.

Figure 7.18: CardioID Sensitee.

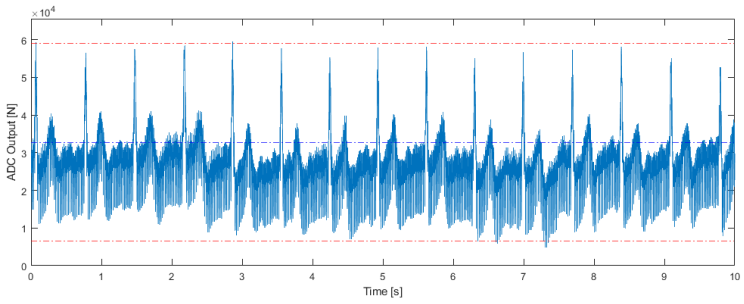

Figure 7.19: ECG signal acquired with conductive textile electrodes - test subject #1.

Table 7.10: Conductive textile test results - test subject #1.

Parameter	Value	Unit
f_{hp}	1.97	Hz
IA Gain	17.24	V/V
FS Gain	10.27	V/V
Total AFE Gain	1752	V/V
Estimated ECG Signal Amplitude	1507	μV
Notch Filter	On	Status

7.3.7 Conductive Leather

In order to test the ability of the system to perform with conductive leather electrodes, the device was connected to a steering wheel upholstered with conductive leather. This

type of acquisition set-up does not allow for RE. The conductive leather steering wheel is comprised of two zones upholstered with conductive leather separated by standard non-conductive leather, providing two electrodes for ECG acquisition. Galvanic connection to the conductive lather is performed by a ring terminal "pop" rivet to each zone, providing a mechanical secure connection. A ring terminal is connected to the device via standard copper conductors, as shown in Figure 7.20.

Figure 7.20: Conductive leather steering wheel connected to the adaptive AFE.

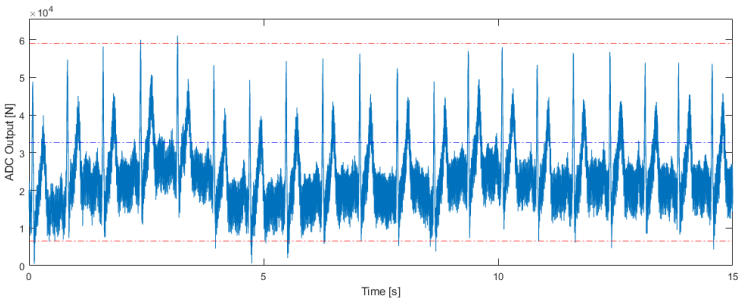

Figure 7.21: ECG signal acquired with conductive leather electrodes - test subject #1.

The system is able to perform; however, it is noticeable that this type of electrode is more susceptible to power line interference when compared with gel electrodes.

Table 7.11: Conductive leather test results - test subject #1.

Parameter	**Value**	**Unit**
f_{hp}	2.89	Hz
IA Gain	25.5	V/V
FS Gain	11	V/V
Total AFE Gain	2789	V/V
Estimated ECG Signal Amplitude	947	μV
Notch Filter	On	Status

7.4 Adaptive Tests Under Dynamic Conditions

This section details results of ECG recording with the developed system using dry electrodes, without a dedicated electrolyte medium besides sweat residues present in the skin. The results presented in this section were obtain in Lead-I configuration without REs.

7.4.1 Walking / Running

To test the system under dynamic conditions, the Sensitee shirt from Section 7.3.6 was used. Recordings were performed while running, as shown in Figure 7.22.

Figure 7.22: Running acquisition.

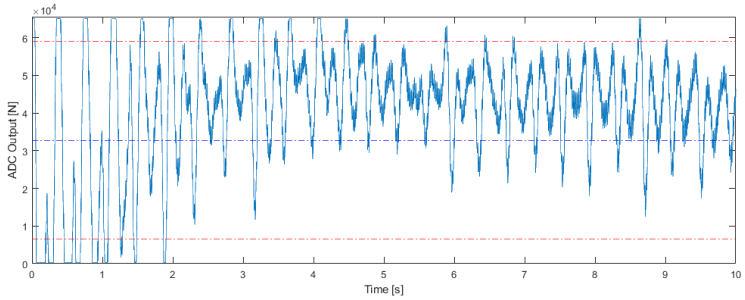

Figure 7.23: ECG signal acquired with conductive textile electrodes - test subject #1.

Figure 7.23 displays the results of this acquisition. No meaningful ECG signal was obtain from this recording due to the high amount of EMA.

7.4.2 Vehicle Simulator Acquisition

Figure 7.24: Vehicle simulator setup during acquisition.

Figure 7.24 displays the simulator setup while ECG recording is in progress. It is possible to observe the developed hardware affixed to the center simulator steering wheel to which the conductive leather cover described in Section 7.3.7 was applied. A single carriageway road with one traffic lane for each direction was chosen as the simulation scenario. Subjects were asked to perform acquisition of 10 to 15-minute period during which ECG was recorded with the developed GUI described in Chapter 6.

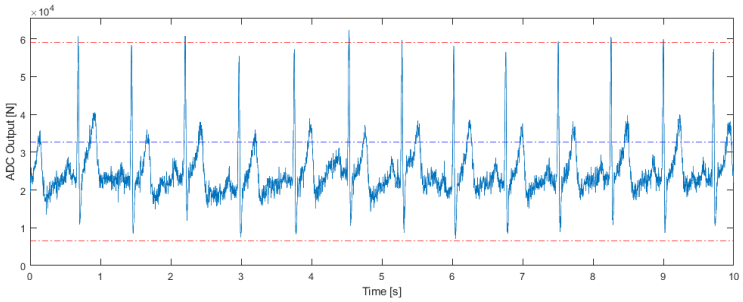

Figure 7.25: Results in vehicle simulator for test subject #1.

Figure 7.25 displays the results of vehicle simulator for test subject #1.

Table 7.12: Vehicle simulator acquisition results - test subject #1.

Parameter	**Value**	**Unit**
f_{hp}	0.49	Hz
IA Gain	95	V/V
FS Gain	1.54	V/V
Total AFE Gain	1463	V/V
Estimated ECG Signal Amplitude	1806	μV
Notch Filter	On	Status

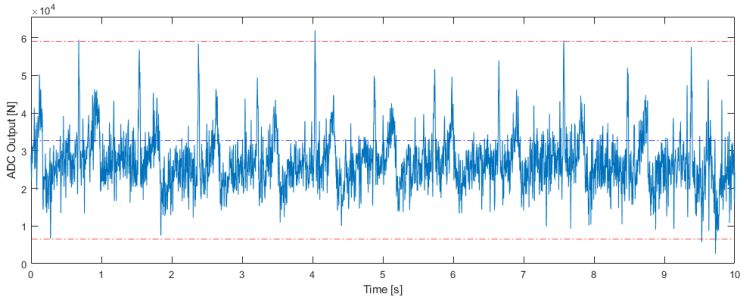

Figure 7.26: Results in vehicle simulator for test subject #12.

Figure 7.26 displays the results of vehicle simulator for test subject #12.

Table 7.13: Vehicle simulator acquisition results - test subject #12.

Parameter	**Value**	**Unit**
f_{hp}	0.93	Hz
IA Gain	32	V/V
FS Gain	7	V/V
Total AFE Gain	2261	V/V
Estimated ECG Signal Amplitude	1167	μV
Notch Filter	On	Status

It was observed that, although test subjects #1 and #12 possess comparable age and physical build, the recorded ECG signal presents different characteristics under identical acquisition conditions, with test subject #12's recording requiring significantly greater gain, more restrictive band-pass filtering, and a greater amount of PLI present. These results reinforce the value of user and context-specific AFE settings.

7.4.3 In-Car Acquisition

The drive test path, displayed in Figure 7.27, followed Portuguese route A1 (European route E1) from kilometer marker 0 to kilometer marker 13, providing a minimum of 7 minutes of acquisition time. This path was chosen for its proximity to ISEL and it's straightness, which allows test subjects to maintain a constant vehicle speed and remain with both hands in contact with the conductive leather steering wheel cover.

For this test the developed system was compared to the CardioID CardioWheel device, described in Section 3.1.3, in order to obtain a reference benchmark result as this device was specifically developed as a solution for ECG acquisition in automotive applications. The drive test path was driven in both directions for each device.

Figure 7.28 displayed the hardware set-up during the drive tests. Notice the adaptive AFE system and CardioWheel device temporarily attached to the center of the steering wheel. The steering wheel cover from Section 7.3.7 was applied to a vehicle's steering wheel, thus implementing the required conductive electrodes for ECG signal acquisition. Connection to the relevant device was performed during acquisition period.

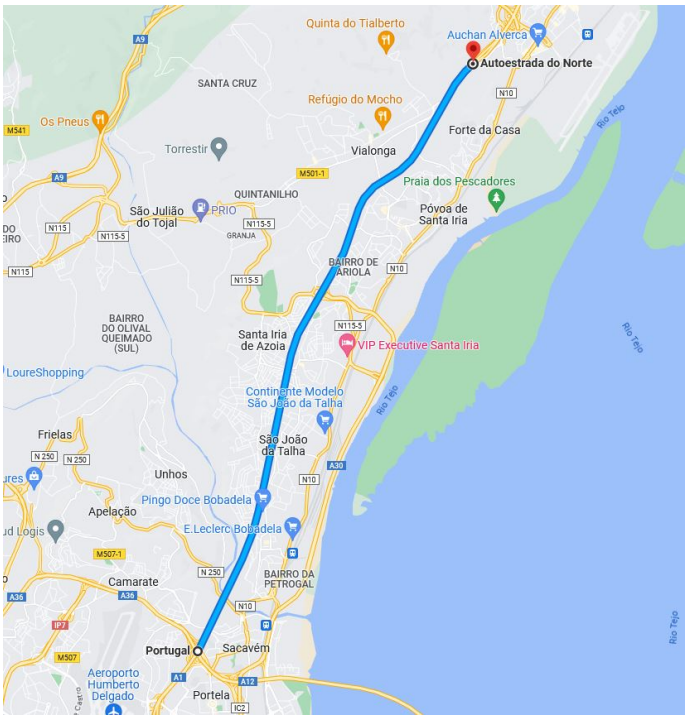

Figure 7.27: Drive test route.

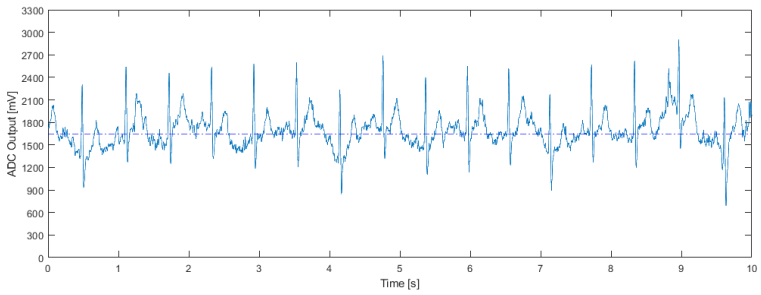

Figure 7.29: ECG recording excerpt with CardioWheel during drive test #1.

Figure 7.29 displays an excerpt of the recording.

Units

Table 7.14: Drive test results.

Parameter	**CardioWheel**		**Adaptive AFE**		**Unit**
Drive Test	1	2	3	4	#
Direction	N-S	S-N	N-S	S-N	Cardinal Direction
Time	10:09	8:47	9:56	12:12	min:s
QA output - BW	18.3	19.9	50.4 (19.7)	62.47 (6.9)	%
QA output - SAT	1.3	1.2	2.9	0.44	%
QA output - PLI	0.5	0.7	0.8	1.4	%
ADC optimization average	49.9	50.7	75.6	78.0	%

Table 7.14 details the results of the drive test. Note that for BW two values are presented; a limitation of the QA algorithm, regarding BW detection for this application, is that it does not take into account the offset adjustment described in Section 5.1.3. The threshold γ_{BW} is fixed and referenced to the ADC half-range, since the adjustment is free

Figure 7.28: In-Car acquisition set-up.

to offset the ADC input with the primary concern of maximizing it's dynamic range this results in multiple periods of false positive BW detection.

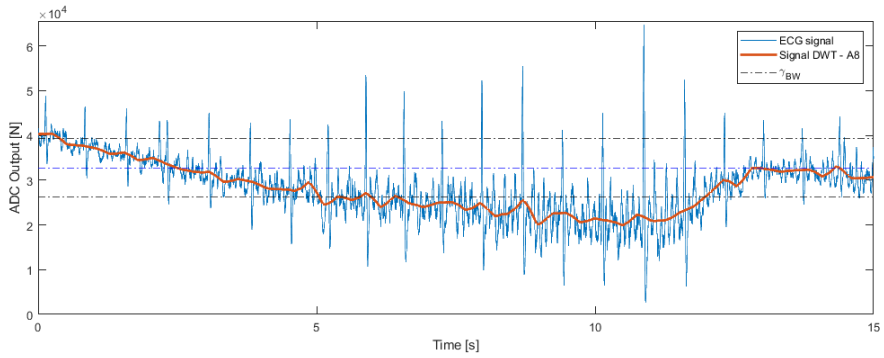

Figure 7.30: Interaction between γ_{BW} and offset adjustment - Excerpt from drive test #4.

This issue is further illustrated in Figure 7.30, in which there is acceptable signal quality even though BW detection threshold is exceeded for a significant amount of time. Therefore, to provide a fair comparison, a second value is provided, regarding the application of a digital high-pass of $f_c = 0.05Hz$ to the signals recorded adaptive AFE, this value was chosen as it is the absolute minimum defined in Section 2.2.4 and intended only to remove the DC offset as an variable solely for the QA algorithm BW detection. Results obtained are comparable and surpass CardioWheel.

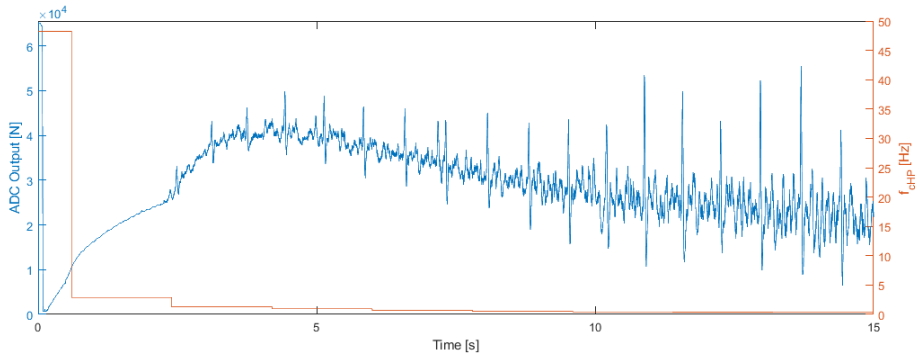

Figure 7.31: ECG recording excerpt with Fast Restore (FR) during drive test #4.

Regarding SAT detection in QA algorithm, by design, the developed system is intended to operate close to the edge of ADC SAT, making the device highly susceptible to EMA. This reflects in the few tenths of a percentage points increase in SAT detection. However, if the γ_{FR} threshold is exceeded, the device is quicker to adjust and settle AFE parameters to resume acquisition with appropriate signal quality as soon as possible. Figure 7.31 exemplifies an instance of FR; recovery time from saturation to ADC maximization was approximately 10 seconds. The results obtained are comparable and surpass CardioWheel.

Small variances in the results could also be due to real-world dynamic traffic conditions. For instance, drive test #4 encountered heavy traffic due to an accident near kilometer maker 2.6, which eventually forced the vehicle to come to a complete stop. As the chosen vehicle was of the manual gearbox type, the test subject was required to remove the hands from the steering wheel a multitude of times in order to select appropriate gearing and to take avoidance action via additional steering inputs.

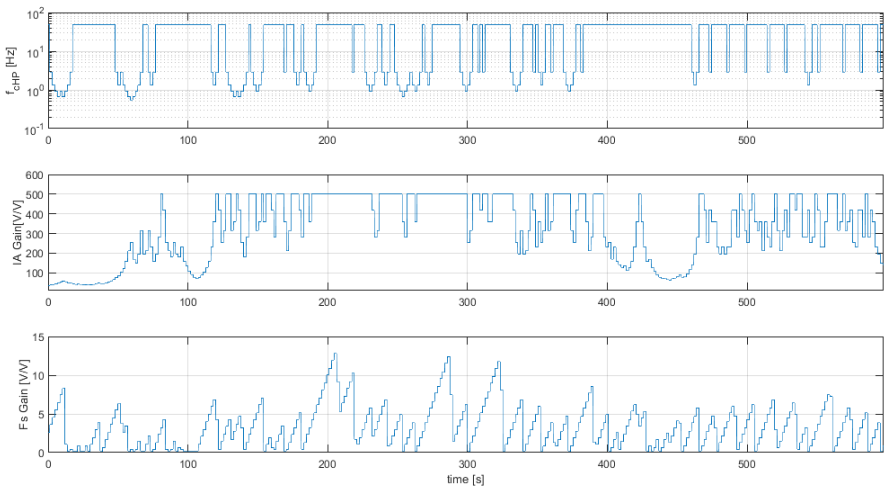

Figure 7.32: Evolution of control parameters over time for drive test #3.

Figure 7.32 displays the changes in control parameters over time form drive test #3. It is possible to observe how the gain parameters are affected. It was also noted that the recordings necessitated a great amount of effort from the test subjects in maintaining both hands on the steering wheel; after 2 to 3 minutes arm fatigue set in and a conscientious effort had to be made to maintain the required driving posture. It's likely a user of such a device, once implemented, won't maintain proper contact with the electrodes for extended periods of time, in contrast to the recordings presented in this Section. This issue intrinsic to human nature is of concern to human motricity fields of study, and reinforces that, if near-continuous monitoring of the subjects is desired, adaptability and fast response are key to maximizing the potential of non-intrusive applications.

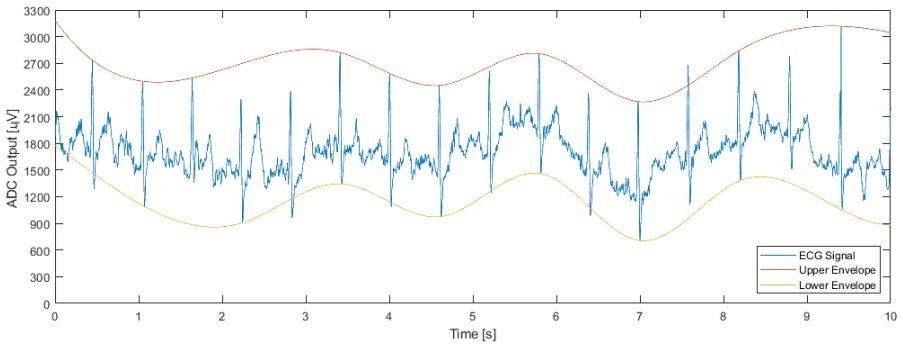

Figure 7.33: ECG signal envelope extraction. Signal obtained with CardioWheel.

In order to quantify ADC optimization a envelope was applied to the signals acquired from the drive tests. This envelope returns the upper and lower peak envelopes of the recordings. The envelopes are determined using spline interpolation over local maximums separated by at least 1 second of samples. The adaptive AFE provides a significant increase in ADC dynamic range optimization and results reflect the desired 80% value.

Chapter 8

Conclusion

The development of an adaptive electrocardiogram ECG recording system was one of the pieces of the puzzle that was required to further extend the application of ECG monitoring into real-world scenarios. The challenge of noise cancellation and the difficulty of using different materials for the electrodes previously required the manual change of the AFE characteristics. In this project, these issues have been tackled by creating a more resilient system to the most common types of issues affecting ECG recordings via dynamic adaptation of its key parameters.

Example applications scenarios of this technology include:

- Perform ECG acquisition in unfavorable and / or dynamic conditions.
- Perform ECG acquisition in scenarios with varied types of patients, e.g. pediatric care (age ranging from birth to 16 years old).
- Validate the capability of novel types of electrodes for application in ECG signal acquisition such as:
  - conductive textiles,
  - conductive plastics or polymers,
  - conductive rubber,
  - conductive coatings.
- Quickly identify and extract optimal parameters for application in static configuration systems.

The QA algorithm developed in this project also shows promising results, given that it is not reliant on the ECG signal directly but rather on the noise and the surrounding components resulting from signal decomposition; thus the algorithm is applicable to situations where ECG signal cannot be directly analyzed due to regulatory restrictions, such as in European Union General Data Protection Regulation (GDPR). The results presented a very high success rate (over 97%) of acceptable ECG recording prediction.

The full system was tested with a wide range of test subjects, from 10 to 63 years of age, healthy or with preexisting cardiac conditions as well as with a plethora of system configurations, electrode types and acquisition scenarios. The system's performance surpassed the authors' initial expectations, achieving successful results even in unfavorable and scientific exploratory scenarios. These results pave the way for new possibilities in the field of ECG acquisition.

8.1 Future Work

This project encompasses many areas of study, such as: hardware development, design and manufacturing, digital signal processing, software development, firmware development and user experience design. Thus, considering limited time frame and human resources of this project, results that any of these areas could be subject to further development. For this project, the main development effort was placed in the hardware design, with other areas such as software and firmware development being performed as a minimum viable option to allow the system to operate as a proof-of-concept for this novel approach to ECG acquisition. This was done to prove its efficacy and obtain performance metrics by comparatively quantifying improvement over static systems, under favorable and unfavorable conditions. The following paragraphs reflect the author's view on which areas to focus efforts of improvement in order to bring about the biggest performance gains.

Research into other hardware parameters of the AFE, such as a better performing IA or the refinement of the RLD, could improve intrinsic system performance via CMRR increase. Other areas such as a better performing ADC operating at higher resolutions and/or sample rates could provide benefits via DSP techniques in signal conditioning and ECG feature extraction, providing a better solution for demanding applications such as biometrics.

Development of a digital control system could unlock extra performance from the system in areas such as parameter optimization time and transient response. This could ultimately provide a algorithm better suited for fast-paced wearable applications such as ECG monitoring in sporting activities.

System miniaturization could also be performed; in this project form factor was not considered a constraint, however, most of the chosen components are offered in smaller packages such as surface-mount technology (SMT) alternatives. The chosen Raspberry Pi Pico MCU could also be feasibly replaced with an embedded system-on-chip (SoC) or field-programmable gate array (FPGA) device, of which exist multiple options in the market providing sufficient DSP computing power for edge-computing applications. In conjunction with wireless communication technologies and battery power the system could become a very capable solution for wearable applications.

Physiological monitoring, in particular electrocardiogram recording, is an ever evolving field of study, the enumerated topics are but a fraction of what future developments will bring.

Appendices

Appendix A

ECG Signal Wavelet Decomposition Example

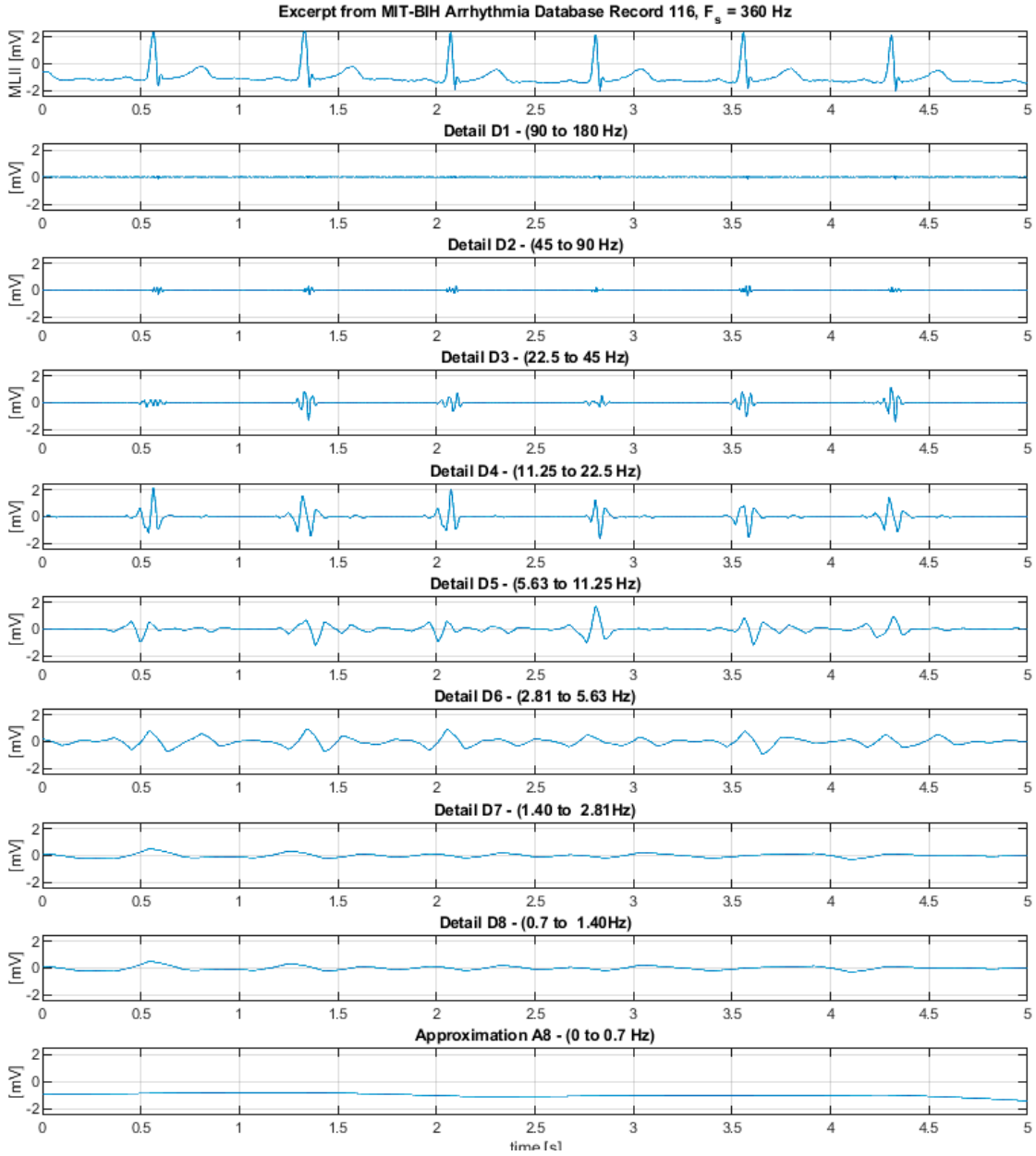

Figure A.1: Wavelet decomposition of ECG signal.

Appendix B

Raspberry Pi Pico - MicroPython Firmware Code

(Conteúdo removido ao abrigo da alínea 3ª do Artigo 17º do Anexo do Despacho n.º 10934/2020, publicado em Diário da República Portuguesa n.º 217/2020, Série II de 6 de Novembro de 2020.)

Appendix C

Test Subjects - Full List

Table C.1: Test subject data.

Test Subject #	Sex	Age [years]	Weight [kg]	Height [m]	Heart conditions
1	Male	30	80	1,90	No
2	Female	26	70	1,69	No
3	Male	57	87	1,79	No
4	Female	54	63	1,58	Tachycardia
5	Female	7	23	1,25	No
6	Male	10	39	1,42	No
7	Female	38	76	1,62	No
8	Male	38	78	1,84	No
9	Female	62	95	1,61	No
10	Male	37	110	1,84	No
11	Male	63	105	1,87	Yes
12	Male	35	82	1,89	No
13	Male	28	87	1,87	No

ECG recordings were performed with explicit test subject consent. For test subjects under the age of 18 years old ECG recordings were perform with explicit caregiver consent.

Appendix D

Hardware

D.1 PCB Test Points

Table D.1: Hardware test point.

Test Point #	**Parameter**
1	Instrumentation Amplifier Output
2	First Gain Stage Output
3	Notch Filter Output
4	Notch Filter Buffer Output
5	Sallen-Key LPF #1 Output
6	Sallen-Key LPF #2 Output
7	ADC Maximizing Stage Input
8	Analog Front-End Output
10	Voltage Divider for Voltage Reference
12	Voltage Reference
13	ADC Maximizing Stage Offset Voltage Buffer Input
14	ADC Maximizing Stage Offset Voltage Buffer Output
15	Integrated High-Pass Filter-Driven IA Voltage Reference
20	Voltage Rail for MCU (typ: 3.3 V)
21	Voltage Rail for AFE (typ: 2.7 V)

D.2 Final Design Schematic

(Conteúdo removido ao abrigo da alínea 3ª do Artigo 17º do Anexo do Despacho n.º 10934/2020, publicado em Diário da República Portuguesa, II série a 6 de Novembro de 2020.)

D.3 Twin-T Notch Transfer Function

$$H_n(s) = \frac{s^3+s^2\left(\frac{1}{C_{n1}.R_{n1}}+\frac{1}{C_{n1}.R_{n2}}+\frac{1}{C_{n2}.R_{n2}}+\frac{1}{C_{n2}.R_{n3}}+\frac{1}{C_{n3}.R_{n2}}\right)+s\left(\frac{C_{n3}.R_{n3}+C_{n1}.R_{n1}}{C_{n1}.R_{n1}.C_{n3}.R_{n3}.R_{n2}}\right)+\frac{1}{C_{n1}.C_{n2}.C_{n3}.R_{n1}.R_{n2}.R_{n3}}}{s^3+s^2\frac{1}{C_{n1}}\left(\frac{1}{R_{n1}}+\frac{1}{R_{n2}}\right)+s\frac{1}{C_{n1}.R_{n1}.R_{n2}}\left(\frac{1}{C_{n3}}+\frac{1}{C_{n2}}+\frac{C_{n1}.C_{n2}.C_{n3}.R_{n1}.R_{n2}.R_{n3}}{C_{n3}.C_{n1}.R_{n1}.R_{n2}+C_{n2}.C_{n1}.R_{n1}.R_{n2}+C_{n2}.C_{n3}.R_{n3}.R_{n2}}\right)+\frac{1}{C_{n1}.C_{n2}.C_{n3}.R_{n1}.R_{n2}.R_{n3}}}$$

(D.1)

Bibliography

[1] J. Moeyersons, "Artefact detection and quality assessment of ambulatory ecg signals," *Computer Methods and Programs in Biomedicine*, no. 1, Aug. 2019.

[2] J. G. Webster, *Medical Instrumentation: Application & Design*, Third Edition. Wiley, 1993.

[3] A. Khawaja, "Automatic ecg analysis using principal component analysis and wavelet transformation," *Karlsruhe transactions on biomedical engineering*, no. 3, 2019.

[4] R. P. J. Malmivuo, *Bioelectromagnetism - Principles and Applications of Bioelectric and Biomagnetic Fields*, First Edition. Oxford University Press, 1995.

[5] W. Einthoven, *Galvanometrische registratie van het menschelijk electrocardiogram.* 1902, pp. 101–106.

[6] University of Nottingham - School of Health Sciences. "A beginners guide to normal heart function, sinus rhythm & common cardiac arrhythmias." (2020), [Online]. Available: `https://www.nottingham.ac.uk/nursing/practice/resources/cardiology/function/bipolar_leads.php` (visited on 02/01/2020).

[7] CardioSecur. "Ecg lead systems." (2020), [Online]. Available: `https://www.cardiosecur.com/magazine/specialist-articles-on-the-heart/lead-systems-how-an-ecg-works` (visited on 02/01/2020).

[8] A. S. Sedra, *Microelectronic Circuits*, Eighth Edition. Oxford University Press, 2020.

[9] C. Kitchin and L. Counts, *A Designer's Guide to Instrumentation Amplifiers*, 3rd ed. 2001.

[10] International Electrotechnical Commission, *IEC 60601-1:2014 - Medical electrical equipment – Part 1: General requirements for basic safety and essential performance.* 2014.

[11] International Electrotechnical Commission, *IEC 60601-2-47:2012 - Particular requirements for safety, including essential performance, of recording and analysing single channel and multichannel electrocardiographs.* 2012.

[12] B. Young and J.-J. Schmid, "The new iso/iec standard for automated ecg interpretation," *Hearts*, vol. 2, pp. 410–418, 3 2021.

[13] J. Bailey and et al., "Recommendations for standardization and specifications in automated electrocardiography: Bandwidth and digital signal processing," *Circulation*, no. 81, 2 1990.

[14] AAMI, "Diagnostic electrocardiographic devices, ec11," *AAMI*, 2 2001.

[15] Y. Fu, "Dry electrodes for human bioelectrical signal monitoring," *National Library of Medicine*, vol. 20, 13 Jun. 2020.

[16] Texas Instruments, "Improving common-mode rejection using the right-leg drive amplifier," *TI Application Report - SBAA188*, no. 6, 2011.

[17] D. Prutchi and M. Norris, "Biopotential amplifiers," *Design and Deveplment of Medical Electronic Instrumentation*, 2005.

[18] R. Kher, "Signal processing techniques for removing noise from ecg signals," *Journal of Biomedical Engineering and Research*, no. 1, Mar. 2019.

[19] U. Satija, B. Ramkumar, and M. S. Manikandan, "An automated ecg signal quality assessment method for unsupervised diagnostic systems," *Biocybernetics and Biomedical Engineering*, no. 38, 2018.

[20] M. Abdelazez, A. D. C. Chan, and et al., "Signal quality indices for ambulatory electrocardiograms used in myocardial ischemia monitoring," *IFMBE Proceedings*, no. 51, Jun. 2015.

[21] E. Richard and A. D. C. Chan, "Design of a gel-less two-electrode ecg monitor," *IEEE International Workshop on Medical Measurements and Applications*, Apr. 2010.

[22] B. Jaswanth and et al., "A comparative analysis of cmos amplifiers for ecg signals," *International Research Journal of Engineering and Technology*, no. 6, Apr. 2019.

[23] D. P. Dobrev and T. D. Neycheva, "Software automatic gain control for common mode interference stabilization," *XXIX International Scientific Conference Electronics - ET2020*, no. 9, 2020.

[24] D. P. Dobrev and T. D. Neycheva, "Automatic common mode electrode-amplifier impedance balance: Implementation and results," *XXVIII International Scientific Conference Electronics - ET2019*, no. 9, 2019.

[25] J. Guerreiro, *A Biosignal Embedded System for Physiological Computing*. ISEL, 2013.

[26] D. Almeida, *Non-Intrusive ECG Acquisition Test-bed*. ISEL, 2018.

[27] Agilent Technologies, *Agilent 33250A Function Arbitrary Waveform Generator User's Guide*. 2013.

[28] A. L. Goldberger and et al., "Components of a new research resource for complex physiologic signals," *Circulation*, vol. 101, e215–e220, 23 2000.

[29] Open Knowledge Foundation. "Open data commons attribution license (odc-by) v1.0." (2020), [Online]. Available: `https://opendatacommons.org/licenses/by/1-0/index.html` (visited on 02/01/2020).

[30] G. Moody and R. Mark, "The impact of the mit-bih arrhythmia database," *IEEE Eng in Med and Biol 20(3):45-50*, Jun. 2019.

[31] G. Moody, W. Muldrow, and R. Mark, "A noise stress test for arrhythmia detectors," *Computers in Cardiology 1984; 11:381-384.*, Jun. 1984.

[32] V. Sygouni and et al., "Capillary pressure spectrometry: Toward a new method for the measurement of the fractional wettability of porous media," *Physics of Fluids*, vol. 18, 5 Sep. 2005.

[33] L. Cohen, *Wavelet Transforms and Time-Frequency Signal Analysis. Applied and Numerical Harmonic Analysis*. Birkhäuser, 2001, pp. 217–232.

[34] MathWorks. "R wave detection in the ecg." (2020), [Online]. Available: `https://www.mathworks.com/help/wavelet/ug/r-wave-detection-in-the-ecg.html` (visited on 02/01/2020).

[35] D. Velez, A. Lourenço, and J. Costa, "Electrocardiographic signal quality assessment without morphology analysis," *7th IEEE Portuguese Meeting on Bioengineering (ENBENG 2023)*, 2023. DOI: `10.1109/ENBENG58165.2023.10175317`.

[36] Silicon Laboratories, "Improving adc resolution by oversampling and averaging, an118," *SilLabs Application Notes*, 1 2013.

[37] Lean2. "Pi pico adc input using dma and micropython." (2020), [Online]. Available: `https://iosoft.blog/2021/10/26/pico-adc-dma/` (visited on 02/01/2020).

[38] Future Technology Devices International, *FT232R USB UART IC Datasheet*, v2.16. May 2020.

[39] C. Gambill and et al., "T wave amplitudes in normal populations: Variation with ecg lead, sex, and age," *Journal of Electrocardiology*, vol. 28, pp. 191–197, 3 1995.

[40] Primasil Silicones Ltd., *Conductive – High Consistency Silicone Rubber (HCR) Technical Data Sheet*.

[41] ProtoPlant, *ProtoPasta CDP1xxxx Conductive PLA Technical Data Sheet*, 1st ed.

[42] R. J. van de Plassche, *Integrated Analog-To-Digital and Digital-To-Analog Converters*. Springer Science, 1994.

[43] H. A. Snellen, *Willem Einthoven* 18601927*, Father of electrocardiography: Life and work, ancestors and contemporaries*, First Edition. Kluwer Academic Publishers, 1995.

[44] R. P. J. Malmivuo, *The Electrodermal Response*, First Edition. Oxford University Press, 1995.

[45] Analog Devices, *AD8232 Single-Lead Heart Rate Monitor Front End Datasheet*, D. 2020.

[46] Analog Devices, *AD8221 Precision Instrumentation Amplifier Datasheet*, C. 2011.

[47] Olimex, *SHIELD-EKG-EMG bio-feedback shield - User's Manual*, E.

[48] Maxim Integrated Products, *MAX4194–MAX4197 Product Data Sheet*. May 2015.

[49] Texas Instruments, *INA125 Product Data Sheet*. Jun. 2022.

[50] Texas Instruments, *APPLICATION BULLETIN - AC COUPLING INSTRUMENTATION AND DIFFERENCE AMPLIFIERS*. 2022.

[51] Texas Instruments, *INA333 Product Data Sheet*. Dec. 2015.

[52] S.-Y. Lee and C.-J. Cheng, "Systematic design and modeling of a ota-c filter for portable ecg detection," *IEEE Transactions on Biomedical Circuits and Systems*, no. 3, Jan. 2009.

[53] M. Abdelazez, A. D. C. Chan, and et al., "Signal quality indices for ambulatory electrocardiograms used in myocardial ischemia monitoring," *IFMBE Proceedings*, no. 51, Jun. 2015.